Master's Thesis of Engineering

Seismic Performance of Precast Columns and Beam-column Connections with Geopolymer Concrete

지오폴리머 콘크리트를 사용한 프리캐스트 기둥 및 보−기둥 접합부의 내진성능

February 2023

Graduate School of Engineering
Seoul National University
Architecture and Architectural Engineering

Han-Se Moon

Seismic Performance of Precast Concrete Columns and Beam-column Connections with Geopolymer Concrete

Advisor: Hong-Gun Park

Submitting a Master's thesis of
Architecture and Architectural Engineering

February 2023

Graduate School of Engineering
Seoul National University
Architecture and Architectural Engineering

Han-Se Moon

Confirming the Master's thesis written by
Han-Se Moon

February 2023

Chair	**Sung-Gul Hong**	**(Seal)**
Vice Chair	**Hong-Gun Park**	**(Seal)**
Examiner	**Cheol-Ho Lee**	**(Seal)**

Abstract

Seismic Performance of Precast Concrete Columns and Beam-column Connections with Geopolymer Concrete

Moon, Han Se
Department of Architecture and Architectural Engineering
College of Engineering
Seoul National University

In the recent situation with the environmental problem worsening, cement which occupies a large proportion of global CO_2 emissions can be a good target for reducing CO_2 emissions in the construction industry. Geopolymer concrete is one type of alternative concrete which does not use any Portland cement but alkaline activators and industrial by-products such as fly ash or ground granulated blast-furnace slag (GGBS). However, geopolymer concrete has a large range of variations in materials and mix proportions, making it difficult to quantify the generic performance of geopolymer concrete. Furthermore, most of the existing studies on geopolymer concrete have been conducted at the material level, and studies at the member or structural level are insufficient. If

any, only few studies have reported the seismic performance of geopolymer concrete members by cyclic loading tests. Besides, building codes do not allow cementitious materials not specified in the industry standard, with an exception when investigation and verification were conducted through performance tests.

The geopolymer concrete in this study had a specific mix proportion with the binder composed of 100% GGBS and alkaline activator (Ca-type composites). The normal concrete to be compared consisted of the binder with 70% cement and 30% GGBS. The material tests were conducted to investigate mechanical properties of the geopolymer concrete, including compressive strength, stress-strain curve, modulus of elasticity, strain at peak stress, modulus of rupture (i.e. flexural strength), and splitting tensile strength.

Cyclic loading tests were conducted to evaluate the seismic performance of precast concrete (PC) columns and beam-column connections using the geopolymer concrete. For column tests, a total of 7 column specimens (2 normal concrete and 5 geopolymer concrete) were tested with 13% compression ratio loaded on the top of the columns. The test parameters included concrete types (normal or geopolymer), construction methods (monolithic or PC), sizes of splice sleeves (D25 or D29), and reinforcement ratio (0.0162 or 0.00254). For beam-column connections, a total of 3 specimens (1 normal concrete and 2 geopolymer concrete) were tested. The test parameters included concrete types (normal or geopolymer), construction methods (monolithic or PC), and overlap lengths of joint hook anchorage (290 mm or 170 mm). The performance was mainly compared in terms of strength, load-displacement relationship, secant stiffness, energy dissipation, and deformation capacity. The seismic performance of each specimen was evaluated by ACI

374.1-05 and AIJ 2002 Guidelines.

The geopolymer concrete had equivalent mechanical properties to the normal concrete or exceeded the design codes' equations overall. The PC columns and beam-column connections using the geopolymer concrete developed the predicted strengths calculated by the design codes. The PC geopolymer concrete specimens showed superior seismic performance to the monolithic normal concrete specimens. The load-displacement relationship and energy dissipation of the PC columns using the geopolymer concrete were equivalent to those of the PC columns using the normal concrete. However, the ductility of the PC columns using the geopolymer concrete was 35% lower than that of the PC column using normal concrete due to the effect of grouting quality.

The different performance between PC geopolymer concrete specimens and monolithic normal concrete specimens does not assure material superiority of the geopolymer concrete, which seems to be mainly caused by PC details. Thus, further study is needed for seismic performance of monolithic columns and beam-column connections using geopolymer concrete.

Keywords: Cyclic loading test, Geopolymer concrete, Column, Beam-column connection, Precast concrete, Grouted splice sleeve connection, Joint hook anchorage

Student Number: 2021-24712

Contents

List of Tables

List of Figures

Chapter 1. Introduction

1.1 Background

(a) CO_2 emissions

Recently, to manage climate change caused by increasing greenhouse gas emissions, nations in the world have taken measures to set and implement goals for reducing greenhouse gas emissions. The Kyoto Protocol (1997) and the Paris Agreement (2015) stipulate the countries' obligation to reduce carbon emissions. The Korean government announced a roadmap for reducing greenhouse gas emissions by 2030. The trend of reducing national greenhouse gas in response to climate change is leading to the implementation of carbon taxes and carbon border taxes.

In the construction industry, cement occupies a large proportion of carbon emissions as well as the amount of production. Among CO_2 emissions of building construction, CO_2 emissions due to cement occupy about 35% (UN Environment Programme, 2021). Cement production accounts for about 6% of the global total CO_2 emissions (McKinsey, 2022). 1 ton of cement production emits from 0.59 ton (IEA, 2021) to 0.93 ton (KEITI, 2021) of CO2. In this context, geopolymer concrete has been studied as an option to reduce CO2 emissions of the construction industry.

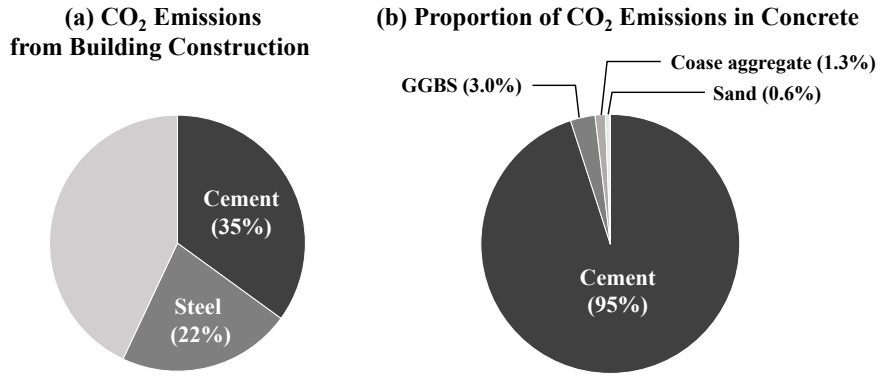

* In 2020 (UN Environmental Programme, 2021)

Figure 1-1 CO_2 emissions from cement

(b) Geopolymer concrete

Geopolymer concrete is a type of alternative concrete which does not use any Portland cement (Lloyd and Rangan, 2010). Instead of using cement, alkaline activators react with materials containing aluminum and silicon (or aluminosilicates) such as fly ash and ground granulated blast-furnace slag (GGBS). Through this chemical reaction so called 'geopolymerization', the mixture is binded (Mo et al., 2016). The term 'geopolymer concrete' was firstly coined by a French material scientist, Joseph Davidovits, in 1978 and various terms have been used for the same material including alkali-activated cement, inorganic polymer concrete, geocement, and so on (Srividya et al., 2022).

Two main constituents of geopolymer concrete are aluminosilicates and alkaline activator. As aluminosilicates, fly ash is mostly used and GGBS, metakaolin, rice husk ash, high calcium wood ash and combined of these materials can be used. As alkaline activator, NaOH and Na_2SIO_3 are mostly used and KOH and K_2SiO_3 can be used (Ma et al.,2018).

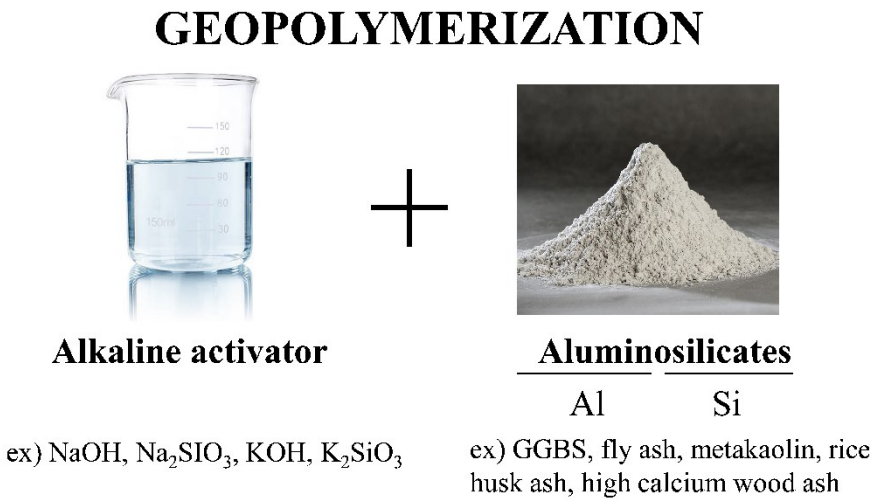

Figure 1-2 Composition of geopolymer concrete

(c) Previous studies on geopolymer concrete and limitations

Geopolymer concrete has a large range of variations on materials and mix proportions. This makes it difficult to quantify the generic performance of geopolymer concrete. It is possible to wrongly apply a result of a specific geopolymer concrete to a different one either with or without intention (Aldred and Day, 2012).

Most of the existing studies on geopolymer concrete were conducted at the material level, and studies at the member level and structure level are insufficient. And if any, the results of the structural tests varied and are not enough to conclude generic structural performance of geopolymer concrete (Ngo et al., 2021).

Among not many studies on the structural performance of geopolymer

concrete members, only few studies of them have reported the seismic performance by cyclic loading tests. The studies were about beam-column connections, and no study was found on the cyclic loading tests of columns. Contrary results were reported by the cyclic loading tests (refer to **2.2.2** and **Table 2-13**).

(d) Verification of structural performance of alternative-cement concrete

Cements not specified in the industry standard are not allowed to use in a building. The only way to use alternative cements is investigation and verification through performance tests (refer to **2.1. (f)**). KDS 14 20 01 :2022 and ACI 318-19 denote that alternative cements which are not cementitious materials specified in Korean Standard or ASTM standard can be allowed based upon the results of performance tests. KCS 14 20 10 :2022 also allows to use cements not specified in Korean Standard only if the quality and the usage are enough defined.

1.2 Scope and Objectives

In this study, the geopolymer concrete manufactured with a specific mix proportion was used. The research is divided into three parts: material tests, column tests, and beam-column connection tests.

Cyclic loading tests were conducted to evaluate the seismic performance of columns and beam-column connections using the geopolymer concrete. The geopolymer concrete specimens and the normal concrete specimens were compared, and also the geopolymer concrete specimens with different design parameters were compared one another. The performance was mainly compared in terms of strength, load-displacement relationship, energy dissipation, and ductility.

The columns and the beam-column connections in this study were manufactured in precast concrete (PC) construction. Because the geopolymer concrete uses activators to induce water and GGBS to react directly, the workability tends to decrease in a relatively short time after material mixing. In addition, since a large amount of GGBS is used instead of cement, initial strength develops slowly. Therefore, the geopolymer concrete is recommended to be applied to PC, which is advantageous for maintaining workability and for securing initial strength.

Connection details of PC were covered in the study, which are secondary but also important. For the columns, the effect of grouted splice sleeve connections was investigated. For the beam-column connections, the effect of hooked bar anchorage inside the joint was investigated.

1.3 Outline of the Master's Thesis

The outline of the master's thesis is illustrated in **Figure 1-3**.

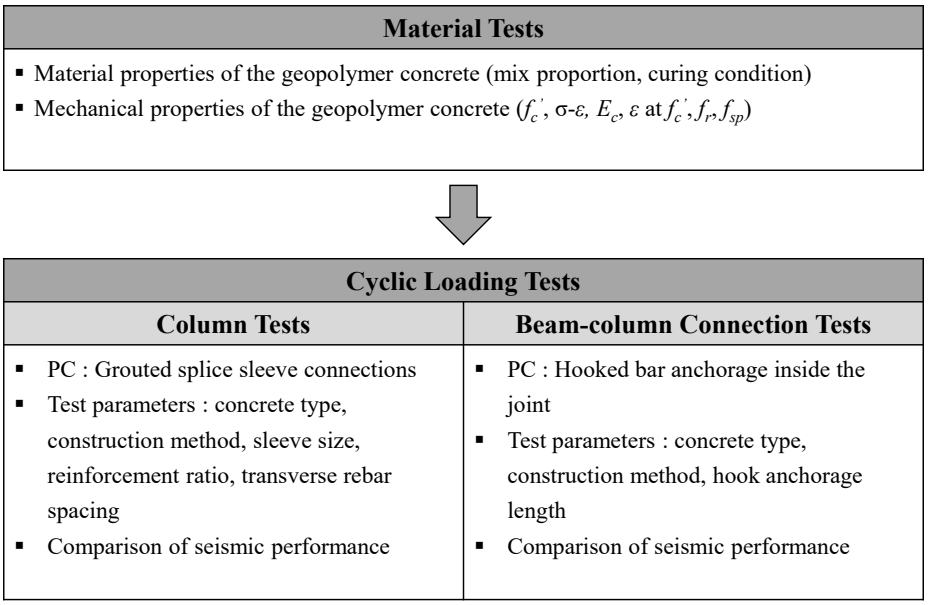

Figure 1-3 Outline of master's thesis

Chapter 2. Literature Review

2.1 Review of Current Design Standard

(a) Modulus of elasticity

The calculation of modulus of elasticity (E_c) varies among codes. ASTM C469 specifies how to calculate modulus of elasticity from concrete cylinder tests, and the other codes use compressive strength to estimate modulus of elasticity. The equations of each code for normal weight concrete are summarized below.

Table 2-1 Code provision for modulus of elasticity of concrete

Building code	Modulus of elasticity of concrete, E_c
ASTM C469, KS F 2438	Secant stiffness using 40% of peak stress
KDS 14 20 10 :2022	$8{,}500(f_c')^{1/3}$
ACI 318-19	$4{,}700\sqrt{f_c'}$

(b) Compressive strength of concrete in accordance with time

Compressive strength of concrete is affected by time after placing. It is well-known that as the age of the concrete goes by about until 28 days, the compressive strength increases. The design codes provide the equations predicting the development of concrete compressive strength in accordance with time $(f_c')_t$ as follows.

Table 2-2 Code provision for compressive strength of concrete in accordance with time

Building code	Compressive strength of concrete in accordance with time, $(f_c')_t$
KDS 14 20 01 :2022	$(f_c')_t = \exp\left(\beta_{sc}\left(1-\sqrt{\frac{28}{t}}\right)\right)(f_c')_{28}$
ACI 209R-92	$(f_c')_t = \frac{t}{\alpha+\beta t}(f_c')_{28}$

Here, t is the age of concrete, $(f_c')_t$ is concrete compressive strength at age t, $(f_c')_{28}$ is 28-day strength, β_{sc}, α, and β are cement-type coefficients

(c) Strain at peak stress

Strains at peak stress of concrete (ε_o) can affect cracking behavior of concrete buildings in the serviceability state. The strains at peak stress of concrete are known to become greater as compressive strength goes high. *fib* MC 2010 suggests mechanical characteristics of concrete. The equations and the table of strains at peak stress of concrete are summarized below.

Table 2-3 Proposed equation for strain at peak stress

Study	Strain at peak stress, ε_0
Nicolo and Pozzo (1994)	$0.00076+\left[\left(0.626f_c'/f^* - 4.33\right)\times10^{-7}\right]^{0.5}$
Tasdemir et al. (1998)	$\left[-0.067\left(f_c'/f^*\right)^2+29.9\left(f_c'/f^*\right)+1053\right]\times10^{-6}$

Here, f^* is 1 MPa.

Table 2-4 Strain at peak stress per *fib* MC 2010

Concrete grade	Characteristic strength, f_{ck} (MPa)	Mean strength, f_{cm} (MPa)	Strain at peak stress, ε_0
C12	12	20	0.0018
C16	16	24	0.0019
C20	20	28	0.0021
C25	25	33	0.0022
C30	30	38	0.0023
C35	35	43	0.0023
C40	40	48	0.0024
C45	45	53	0.0024
C50	50	58	0.0025
C55	55	63	0.0025
C60	60	68	0.0026
C70	70	78	0.0027
C80	80	88	0.0028
C90	90	98	0.0029
C100	100	108	0.0030

(d) Modulus of rupture

Modulus of rupture of concrete strength (f_r), also known as flexural strength, is a crucial factor for serviceability limit state; cracking, deflection, minimum flexural reinforcement and so on. In design codes such as ACI 318 and KDS 2022, the use of a minimum modulus of rupture is recommended for serviceability checks that include deflection and crack control. Hence these equations highly underestimate the actual modulus of rupture of concrete.

Legeron and Paultre (2000) analyzed 353 experimental data of which compressive strength ranged 20-130 MPa and proposed relations of modulus of rupture and compressive strengths. The study reported that the equation of ACI 318 ($0.62\sqrt{f_c'}$) is almost a lower bound relation ($0.6\sqrt{f_c'}$). The average relation

found in the study was $0.94\sqrt{f_c'}$ which is the same as the equation proposed by Carrasquillo et al. (1981). The equations of design codes and the equation proposed by the researchers for normal weight concrete are summarized below.

Table 2-5 Code provision for modulus of rupture

Building code or study	Modulus of rupture, f_r
KDS 14 20 30 :2022	$0.63\sqrt{f_{ck}'}$
ACI 318-19	$0.62\sqrt{f_c'}$
Carrasquillo et al. (1981)	$0.94\sqrt{f_c'}$

(e) Splitting tensile strength

The calculation of splitting tensile strength (f_{sp}) varies among codes. ACI 318-14 does not explicitly denote the equation of splitting tensile strength, but includes the equation in the commentary as an "assumption". Unlike other codes, *fib* model code 2010 uses characteristic compressive strength (f_{ck}) rather than compressive strength (f_c'), which makes it impossible to use concrete cylinder test. The equations of each code for normal weight concrete are summarized below.

Table 2-6 Code provision for splitting tensile strength

Building code	Criterion	Splitting tensile strength, f_{sp}	
ACI 318-14	-	$0.56\sqrt{f_c'}$	
ACI 363R-92	$21 < f_c' < 83$	$0.59\sqrt{f_c'}$	
fib MC 2010	$f_{ck} \leq 50$	$0.3(f_{ck})^{2/3}$	(i)
	$f_{ck} > 50$	$2.12ln(1 + 0.1(f_{ck} + 8))$	(ii)

(f) Alternative cements

KDS 14 20 01 :2022 and ACI 318-19 denote that alternative cements which are not cementitious materials specified in Korean Standard or ASTM standard can be allowed based upon the results of performance tests. KCS 14 20 10 :2022 also allows to use cements not specified in Korean Standard only if the quality and the usage are enough defined.

Table 2-7 Code provision for alternative cements

Building code	Content
KDS 14 20 01 :2022	(1) Cement shall be the same as or equivalent to those prescribed in KS L 5201, KS L 5205, KS L5210, KS L 5211, KS L 5217, and KS L 5401 of the Korean Industrial Standards. (4) This criterion may not be applied when designing by special investigative research. However, when designing according to research by performance experiments, the design basis considering the variability of material strengths and the variability of structural resistant capacities should be specified.
ACI 318-19	(a) Cementitious materials shall conform to the specifications in Table 26.4.1.1.1(a) (ASTM standard), except as permitted in 26.4.1.1.1(b). (b) Alternative cements shall be permitted if approved by the licensed design professional and the building official. Approval shall be based upon test data documenting that the proposed concrete mixture made with the alternative cement meets the performance requirements for the application including structural, fire, and durability.
KCS 14 20 10 :2022	(1) Ordinary Portland cement, moderate-heat Portland cement, high-early-strength Portland cement, low-heat Portland cement, sulfite-resistant Portland cement suitable for KS L 5201, Portland blast furnace cement suitable for KS L 5210, fly ash cement suitable for KS L 5211, and pozzolan cement suitable for KS L 5401 shall be used. (2) Cements other than (1) should be checked for its quality and its method of use should be sufficiently reviewed.

(g) One-way shear strength

Nominal one-way shear strength at a section (V_n) is calculated by the equation below.

$$V_n = V_c + V_s \quad \text{Eq 2-1}$$

$$V_s = \frac{A_v f_{yt} d}{s} \quad \text{Eq 2-2}$$

Here, V_c is a nominal shear strength due to concrete, Vs is a nominal shear strength due to transverse reinforcement, A_v is an effective area of all bar legs within spacing s, f_{yt} is a yield strength of a transverse reinforcement.

The calculation of V_c varies among codes with the same basic design equation shared, which is summarized below. In this study, the equation of ACI 318-19 (i) is used to calculated nominal one-way shear strength.

Table 2-8 Code provision for one-way shear strength due to concrete

Building code	Criterion	Nominal shear strength due to concrete, V_c	
KDS 14 20 22 :2022	Under only shear and bending moment	$\frac{1}{6}\lambda\sqrt{f_{ck}}b_w d$	(i)
	Under axial compression	$\frac{1}{6}\left(1+\frac{N_u}{14A_g}\right)\lambda\sqrt{f_{ck}}b_w d$	(ii)
ACI 318-19	$A_v \geq A_{v,min}$	$\left[0.17\lambda\sqrt{f_c'}+\frac{N_u}{6A_g}\right]b_w d$	(i)
		$\left[0.66\lambda(\rho_w)^{1/3}\sqrt{f_c'}+\frac{N_u}{6A_g}\right]b_w d$	(ii)
	$A_v < A_{v,min}$	$\left[0.66\lambda_s\lambda(\rho_w)^{1/3}\sqrt{f_c'}+\frac{N_u}{6A_g}\right]b_w d$	(iii)

where N_u is axial compression, A_g is gross sectional area, ρ_w is reinforcement ratio, and λ_s is size effect factor.

(h) Moment frames

ACI 318-19 denotes the definition of ordinary, intermediate, and special moment frames. Ordinary moment frames can be used for structures which are not resisting strong ground motion. ACI 318-19 18.3 should be satisfied. Intermediate moment frames can resist moderately strong ground motion. ACI 318-19 18.4 should be satisfied. Special moment frames can resist string ground motion. ACI 318-19 18.6 through 18.9 should be satisfied. In order of special, intermediate and ordinary, more requirements in reinforcement detailing are needed for the design of the moment frame, and better deformation capacity is expected.

ACI 352R-02 uses the terms such as type 1 connections and type 2 connections. Type 1 connections mean frame members with limited ductility, which are equal to ordinary moment frames. Type 2 connections mean frame members with large ductility, which are equal to intermediate or special moment frames.

(i) Hooked bars terminated in a joint

ACI 318-19, KDS 14 20 80 :2022 and ACI 352R-02 denote that hooked bars terminated in a joint should extend far to the opposite face of the joint. This is to help a diagonal compression strut inside the joint to form well. Especially, ACI 352R-02 recommends that hooks should extend so that distance between far face of joint hoops and the hook is less than 50 mm.

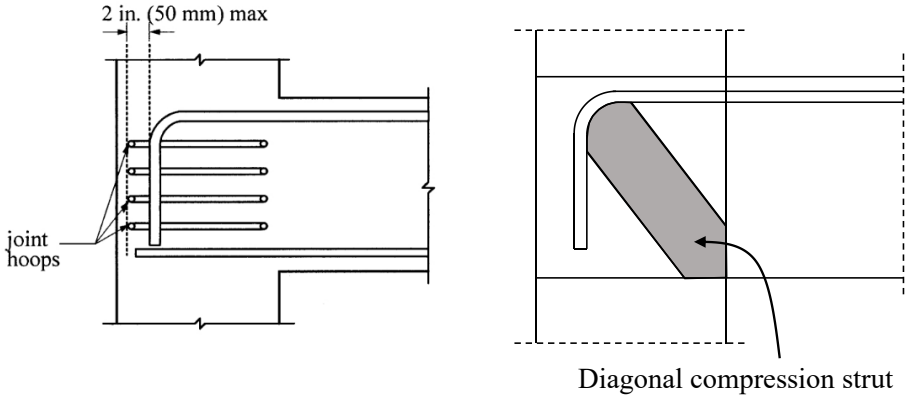

(a) Hook extension (b) Diagonal compression strut

Figure 2-1 Hook extension and resulting diagonal compression strut

(j) Development length of beam reinforcement in beam-column joint

The calculation of development length of hooked bars (l_{dh}) varies among codes. The basic equations of each code without modification factors are summarized below.

All the codes denote that the development length should be greater than $8d_b$ and 150 mm. Except ACI 318-19 (a, b) and ACI 352R-02 (b), the equations of the codes yield the same value ($1/4.2 \approx 0.24$). In the study, the equation of ACI 352R-02 (i) which yields the same value as ACI 318-14 and KDS 14 20 52 :2022 was used to calculated the development length of hooked bars.

Table 2-9 Code provisions for basic development length of hooked bars

Building code	Criterion	Development length of hooked bars, l_{dh}	Critical section	
KDS 14 20 52 :2022	-	$\frac{0.24 d_b f_y}{\sqrt{f_{ck}}}$	Column face	
ACI 318-14	-	$\left(\frac{0.24 f_y}{\sqrt{f_c'}}\right) d_b$	Column face	
ACI 352R-02	Ordinary moment frames	$\frac{f_y d_b}{4.2\sqrt{f_c'}}$	Column face	(i)
	Intermediate or special moment frames	$\frac{\alpha f_y d_b}{6.2\sqrt{f_c'}}$	Outside edge of the joint transverse reinforcement	(ii)
ACI 318-19	Ordinary or Intermediate moment frames	$\left(\frac{f_y}{23\sqrt{f_c'}}\right) d_b^{1.5}$	Column face	(i)
	Special moment frames	$\frac{f_y d_b}{5.4\sqrt{f_c'}}$	Outside edge of the joint transverse reinforcement	(ii)

Here, α (≥ 1.25) is the stress multiplier.

(k) Beam reinforcements passing through a joint

ACI 318-19, KDS 14 20 80 :2022, and ACI 352R-02 specify that when reinforcements of a beam pass through a joint, the beam reinforcements inside the joint can slip under cyclic loading. To reduce bond stresses and prevent bar slip, codes specify the minimum column depth in terms of the bar diameter, which are summarized below.

Table 2-10 Code provisions for column-depth-to-bar-diameter ratio

Building code	Criterion	h_c/d_b	
KDS 14 20 80 :2022	$f_y \leq 400$ MPa	≥ 20	(i)
	$f_y > 400$ MPa	≥ 25	(ii)
ACI 318-19	$f_y \leq 420$ MPa	≥ 20	(i)
	420 MPa $\leq f_y \leq 550$ MPa	≥ 26	(ii)
ACI 352R-02	-	$\geq 20\frac{f_y}{420}$	

Here, h_c is column depth

(l) Joint shear strength

Codes specify nominal joint shear strengths by different equations. The nominal joint shear strengths of beam-column connections with two opposite beams and a continuous column are summarized below. In this study, the equation of ACI 352R-02 (ii) was used.

Table 2-11 Code provisions for joint shear strength

	Nominal joint shear strength, $V_n = C \times \sqrt{f_c'} b_j h_c$		
Building code	Criterion	C	
KDS 14 20 80 :2022	-	1.25	
ACI 318-19	Ordinary moment frame	1.7	(i)
	Intermediate or special moment frame	1.2	(ii)
ACI 352R-02	Ordinary moment frame	1.66	(i)
	Intermediate or special moment frame	1.245	(ii)

Here, the beam-column connection is assumed to have two opposite beams and a continuous column. b_j is effective joint width, h_c is column depth.

And also, the definition of effective joint width (b_j) is varied among the codes. Nevertheless, the resulting values calculated by the different codes are similar. In this study, ACI 352R-02 was used to calculated nominal joint shear strength.

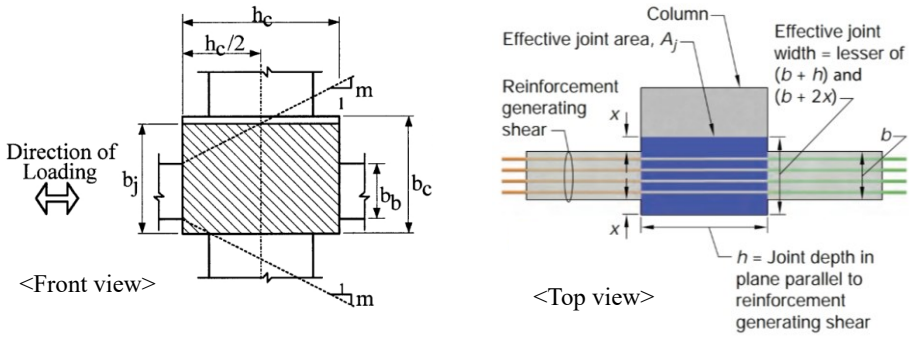

(a) ACI 352R-02 (b) ACI 318-19

Figure 2-2 Effective joint width

Table 2-12 Code provisions for effective joint width

Building code	Criterion	b_j
KDS 14 20 80 :2022, ACI 318-19	minimum of	b_b+h_c b_b+2x b_c
ACI 352R-02	minimum of	$\frac{b_b+b_c}{2}$ $b_b+\Sigma\frac{mh_c}{2}$ b_c

Here, b_b is beam width, b_c is column width, h_c is column depth, x and m are illustrated in **Figure 2-2**.

(m) Seismic performance evaluation by ACI 374.1-05

ACI 374.1-05 denotes acceptance criteria to evaluate high seismic performance of moment frames not satisfying requirements of ACI 318 for

special moment frames. ACI 318 also states that moment frames satisfying all the acceptance criteria of ACI 374.1 can be deemed as special moment frames (for moment frames, refer to **2.1 (h)**).

The acceptance criterion (a) is to ensure providing adequate initial stiffnesses, the acceptance criterion (b) to ensure following strong-column-weak-beam concept, the acceptance criterion (c) to ensure limiting the level of strength degradation, the acceptance criterion (d) to ensure adequate damping for the frame as a whole, and the acceptance criterion (e) to ensure no significant pinching effect.

The acceptance criteria defined in ACI 374.1-05 are as follows.

(a) The test module shall have attained a lateral resistance equal to or greater than the nominal strength (E_n) before its drift ratio exceeds the value consistent with the allowable story drift limitation (Δ_a) of ASCE/SEI 7-10.

(b) The maximum lateral resistance (E_{max}) recorded in the test shall have not exceeded λE_n, where λ ($=\sum M_{n,column}/\sum M_{n,beam}$) is the specified overstrength factor for the test column.

(c) At the third cycle of 3.5% drift ratio, peak force for a given loading direction shall have been not less than $0.75E_{max}$ for the same loading direction.

(d) At the third cycle of 3.5% drift ratio, the relative energy dissipation

ratio shall have been not less than 1/8.

(e) At the third cycle of 3.5% drift ratio, the secant stiffness from a drift ratio of −0.35% to a drift ratio of +0.35% shall have been not less than 0.05 times the stiffness for the initial drift ratio.

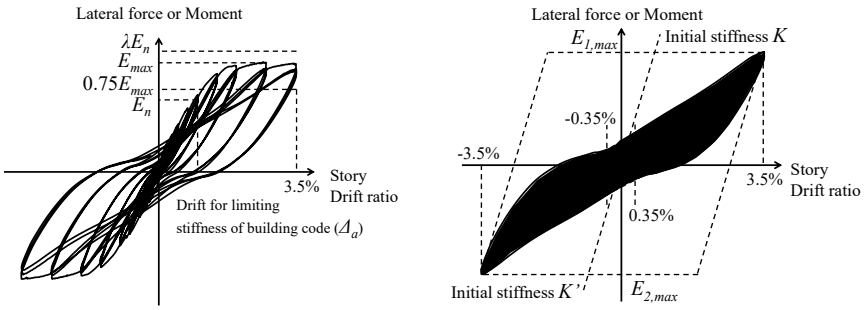

(a) Quantities used in evaluating acceptance criteria

(b) Relative energy dissipation ratio

Figure 2-3 Acceptance criteria of ACI 374.1-05

(n) Seismic performance evaluation by AIJ 2002 Guidelines

"Guidelines for Structural Design of Precast Concrete Connection Emulating Cast-in-place Reinforced Concrete (2002)" of Architectural Institute of Japan specifies structural performance goals so that PC structure can ensure the performance of RC structure.

Especially, AIJ 2002 Guidelines suggests structural performance goals of members on ultimate limit state under earthquake load. Part of structural performance goals are summarized as follows.

PC members whose connection is in a plastic hinge region when PC

structural system reaches ultimate limit state shall meet the following performance.

(a) The flexural yield strength of the PC member shall exceed the flexural yield strength of the RC member.

(b) The strength of the PC member shall exceed the strength of the RC member.

(c) For PC members with beam-column joints, the strength at 2% drift ratio shall exceed 80% of the peak strength.

(d) The difference between the flexural yield deformation of the PC member and the flexural yield deformation of the RC member shall be not more than 20%.

(e) For PC members with beam-column joints, at the 2nd cycle of 2% drift ratio, the energy dissipation of the PC member shall exceed 80% of the energy dissipation of the RC member.

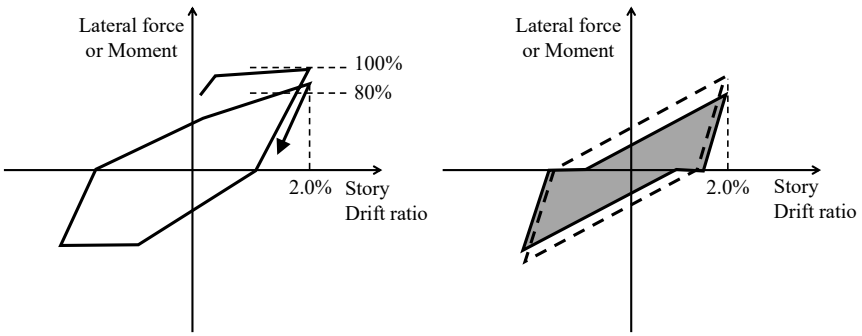

(a) Strength degradation (b) Energy dissipation

Figure 2-4 Acceptance criteria of AIJ 2002 Guidelines

2.2 Geopolymer Concrete

2.2.1 Material performance

(a) Diaz-Loya et al. (2011)

Diaz-Loya et al. investigated the relationship between mechanical properties and compressive strengths of geopolymer concrete and found out that flexural strengths and modulus of elasticity of geopolymer concrete had the same tendency as that of ordinary Portland cement concrete. The binder material was fly ash with various samples of chemical composition. The activator was a mixture of 14 M sodium hydroxide (NaOH) solution and sodium silicate (Na_2SiO_3). The activator-solution-to-binder ratio was ranged from 40 to 98%.

(b) Amran et al. (2020)

Amran et al. broadly reviewed studies on mechanical properties of geopolymer concrete. The splitting tensile strength of geopolymer concrete could be 30% more than that of normal concrete. The flexural strength of geopolymer concrete could increase 25% compared with normal concrete depending on binder materials, but on the other hand, could decrease by using a less amount of activator. The modulus of elasticity could increase or decrease depending on an amount of activator. The stress-strain behavior of geopolymer concrete was similar to or more brittle than that of normal concrete.

(c) Hutagi et al. (2020)

Hutagi et al. conducted cyclic compressive loading tests of geopolymer concrete cylinders and concluded that the cyclic behavior of geopolymer concrete agreed well with the monotonic behavior. The envelop curves of the cyclic compressive loading tests were compared with the stress-strain curves of the monotonic compressive tests. The binder materials of geopolymer concrete were fly ash and GGBS, and the activator was a mixture of NaOH and Na_2SiO_3. The activator-solution-to-binder ratio was either of 30% (f_c'=60 MPa), 35% (f_c'=50 MPa), and 40% (f_c'=40 MPa).

2.2.2 Structural performance (cyclic loading tests)

Among not many studies on the structural performance of geopolymer concrete members, only few studies of them have reported the seismic performance by cyclic loading tests. The studies were about beam-column connections, and no study was found on the cyclic loading tests of columns.

The results of the studies varied in terms of seismic performance. Some study (Ngo et al., 2021) reported that the geopolymer concrete specimens showed inferior seismic performance to the normal concrete specimens. On the other hand, some studies (Raj et al., 2016; Saranya et al., 2021) reported that the geopolymer concrete specimens showed equivalent or better seismic performance.

The studies adopted various properties of materials including types of binder materials and the amount of the activator solution. The literature on cyclic

loading tests of geopolymer concrete members was summarized in **Table 2-13** and explained one by one below.

Table 2-13 Previous studies on cyclic loading tests for geopolymer concrete element

Study	Material			Element	Result[2)]
	Binder	Alkaline activator	A/B ratio[1)]		
Ngo et al. (2021)	GGBS[3)], Fly Ash	NaOH, Na_2SiO_3	60%	Beam-column connection	- Similar (monolithic) - Inferior (PC)
Raj et al. (2016)	Fly ash	NaOH, Na_2SiO_3	35%	Beam-column connection	- Equivalent or better (monolithic) - Equivalent or better (SFRC[4)])
Saranya et al. (2021)	GGBS, Dolomite	NaOH, Na_2SiO_3	60%	Beam-column connection	- Better (monolithic)
Mao et al. (2022)	Slag, Fly ash	NaOH, Na_2SiO_3, Na_2CO_3	38-50%	Beam-column connection	- Inferior (monolithic)

1) A/B ratio : activator-to-binder ratio
2) Compared to ordinary Portland cement specimen
3) GGBS : ground granulated blast-furnace slag
4) SFRC : steel fiber reinforced concrete

(a) Ngo et al. (2021)

Ngo et al. conducted cyclic loading tests of 4 beam-column connection specimens including 1 monolithic specimen with geopolymer concrete, 1 PC specimen with geopolymer concrete, 1 monolithic specimen with ordinary portland concrete, and 1 PC specimen with ordinary portland concrete. The binder materials of the geopolymer concrete were 2:3 ratio of GGBS and low calcium fly ash, and the activator was a mixture of 12 M sodium hydroxide (NaOH) and D-grade sodium silicate (Na_2SiO_3) solution. The activator-

solution-to-binder ratio was 60%.

While the tests of the monolithic specimens either with the geopolymer concrete or ordinary portland concrete yielded similar results, the test result of the PC specimen with the geopolymer concrete was inferior to that of the ordinary portland concrete specimen. The PC specimen with the geopolymer concrete showed brittle failure behavior, the ductility of which was 42.8% lower than that of the ordinary portland concrete specimen. Nevertheless, the monolithic specimen with the geopolymer concrete showed equivalent performance to the ordinary portland concrete specimen in terms of strength, load-displacement relationship, energy dissipation, and ductility. And also, the crack patterns of both ordinary portland concrete and the geopolymer concrete specimens were similar regardless of construction methods.

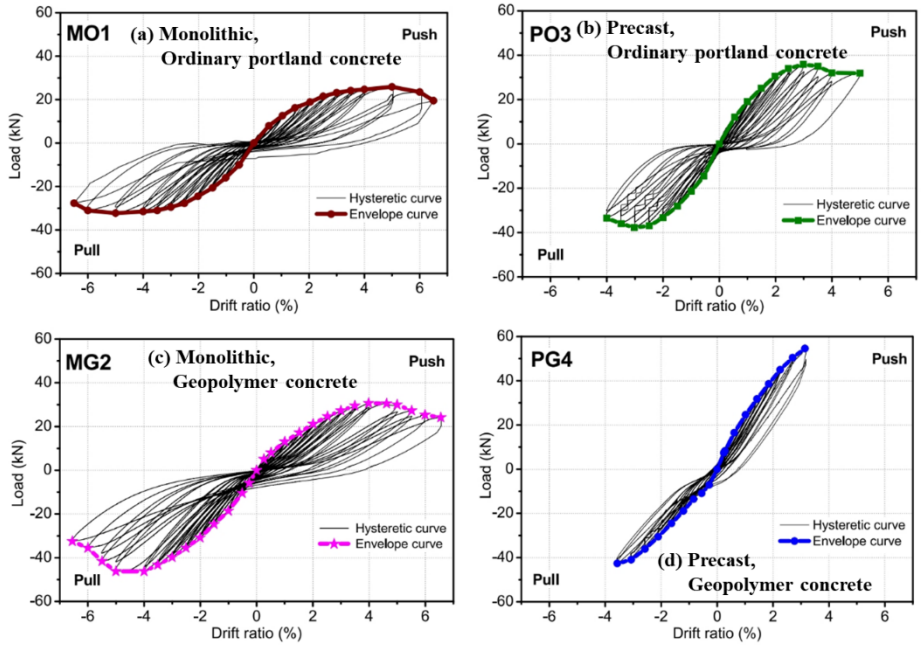

Figure 2-5 Load-displacement relationships in Ngo et al. (2021)

(b) Raj et al. (2016)

Raj et al. conducted cyclic loading tests of 4 beam-column connection specimens including 2 geopolymer concrete specimens (plain or steel fiber reinforced) and 2 conventional concrete specimens (plain or steel fiber reinforced). The binder material of geopolymer concrete was low calcium fly ash (Class F), and the activator was a mixture of sodium silicate (Na_2SiO_3) solution and sodium hydroxide (NaOH) solution. The activator-solution-to-binder ratio was 35%.

The results of the geopolymer concrete specimens were equivalent to or better than those of the plain conventional concrete specimens in both plain and

steel fiber reinforced concrete specimens. The specimens showed similar performance in terms of strength, load-displacement relationship, energy dissipation, deformation capacity, stiffness and etc. In **Figure 2-6,** GBJ and CCJ are the plain concrete specimens with the geopolymer concrete and conventional concrete respectively. SFRGBJ and SFRCCJ are the steel fiber reinforced concrete specimen with the geopolymer concrete and conventional concrete, respectively.

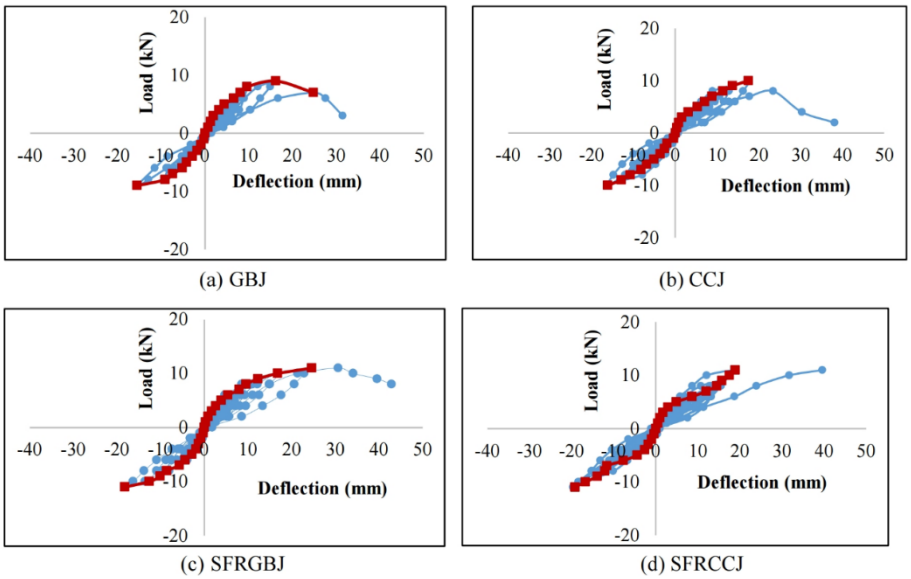

Figure 2-6 Load-displacement relationships in Raj et al. (2016)

(c) Saranya et al. (2021)

Saranya et al. conducted cyclic loading tests of 5 beam-column connection specimens including 1 geopolymer concrete, 1 cement concrete, and 3 steel fiber reinforced geopolymer concrete specimens. The binder materials of the geopolymer concrete were GGBS and dolomite with 7:3 ratio, and the activator

was a mixture of sodium silicate (Na_2SiO_3) and sodium hydroxide (NaOH). The activator-solution-to-binder ratio was 60%.

The results of the geopolymer concrete specimen were better than those of the cement concrete specimen. The geopolymer concrete specimen showed better performance in terms of load-displacement relationship, energy dissipation, ductility, and toughness. In **Figure 2-7**, OPC 0 is the cement concrete specimen, GPC is the geopolymer specimen, and SFGPC 0.25, SFGPC 0.5, and SFGPC 0.75 are the geopolymer specimens with 0.25%, 0.5% 0.75% steel fibers, respectively.

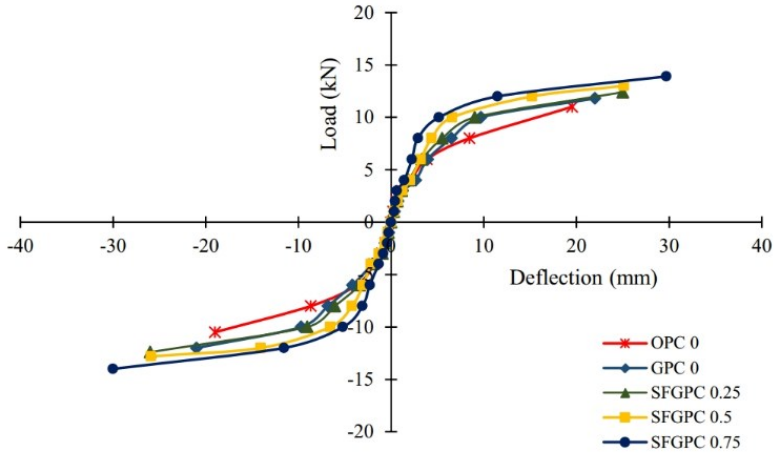

Figure 2-7 Envelop curves in Saranya et al. (2021)

(d) Mao et al. (2022).

Mao et al. conducted cyclic loading tests of 11 beam-column connection specimens including 8 geopolymer concrete and 3 normal concrete specimens. The binder materials of the geopolymer concrete were slag and fly ash, and the

activator was a mixture of Na_2SiO_3, NaOH and Na_2CO_3. The activator-solution-to-binder ratio was 38-50%.

The results of the geopolymer concrete specimen were inferior to those of the normal concrete specimens. The geopolymer concrete specimens showed lower stiffness, lower ductility, early strength degradation, higher stiffness degradation rate, and lower energy dissipation capacity than the normal concrete specimens. The authors explained that the geopolymer concrete used was more brittle than the normal concrete and it developed micro-cracks in the specimens.

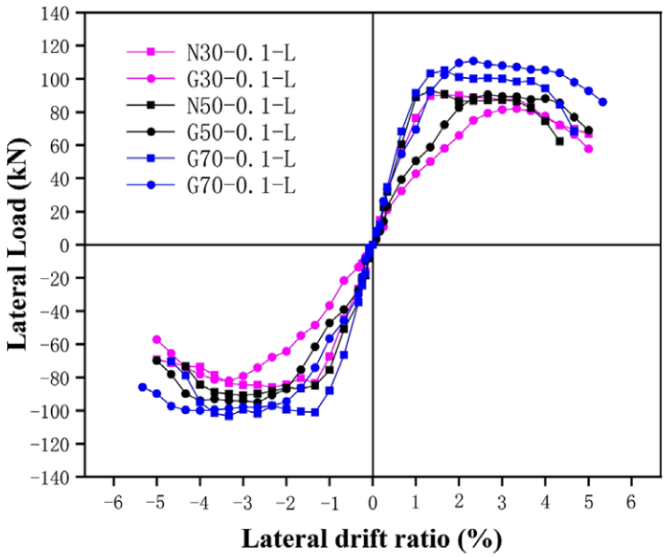

Figure 2-8 Envelop curves in Mao et al. (2022)

2.2.3 Field applications (structural uses)

(a) Precast bridge decks (Aldred and Day, 2012)

Geopolymer concrete has been used as precast bridge decks for constructing the bridge. In 2009, the Murraire Plane site bridge in Australia was constructed by using precast bridge decks made from geopolymer concrete. The bridge decks were prefabricated at the factory and installed on site. Another example is the Bundaleer Road Bridge in Australia, constructed in 2012. This bridge also used geopolymer concrete in constructing precast bridge decks.

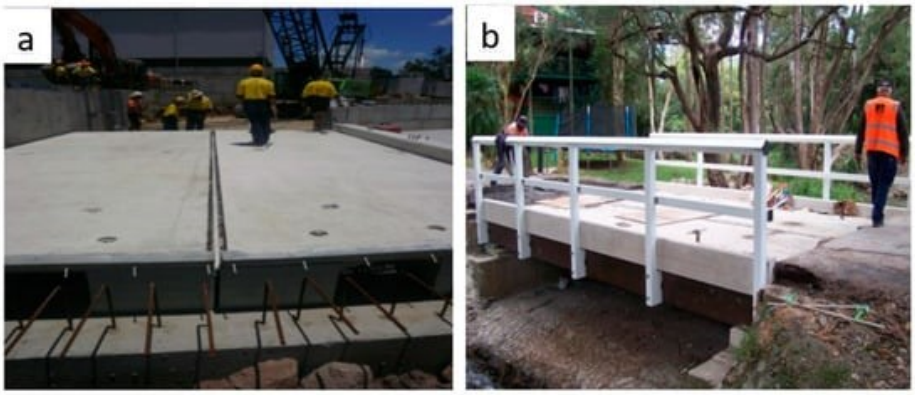

Figure 2-9 (a) The Murrarie Plane site bridge and (b) the Bundaleer Road bridge

(b) A small building (Sirividya et al., 2022)

Geopolymer concrete has been used in constructing a small building. The small building in India was constructed using geopolymer concrete

(a) Geopolymer concrete building, India

(b) The Global Change Institute, Australia

Figure 2-10 Geopolymer concrete buildings

(c) Precast beams of a multi-story building (Aldred and Day, 2012)

The Global Change Institute in Australia was investigated to be the first and only multi-story building which used geopolymer concrete as a structural material. Here, geopolymer concrete was used in constructing precast beams, whose span was 10.8 m in maximum. The building, constructed in 2013, has 4 stories and used 33 precast beams using geopolymer concrete.

(d) Footbridge (Concrete products, 2022)

Geopolymer concrete with fiber-reinforced polymer rebars was used to construct footbridges in Geelong, Australia. The engineers used carbon fiber-reinforced polymer for tension and glass fiber reinforced polymer for compression.

Figure 2-11 Geopolymer concrete footbridge

2.3 Grouted Splice Sleeve Connections

The cyclic loading tests of columns or beam-column connections with grouted splice sleeve connections showed various results on seismic performance. Some studies (Lu at el., 2017; Liu et al., 2016) reported equivalent or even superb seismic performance of the PC specimens to the monolithic specimen. On the other hand, some study (Ameli et al., 2015) reported inferior seismic performance of the PC specimens to the monolithic specimen. The relative compressive strength of grout to concrete used in the test specimens varied.

The locations of cracking were also variously reported. Some studies (Ameli et al., 2015; Liu et al., 2016) reported the cracks were concentrated on the interface between members. On the other hand, some study (Lu at el., 2017) reported the cracks occurred above the sleeves. The literature as to grouted splice sleeve connections were summarized as follows, which cover the invention (a), cyclic loading tests (b, c, d), the effect of grouting defects (e).

(a) Lin and Wu (2016)

Lin et al. summarize the invention of and the research work on splice sleeves. The authors state that splice sleeves were first invented in the 1970s to provide structural integrity between PC members. The fashion of splice sleeves was the same as today, which is to splice reinforcements of two different PC members by injecting non-shrinkage grout into the splice sleeve. The authors also mention that few researches have conducted cyclic loading tests for the seismic

performance of grouted splice sleeve connections.

(b) Lu at el. (2017)

Lu at el. conducted cyclic loading tests of 4 PC columns with sleeve connections and 2 monolithic columns. The column section was 500 mm width × 500 mm height, the loading height was 1150 mm, no axial compression was loaded on the top of the column. The average compressive strength of grout used in the test specimens was 144% higher than the average compressive strength of concrete (124 MPa for grout and 50.9 MPa for concrete).

The failure modes and the load-displacement relationship were equivalent between the PC and the monolithic specimens. The energy dissipation and ductility of the PC specimens were better than those of the monolithic specimens.

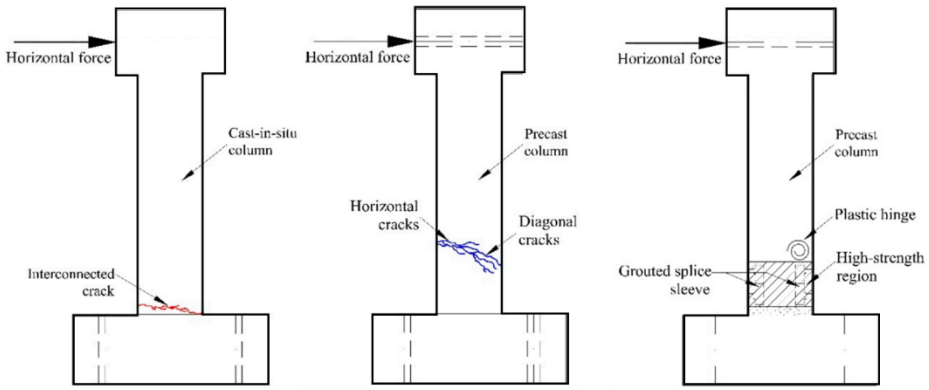

(a) Crack of monolithic specimen (b) Crack of precast specimen (c) Transfer of plastic hinge region

Figure 2-12 Different crack patterns of column specimens in Lu et al. (2017)

The location of cracks was different. Whereas the cracks of the monolithic specimens formed at the bottom of the column, the cracks of the PC specimens formed above the sleeves. The plastic hinge region moved upward due to the high strengths of the splice sleeves and the grout.

(c) Ameli et al. (2015)

Ameli et al. conducted cyclic loading tests of 2 PC column-to-cap beam joints with grouted splice sleeve connections and 1 monolithic column-to-cap beam joints. One of the PC specimens located the splice sleeves in the column, and the other PC specimen located the splice sleeves in the beam right under the column face. The column section was an octagonal shape with 533 mm width, the loading height was 2100 mm, the axial compression of 6% of the column crushing strength was loaded on the top of the column. The average compressive strength of grout used in the test specimens was 95% higher than the average compressive strength of concrete (81.3 MPa for grout and 41.6 MPa for concrete).

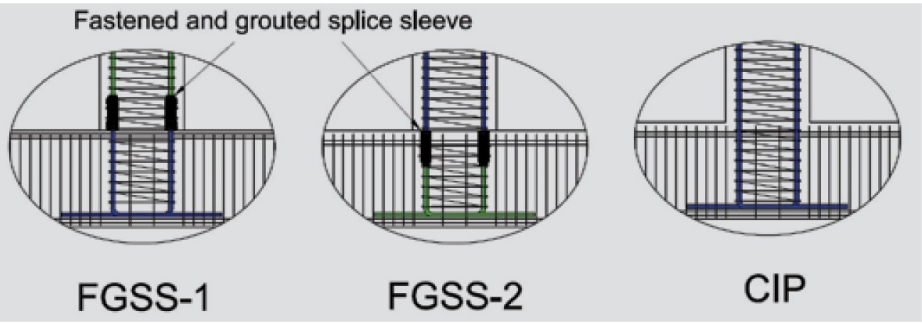

Figure 2-13 Test specimens of Ameli et al. (2015)

The load-displacement relationship and the ductility were superb in order of the monolithic specimen, the PC specimen with the sleeves in the beam, and the PC specimen with the sleeves in the column. In case of the PC specimen with the sleeves in the column, the damage was concentrated in the local region.

(d) Liu et al. (2016)

Liu et al. conducted cyclic loading tests of 2 PC beam-column connections with sleeve connections and 2 monolithic beam-column connections. The column section was 300 mm width × 300 mm height, and the beam section was 200 mm width × 300 mm height. The total height of the column was 2000 mm, the total length of the beam was 2300 mm. The axial compression of 30-40% of the column crushing strength was loaded on the top of the column. The 7^{th} day and 28^{th} day compressive strength of grout used in the test specimens (88.4 MPa and 100 MPa, respectively) was 185% and 223% higher than the compressive strength of concrete (31 MPa).

The PC specimens and the monolithic specimens showed the equivalent seismic performance in terms of load-displacement relationship, deformation capacity, and energy dissipation. However, the crack patterns were different between the PC specimens and the monolithic specimens. The cracks of the PC specimens were concentrated in the interface between the beam and the joint, while the cracks of the monolithic specimens were distributed along the beam.

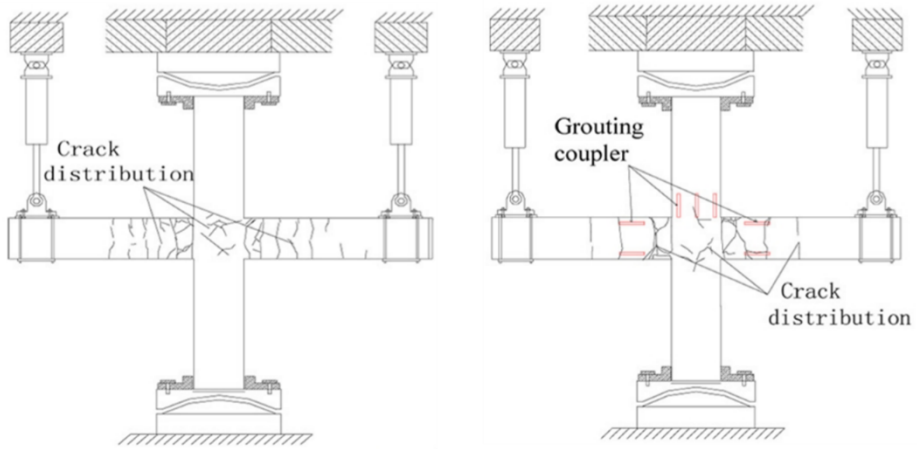

(a) Monolithic specimen (b) Precast concrete specimen

Figure 2-14 Different crack patterns of beam-column connection specimens in Lui et al. (2016)

(e) Xie et al. (2022)

Xie et al. investigated the effect of grouting defects by conducting cyclic loading tests of 5 PC column specimen with grouted splice sleeve connections; 1 without grouting defects, 2 with 45% and 60% grouting defects, and 2 with 45% and 60% grouting defects which were repaired.

The column section was 550 mm width × 550 mm height, the loading height was 2000 mm, and the axial compression of 25% of the column compressive strength was loaded on the top of the column. The average compressive strength of grout used in the test specimens was 105% higher than the average compressive strength of concrete (89 MPa for grout and 43.5 MPa for concrete).

The authors reported that the specimens with grouting defects showed two characters compared to the specimen without grouting defects. One was the bar

slip which occurred at the interface between the sleeves and the grout. As the gap opening was widened during cyclic loading, the rocking phenomenon was observed. The other was the pinching effect of the hysteresis curve. In the unloading phase, the hysteresis curves of the specimens with grouting defects were convex in the positive loading and concave in the negative loading, while that of the specimen without grouting defect was vice-versa. PC1-0 in **Figure 2-13** is the specimen without grouting defect, and the PC2-45 is the specimen with 45% grouting defect.

The seismic performance of the specimens with grouting defect were inferior to that of the specimens without grouting defect. They showed lower strength, energy dissipation, and deformation capacity.

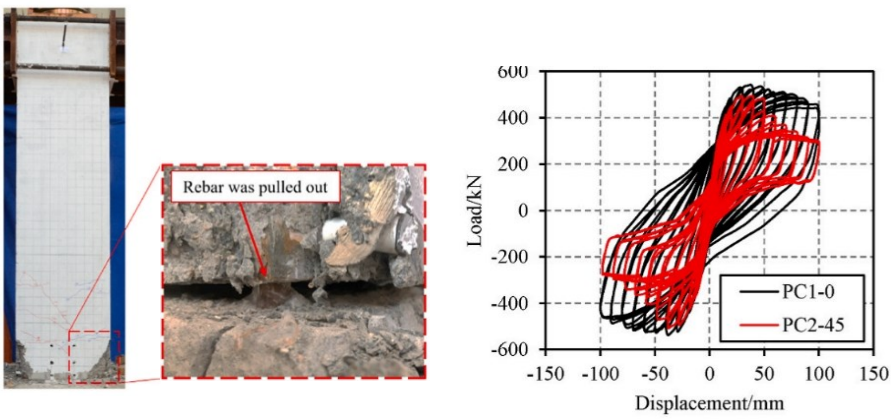

(a) Bar slip (b) Pinching effect

Figure 2-15 Characters of grouting defect in Xie et al. (2022)

2.4 Hooked Bars Terminated in Joint

Even though design codes denote that hooked bars should extend far to the opposite face of the joint, no study was found on the effect of overlap lengths of hooked bars terminated in a joint. Instead, proposed nominal strength models of exterior beam-column joints include the contribution of hooked bars terminated in a joint. Among 3 studies summarized below, 2 studies (Hwang and Lee, 1999; Pauletta et al., 2015) consider the point where the hooked bar is terminated to affect the nominal joint strength, and the other study (Park and Mosalam, 2012) implicitly assumes the hooked bar must extend to the far end.

(a) Hwang and Lee (1999)

Hwang and Lee proposed the softened strut-and-tie model to estimate nominal strengths of exterior joints. The model includes the contribution of diagonal strut, horizontal tie, and intermediate column reinforcements. Here, the angles of the struts are determined by the point where the hooked bar is terminated. The angles of the struts highly affect the nominal strength of the exterior joint; for example, the contribution of diagonal mechanism is calculated by $V_{jh,diag}=D\cos\theta$. Therefore, the point where the hooked bar is terminated affects the nominal strength of the joint.

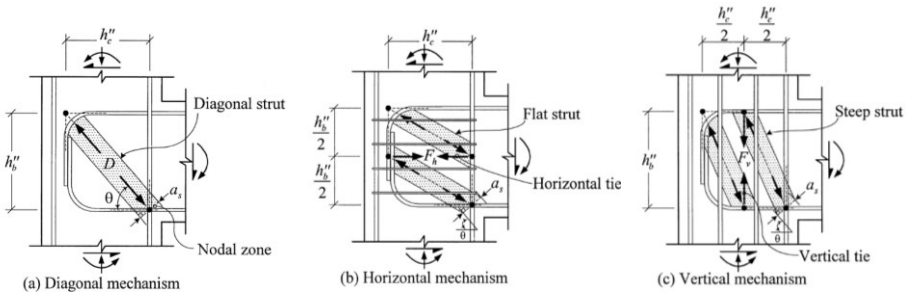

Figure 2-16 Softened strut-and-tie model of Hwang and Lee (1999)

(b) Park and Mosalam (2012)

Park and Mosalam proposed the assumed SAT model to estimate nominal strengths of exterior joints without joint transverse reinforcements. The model includes the contribution of two inclined struts in the joint, where one strut is caused by hook anchorage and the other strut by bond resistance. Here, the angles of the struts are not affected by where the hooked bar is terminated, but by the height of the column section. This means the assumption is behind the model that the hooked bar terminated in the joint must extend to the far end.

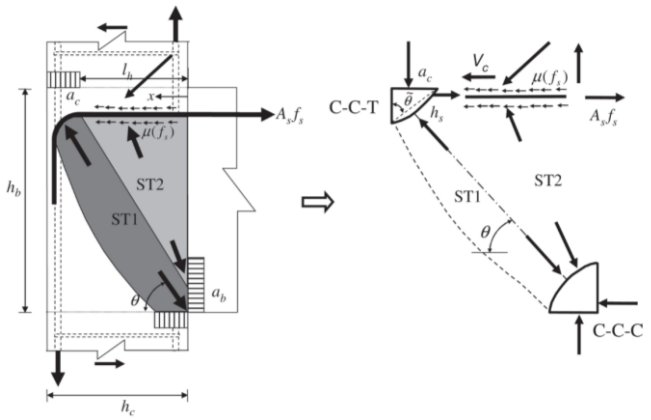

Figure 2-17 Assumed SAT model of Park and Mosalam (2012)

(c) Pauletta et al. (2015)

Pauletta et al. proposed the new strut-and-tie mechanism which mixed the model of Hwang and Lee (1999) and that of Park and Mosalam (2012). The model includes the contribution of two inclined struts, horizontal hoops, and intermediate column reinforcements. Here, the angles of the struts are determined by the point where the hooked bar is terminated.

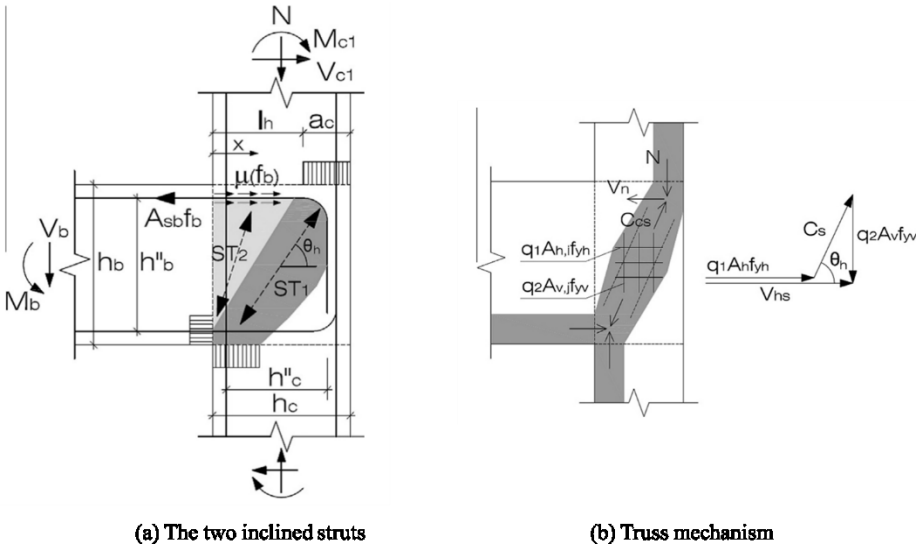

Figure 2-18 Strut-and-tie model of Pauletta et al. (2015)

Chapter 3. Material Performance of Geopolymer Concrete

3.1 Introduction

Geopolymer concrete has a large range of variations on materials and mix proportions. Depending on constituent materials and mix proportions of geopolymer concrete, the material performance can vary. Therefore, it is essential to quantify the material performance of the specific material used in this study.

In this chapter, material performance of the geopolymer concrete was investigated. The tests were conducted to investigate mechanical properties of the geopolymer concrete, including compressive strength, stress-strain curve, modulus of elasticity, strains at peak stress, modulus of rupture (i.e. flexural strength), and splitting tensile strength.

In each test, the standard-cured group and the ambient-cured group were tested. The standard-cured group was used to investigate the exact material performance of the geopolymer concrete, including the size effect. The ambient-cured group made during the structural tests was used to compare the material performance between the geopolymer concrete and the normal concrete.

3.2 Mixing and Curing

3.2.1 Mix proportion

Table 3-1 Mix proportion of geopolymer concrete and normal concrete

	Material	Geopolymer concrete	Normal concrete
Binder	Cement	- (0%)[1)]	305 (70%)
	GGBS[2)]	500 (100%)	130 (30%)
Alkaline activator	Ca-type composites[3)]	124.8	-
A/B ratio[4)]		25%	-
	Water	129	165
	Sand	759	805
	Coarse aggregate	862	978
	Agents	11.4	4

Unit : kg/m^3
1) Proportion among binder
2) GGBS : ground granulated blast-furnace slag
3) Ca-type composites: calcium-type-material-based activator
4) A/B ratio : activator-to-binder ratio

Table 3-1 shows mix proportion of the geopolymer concrete and the normal concrete used in this study. In the geopolymer concrete, instead of using cement, 100% GGBS was used as a binder material. As an alkaline activator, Ca-type composites were used, where the activator-to-binder ratio was 25%. In normal concrete, 70% cement and 30% GGBS were used as binder materials.

3.2.2 Curing condition

The geopolymer concrete was steam-cured. Being cured at the level of 20°C for 2-3 hours as a preconditioning time, the temperature increased from 20°C

to 35°C for 2 hours of heating time. Then, the temperature was maintained at 35°C for 8 hours. being ended by lowering temperature from 35°C to 20°C for 2 hours.

In the case of normal concrete, the same procedure of steam curing was conducted except the time and the temperature at the peak temperature. The peak temperature was maintained at 50-60°C for 6 hours.

3.3 Test Results of Material Performance

3.3.1 Compressive strength

Preparation of concrete cylinders followed KS F 2403, and compressive strength (f_c') tests followed KS F 2405. A total of 108 geopolymer and 15 normal concrete cylinders were manufactured and steam-cured for 8 hours and 6 hours, respectively. After then, curing condition varied; standard condition for exact material performance of the geopolymer concrete and ambient condition for structural test. The ambient-cured specimens, in this section, were used for relative comparison between the geopolymer concrete and the normal concrete. The test setting is shown in **Figure 3-1**.

50 geopolymer concrete cylinders were cured in standard condition in a steady-temperature-and-humidity chamber (20℃, 60-70% RH) to measure their strength in accordance with ages. The standard-cured cylinders consisted of 35 Ø100×200 mm cylinders and 15 Ø150×300 mm cylinders to find out the difference due to the size of the cylinder.

58 geopolymer and 15 normal concrete cylinders were cured in ambient condition and tested on the main testing date. In the case of cylinders without mention of sizes, they were made in a size of Ø100×200 mm.

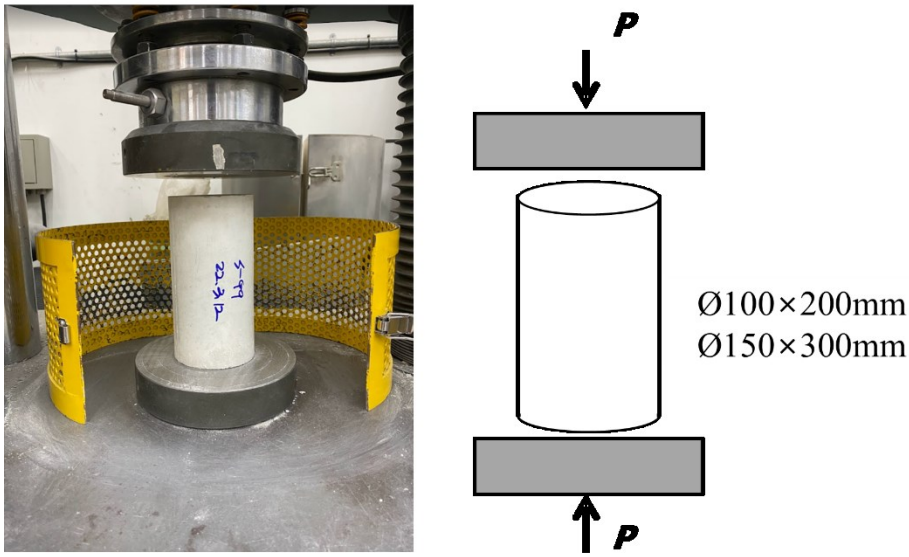

Figure 3-1 Setting of compressive strength test of concrete cylinder

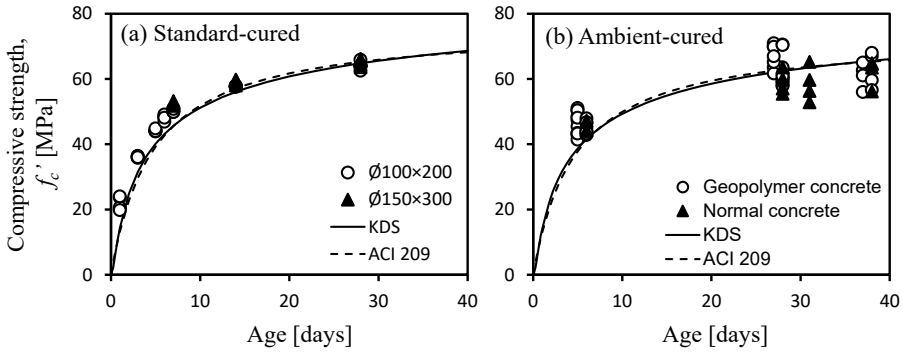

(a) Standard-cured (b) Ambient-cured

Figure 3-2 Compressive strength of geopolymer concrete cylinder

Figure 3-2 (a) shows the compressive strengths of the geopolymer concrete in accordance with ages which were cured in standard condition after 8 hours of steam curing. 5 cylinders were tested for each age. The average compressive strengths of Ø100×200 mm cylinders of day 1, 3, 5, 6, 7, 14, and 28 were 21.6, 36.1, 44.2, 48.2, 50.5, 58.0, and 64.2 MPa, respectively. The average compressive strengths of Ø150×300 mm cylinders of day 7, 14, and 28 were 52.4, 59.2, and 65.4 MPa, respectively, which were only 2-4% different from those of Ø100×200 mm cylinders.

Figure 3-2 (b) shows the compressive strengths of the geopolymer and normal concrete in accordance with ages which were cured in ambient condition together with the main test specimens after 8 or 6 hours of steam curing. The average compressive strengths of the geopolymer concrete cylinders of day 5, 6, and after day 28 were 46.6, 45.0, and 63.1 MPa, respectively. The average compressive strength of normal concrete cylinders of day 6 and after day 28 were 48.9 and 59.9 MPa, which was only 5% different from those of the geopolymer concrete cylinders.

Figure 3-2 compares the test strengths of the concrete cylinders with the equation predicting the strength of concrete in accordance with age (refer to **2.1 (b)**). The results show that the concrete cylinders regardless of concrete types well-follow the prediction of strength development. Here, the cement type 1 and moist curing condition are assumed ($\underline{\beta_{sc}}$ = 3.5, α = 4.0, β = 0.85).

3.3.2 Stress-strain curve

Figure 3-3 illustrates stress-strain curves of standard-cured geopolymer concrete with different sizes and ages. In ages of 7, 14, and 28, the graph includes 4 Ø100×200 mm cylinders and 4 Ø150×300 mm cylinders. The stress-strain curves of Ø100×200 mm cylinders were similar to the stress-strain curves of Ø150×300 mm cylinders regardless of ages.

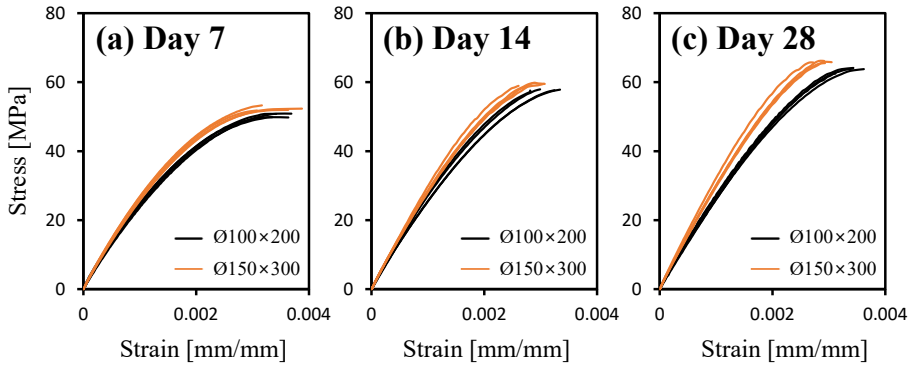

Figure 3-3 Stress-strain curves of standard-cured geopolymer concrete

Figure 3-4 compares stress-strain curves of ambient-cured geopolymer concrete with normal concrete. The graph includes 8 geopolymer concrete cylinders and 4 normal concrete cylinders with almost the same compressive strengths. The stress-strain curves of the geopolymer concrete cylinders showed little difference from the stress-strain curves of the normal concrete cylinders. This implies that the geopolymer concrete may be designed by the same concepts as cementitious concrete.

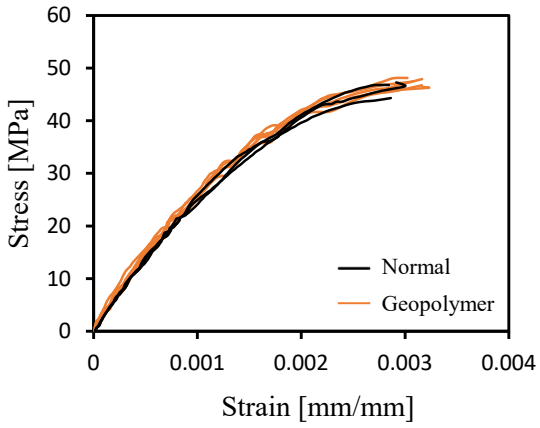

Figure 3-4 Stress-strain curves of ambient-cured geopolymer concrete

3.3.3 Modulus of elasticity

Figure 3-3 shows modulus of elasticity (E_c) of the geopolymer concrete from the previous compressive strength tests except day 1-6 standard-cured Ø100×200 mm cylinders. Modulus of elasticity was calculated by secant stiffness using 40% of maximum strength according to KS F 2438 and ASTM C469. 2 curves based on the current design codes were drawn together (**refer to 2.1 (a)**).

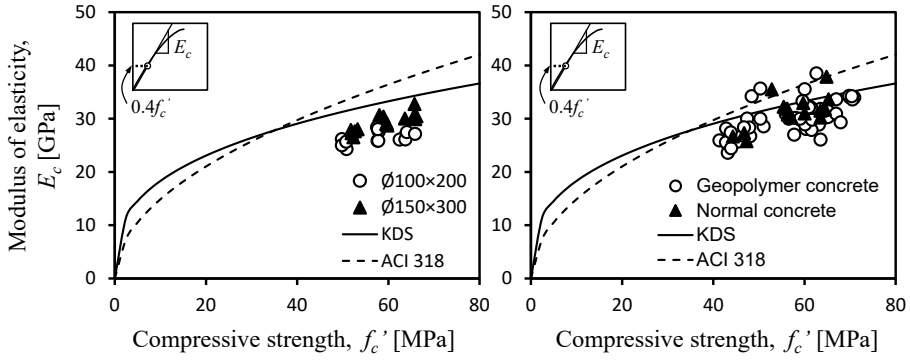

(a) Standard-cured (b) Ambient-cured

Figure 3-5 Modulus of elasticity of geopolymer concrete cylinder

Figure 3-3 (a) shows the modulus of elasticity of the geopolymer concrete with compressive strength which was cured in standard condition after 8 hours of steam curing. The modulus of elasticity of the standard-cured geopolymer concrete was 26.8 GPa (Ø 100×200 mm) and 30.7 GPa (Ø 150×300 mm) in average. The ratio of tested modulus of elasticity to KDS ($E_{c,test}/E_{c,KDS}$) was 81% (Ø 100×200 mm) and 88% (Ø 150×300 mm) in average. As to ACI 318, the ratio ($E_{c,test}/E_{c,ACI}$) was 74% (Ø 100×200 mm) and 81% (Ø 150×300 mm) in average.

Figure 3-3 (b) shows the modulus of elasticity of the geopolymer and normal concrete with compressive strength which was cured in ambient condition together with the main test specimens after 8 hours of steam curing. The ratio of tested modulus of elasticity to KDS ($E_{c,test}/E_{c,KDS}$) was 91% (geopolymer) and 96% (normal). As to ACI 318, the ratio ($E_{c,test}/E_{c,ACI}$) was 85% (geopolymer) and 88% (normal). Regardless of the concrete type, tested modulus of elasticity was lower than the equations of the design codes.

In **Figure 3-3**, the modulus of elasticity of both the geopolymer concrete and the normal concrete was 4-26% lower than the design codes. This low modulus of elasticity seems to be caused by the process of manufacturing concrete cylinders, not by material properties. This is supported by the low modulus of elasticity regardless of concrete type shown in **Figure 3-3 (b)**. When modulus of elasticity is low, stiffness may become low and deflection may become large.

3.3.4 Strain at peak stress

Figure 3-6 and **3-7** shows strains at peak stress (ε_o) of the geopolymer

concrete from the previous compressive strength tests. Excluded were 1-6 days standard-cured Ø100×200 mm geopolymer cylinders. **Figure 3-6** presents average strains at peak stress of each age.

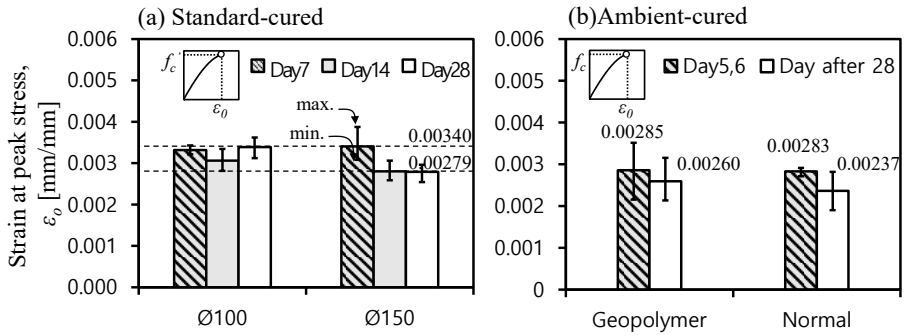

Figure 3-6 Strain at peak stress of geopolymer concrete cylinder - 1

Figure 3-6 (a) shows the strains at peak stress of the geopolymer concrete with the change of age which was cured in standard condition after 8 hours of steam curing. The average strains at peak stress of Ø100×200 mm cylinders of day 7, 14, and 28 were 0.00331 ($f_{c,avg}^{'}$=50.5 MPa), 0.00306 ($f_{c,avg}^{'}$=58.0 MPa), and 0.00339 ($f_{c,avg}^{'}$=64.2 MPa), respectively. The average strains at peak stress of Ø150×300 mm cylinders of day 7, 14, and 28 were 0.00340 ($f_{c,avg}^{'}$=52.4 MPa), 0.00280 ($f_{c,avg}^{'}$=59.2 MPa), and 0.00279 ($f_{c,avg}^{'}$=65.4 MPa), respectively. The average strains at peak stress of Ø150×300 mm cylinders were 82-103% of those of Ø100×200 mm cylinders. The strains at peak stress ranged from 0.00279 to 0.00340 ($f_{c,avg}^{'}$= 50.5-65.4 MPa).

Figure 3-6 (b) shows the strains at peak stress of the geopolymer and normal concrete with the change of age which was cured in ambient condition together

with the main test specimens after 8 or 6 hours of steam curing. The average strains at peak stress of the geopolymer concrete cylinders were 0.00285 ($f_{c,avg}^{'}$= 45.8 MPa on day 5,6) and 0.00260 ($f_{c,avg}^{'}$= 63.1 MPa on day after 28). The average strains at peak stress of normal concrete cylinders were 0.00283 ($f_{c,avg}^{'}$= 48.9 MPa on day 5,6) and 0.00237 ($f_{c,avg}^{'}$= 59.9 MPa on day after 28). The difference between concrete type was 1-9%.

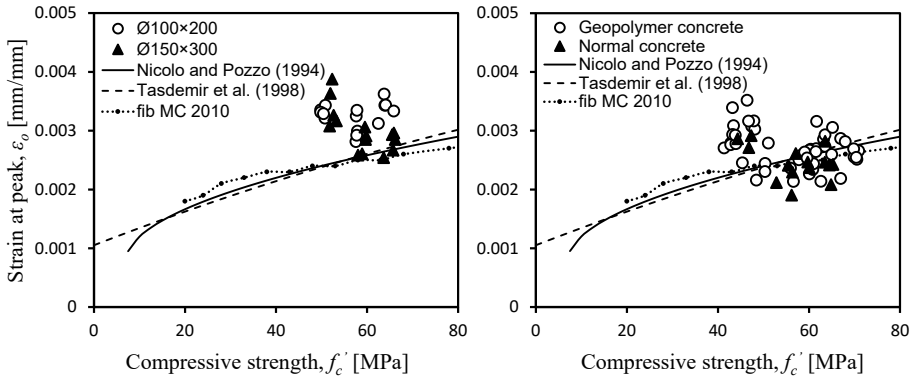

(a) Standard-cured (b) Ambient-cured

Figure 3-7 Strain at peak stress of geopolymer concrete cylinder - 2

Figure 3-7 presents average strains at peak stress versus compressive strength and compares it with proposed equations and a design code. Two of three curves are proposed equations of Nicolo and Pozzo (1994) and Tasdemir et al. (1998), respectively, and one curve is based on mechanical characteristics of concrete per *fib* MC 2010 (refer to **2.1 (c)**).

Figure 3-7 (a) shows strains at peak stress versus compressive strength of the standard-cured geopolymer concrete cylinders with different cylinder sizes. Compared with the proposed equations and the design code, the strains at peak stress of the geopolymer concrete was greater regardless of the cylinder size.

Figure 3-7 (b) shows strains at peak stress of the ambient-cured geopolymer and normal concrete cylinders. The strains at peak stress of both concrete types showed similar tendency. Some specimens showed large strains as the standard-cured geopolymer concrete specimens did.

The reason why strains at peak stress of the specimens was greater than the proposed equations and the design code may be induced by low modulus of elasticity. As shown in **Figure 3-8**, the low modulus of elasticity probably caused by the process of manufacturing concrete cylinders (**Figure 3-5**) might change the shape of strain-stress curve when compressive strength was the same. As the peak stress developed later, the strain of the specimen might be large.

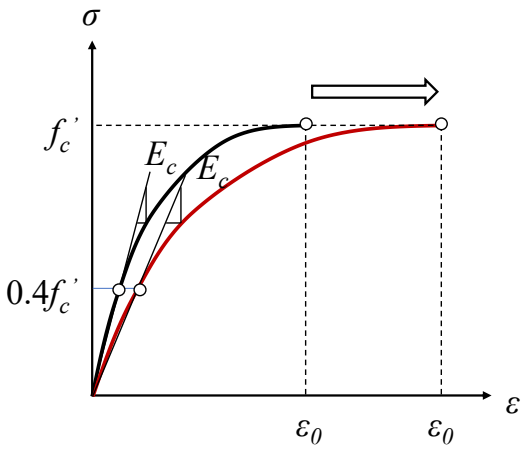

Figure 3-8 Change of strain-stress curve

This seems to be caused not by the properties of the material but by the process of manufacturing concrete cylinders, which is supported by the fact that both concrete types showed similar tendency. When strains at peak stress of concrete in a building is large, the risk of cracking may become high in the

serviceability state.

3.3.5 Modulus of rupture (i.e. flexural strength)

Preparing concrete specimens followed KS F 2403, and modulus of rupture (f_r; i.e. flexural strength) tests followed KS F 2408. A total of 21 geopolymer and 3 normal concrete specimens were manufactured and steam-cured for 8 hours and 6 hours, respectively. After then, curing condition varied. The test setting is shown in the **Figure 3-7**. 3 curves based on the current design codes and the proposed equation were drawn together (refer to **2.1 (d)**).

15 geopolymer concrete specimens were cured in standard condition in a steady-temperature-and-humidity chamber (20℃, 60-70% RH) to measure their strength with the change of age. 6 geopolymer and 3 normal concrete specimens were cured in ambient condition and tested on the main testing date.

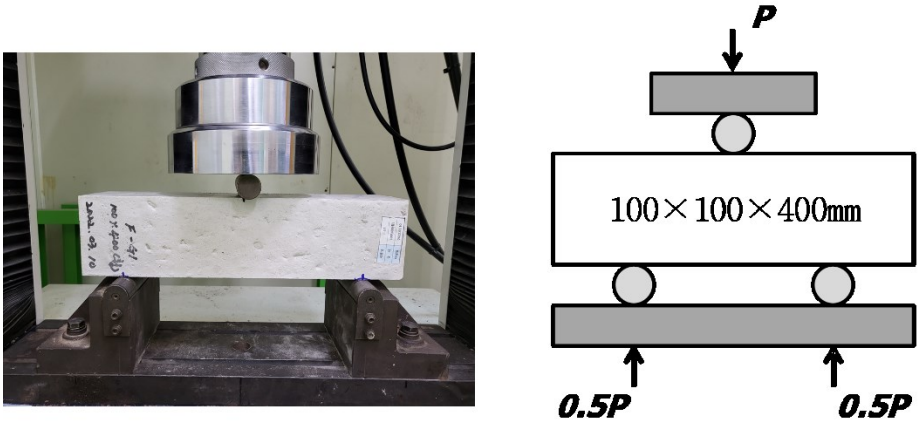

Figure 3-9 Setting of modulus of rupture test of concrete cylinder

Figure 3-8 (a) shows the modulus of rupture of the geopolymer concrete with the change of age which was cured in standard condition after 8 hours of steam curing. 5 specimens were tested for each age. The average modulus of rupture of 7, 14, and 28 days were 5.82, 5.96, and 6.06 MPa, respectively, slightly increasing with the change of concrete age.

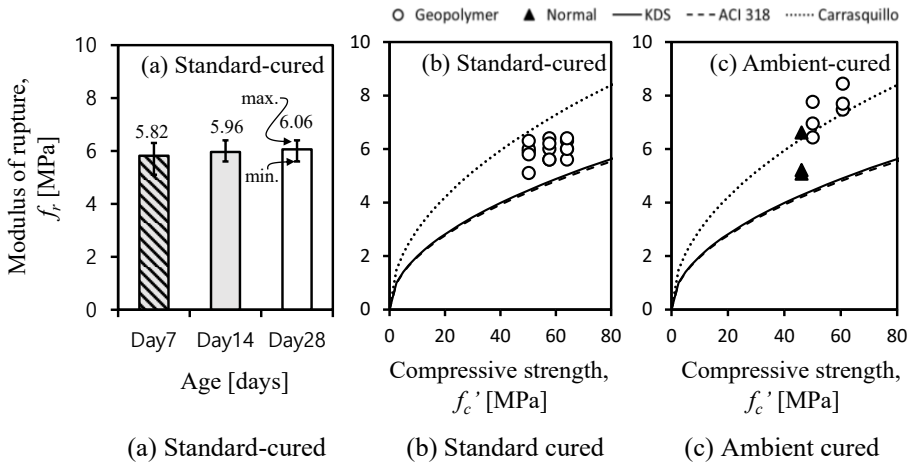

Figure 3-10 Modulus of rupture of geopolymer concrete cylinder

Figure 3-8 (b) shows the modulus of rupture of the geopolymer concrete with compressive strength which was cured in standard condition after 8 hours of steam curing. The ratio of tested modulus of rupture to KDS ($f_{r,test}/f_{r,KDS}$) was 125%, and the ratio to ACI 318 ($f_{r,test}/f_{r,ACI}$) was 127% in average.

Figure 3-8 (c) shows the modulus of rupture of the 6 geopolymer and the 3 normal concrete with compressive strength which was cured in ambient condition together with the main test specimens after 8 or 6 hours of steam curing. The ratio of tested modulus of rupture to KDS ($f_{r,test}/f_{r,KDS}$) was 159% (geopolymer) and 132% (normal) in average. As to ACI 318, the ratio ($f_{r,test}/f_{r,ACI}$) was 162% (geopolymer) and 134% (normal) in average. Regardless of the

concrete type, tested modulus of rupture was higher than the equations of the design codes.

Figure 3-8 (b), (c) include not only the equations of the design codes but also the proposed equation of Carrasquillo. Legeron and Paultre (2000) demonstrated that the proposed equation of Carrasquillo represented the average relation of modulus of rupture of concrete and compressive strength and that ACI 318 equation highly underestimated the modulus of rupture of concrete.

3.3.6 Splitting tensile strength

Preparing concrete cylinders followed KS F 2403, and splitting tensile strength (f_{sp}) tests followed KS F 2423. A total of 70 geopolymer and 6 normal concrete cylinders were manufactured and steam-cured for 8 hours and 6 hours, respectively. After then, curing condition varied. The test setting is shown in **Figure 3-9**. 2 curves based on the design codes were drawn together (refer to **2.1 (e)**).

30 geopolymer concrete cylinders were cured in standard condition in a steady-temperature-and-humidity chamber (20℃, 60-70% RH) to measure their strength with the change of age. The standard-cured cylinders consisted of 15 Ø100×200 mm cylinders and 15 Ø150×200 mm cylinders to find out the difference due to the size of the cylinder.

40 geopolymer and 6 normal concrete cylinders were cured in ambient condition and tested on the main testing date. The ambient-cured geopolymer

concrete cylinders consisted of 20 Ø100×200 mm cylinders and 20 Ø150×200 mm cylinders. The ambient-cured normal concrete cylinders consisted of 3 Ø100×200 mm cylinders and 3 Ø150×200 mm cylinders.

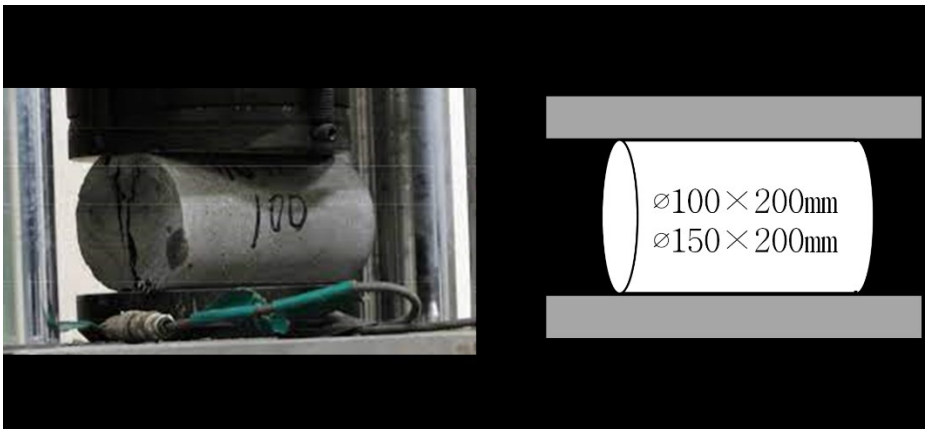

Figure 3-11 Setting of splitting tensile strength test of concrete cylinder

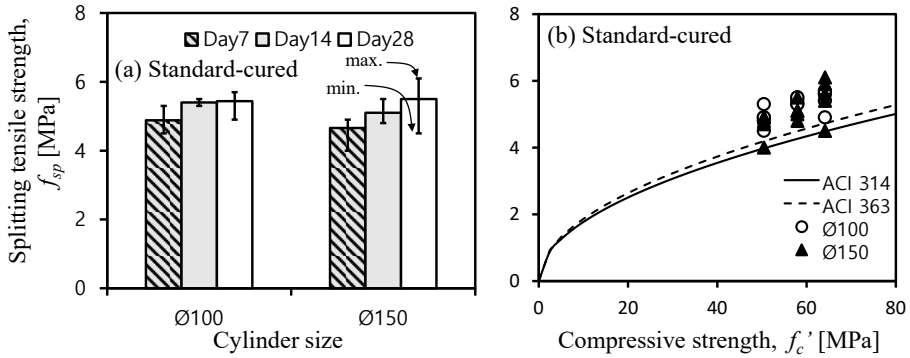

(a) Standard-cured (b) Standard-cured

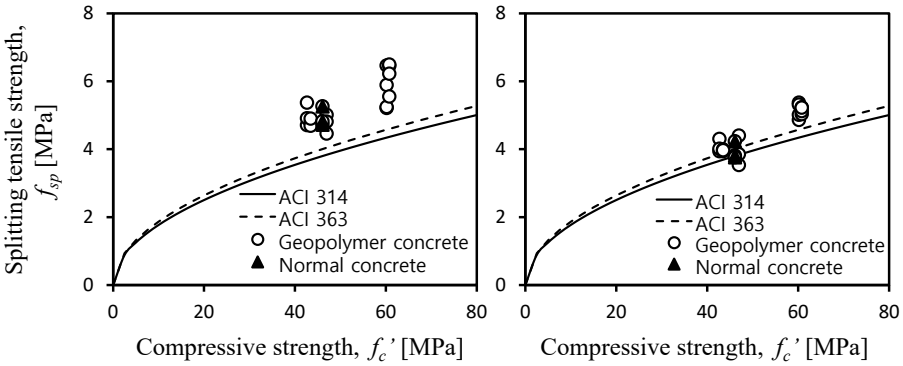

(c) Ambient-cured (Ø100) (d) Ambient-cured (Ø150)

Figure 3-12 Splitting tensile strength of geopolymer concrete cylinder

Figure 3-10 (a) shows the splitting tensile strength of the geopolymer concrete with the change of age which was cured in standard condition after 8 hours of steam curing. 5 specimens were tested for each age. The average splitting tensile strengths of Ø100×200 mm cylinders of 7, 14, and 28 days were 4.88, 5.4, and 5.44 MPa, respectively. The average splitting tensile strengths of Ø150×200 mm cylinders of 7, 14, and 28 days were 4.66, 5.10, and 5.5 MPa, respectively. As the concrete age increased, splitting tensile strength increased. The difference between cylinder sizes was only 1-5%.

Figure 3-10 (b) shows the splitting tensile strength of the geopolymer concrete with compressive strength which was cured in standard condition after 8 hours of steam curing. The ratio of tested splitting tensile strength to ACI 318 ($f_{sp,test}/f_{sp,318}$) was 124% (Ø100×200) and 120% (Ø150×200) in average. As to ACI 363, and the ratio ($f_{sp,test}/f_{sp,363}$) was 117% (Ø100×200) and 114% (Ø150×200) in average. Regardless of the size of the cylinder, tested splitting tensile strength was higher than the equations of the design codes.

Figure 3-10 (c) shows the splitting tensile strength of Ø100×200 the geopolymer and normal concrete with compressive strength which was cured in ambient condition together with the main test specimens after 8 or 6 hours of steam curing. The ratio of tested splitting tensile strength to ACI 318 ($f_{sp,test}/f_{sp,318}$) was 132% (geopolymer) and 130% (normal) in average. As to ACI 363, and the ratio ($f_{sp,test}/f_{sp,363}$) was 126% (geopolymer) and 123% (normal) in average. Regardless of the concrete type, tested splitting tensile strength was higher than the equations of the design codes.

Figure 3-10 (d) shows the splitting tensile strength of Ø150×200 geopolymer and normal concrete with compressive strength which was cured in ambient condition together with the main test specimens after 8 or 6 hours of steam curing. The ratio of tested splitting tensile strength to ACI 318 ($f_{sp,test}/f_{sp,318}$) was 111% (geopolymer) and 103% (normal) in average. As to ACI 363, and the ratio ($f_{sp,test}/f_{sp,363}$) was 105% (geopolymer) and 98% (normal) in average. Regardless of the size of the cylinder, tested splitting tensile strength was higher than the equations of the design codes in overall.

3.4 Summary

In this chapter, material performance of the geopolymer concrete was investigated. The geopolymer concrete consisted of the binder with 100% GGBS and alkaline activator (Ca-type composites). The normal concrete for control specimen consisted of the binder with 70% cement and 30% GGBS. The geopolymer concrete was steam-cured after casting at 35°C for 8 hours. The normal concrete was also steam-cured at 50-60°C for 6 hours.

The tests were conducted to investigate material performance of the geopolymer concrete, including compressive strength, stress-strain curve, modulus of elasticity, strains at peak stress, modulus of rupture (i.e. flexural strength), and splitting tensile strength. In each test, the standard-cured group and the ambient-cured group were tested. The standard-cured group was used to investigate the exact material performance of the geopolymer concrete, including the size effect. The ambient-cured group made during the structural tests was used to compare the material performance between the geopolymer and the normal concrete.

In overall, the geopolymer concrete had equivalent material performance to the normal concrete or exceeded the equations of the design codes. The major findings are summarized as follows:

1) The compressive strengths of the standard-cured geopolymer concrete on day 7, 14, and 28 were 50.5, 58.0, and 64.2 MPa, respectively (Ø100×200 mm) and 52.4, 59.2, and 65.4 MPa, respectively (Ø150×300 mm). In the ambient-cured group, the compressive strength of the geopolymer and the

normal concrete was only 5% different.

2) The stress-strain curves of standard-cured geopolymer concrete were similar in different size of cylinders. The stress-strain curves of the ambient-cured geopolymer concrete cylinders showed little difference from the stress-strain curves of the normal concrete cylinders.

3) The ratio of tested modulus of elasticity of the standard-cured geopolymer concrete to KDS ($E_{c,test}/E_{c,KDS}$) was 81% (Ø100×200 mm) and 88% (Ø 150×300 mm) in average. As to ACI 318, the ratio ($E_{c,test}/E_{c,ACI}$) was 74% (Ø100×200 mm) and 81% (Ø150×300 mm) in average. In the ambient-cured group, regardless of the concrete type, the tested modulus of elasticity was 9-15% (geopolymer) and 5-12% (normal) lower than the equations of the design codes.

4) The average strains at peak stress of the standard-cured geopolymer concrete ranged from 0.00279 to 0.00340. In the ambient cured group, the average strains at peak stress of the geopolymer concrete was 1-9% different from that of the normal concrete.

5) The modulus of rupture (i.e. flexural strength) of the standard-cured geopolymer concrete on day 7, 14, and 28 was 5.82, 5.96, and 6.06 MPa, where the ratio of tested modulus of rupture to KDS ($f_{r,test}/f_{r,KDS}$) was 125%, and the ratio to ACI 318 ($f_{r,test}/f_{r,ACI}$) was 127% in average. In ambient-cured group, regardless of the concrete type, the tested modulus of rupture were higher than the equations of the design codes.

6) The splitting tensile strengths of the standard-cured geopolymer concrete

on day 7, 14, and 28 were 4.88, 5.40, and 5.44 MPa, respectively (Ø100×200 mm) and 4.66, 5.10, and 5.5 MPa, respectively (Ø150×200). Regardless of the size of the cylinder, the tested splitting tensile strengths were 14-24% higher than the equations of ACI 314 and ACI 363. Regardless of concrete type and cylinder size, the tested splitting tensile strengths were higher than the equations of the design codes.

Chapter 4. Cyclic Loading Tests for Columns

4.1 Introduction

Only few studies have been reported on the seismic performance of geopolymer concrete members by cyclic loading tests, and no study was found on the cyclic loading tests of columns. The results of the studies varied in terms of seismic performance, and the studies adopted various properties of materials including the type of binder materials and the amount of the activator solution.

And also, the cyclic loading tests of columns or beam-column connections with grouted splice sleeve connections showed various results on seismic performance. The locations of cracking were also variously reported. Therefore, both geopolymer concrete columns and splice sleeve connections need to be investigated regarding seismic performance.

In this chapter, cyclic loading tests were conducted to investigate seismic performance of the PC columns using the geopolymer concrete. The structural performance of the geopolymer concrete columns was evaluated by whether the specimens developed nominal strengths calculated by design codes. The test results of the geopolymer concrete specimens were compared with those of the normal concrete specimens in terms of seismic performance.

Moreover, the seismic performance of splice sleeve connections was evaluated by comparing PC specimens with monolithic specimen. The effect of sizes of sleeves was covered. Furthermore, the seismic performance of each

specimen was evaluated by ACI 374.1-05 and AIJ 2022 Guidelines.

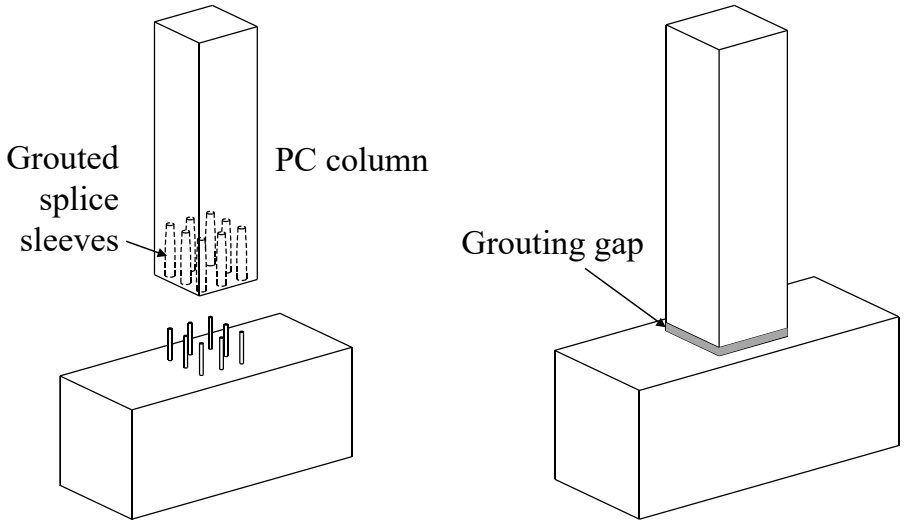

Figure 4-1 PC column with grouted splice sleeve connection

4.2 Test Plan

4.2.1 Test parameters

Table 4-1 shows the test parameters of column specimens, such as concrete types, construction methods, sizes of sleeves, reinforcement ratio, and transverse rebar spacing. In the specimen names, the letters 'N' and 'G' denote concrete types; the normal concrete and the geopolymer concrete, respectively. The letter 'IMP' denotes imperfection in manufacturing test specimens especially in grouting.

Table 4-1 Test parameters of column specimens

Specimen	Concrete type	Construction method	Sleeve size[1)]	Rebar size	ρ[2)]	s[3)] (mm)
C-N1	Normal	Monolithic	-	D25	0.0162	200
C-N2	Normal	PC	D25	D25	0.0162	200
C-G1	Geopolymer	PC	D25	D25	0.0162	200
C-G2	Geopolymer	PC	D32	D32	0.0254	200
C-G3	Geopolymer	PC	D29	D25	0.0162	200
C-G1-IMP	Geopolymer	PC	D25	D25	0.0162	200
C-G4-IMP	Geopolymer	PC	D25	D25	0.0162	100

1) Standard diameters of a reinforcement inserted inside a sleeve.
2) Reinforcement ratio
3) Spacing of transverse reinforcements

The specimens can be grouped by the two control specimens (C-N1 and C-N2) and the five experimental specimens (C-G1, C-G2, C-G3, C-G1-IMP, C-G4-IMP). One of the control specimens, C-N1, was monolithically made and the other, C-N2, was constructed as PC members and connected by splice sleeve connection. All of them were made of the normal concrete. On the other hand, the experimental specimens were made of the geopolymer concrete. One of the experimental specimens, C-G1, was constructed by the same method as the PC

control specimen except using the geopolymer concrete. C-G2 used higher reinforcement ratio with larger-sized rebars and sleeves. C-G3 used the larger-size sleeves while maintaining the size of longitudinal reinforcements. C-G1-IMP was constructed the same as C-G1 but unintentionally manufactured with imperfection in grouting. C-G4-IMP used halved spacing of transverse reinforcements but also manufactured with grouting imperfection.

4.2.2 Details of test specimens

Figure 4-2 shows details of test specimens for cyclic loading column tests under the constant axial load. The column specimens were composed of the column and the base. The section of the column was 500 mm width × 500 mm height and the section of the base was 800 mm width × 800 mm height. The total height of the columns was 1900 mm and the shear span from the face of the base to the loading point was 1500 mm. The total length of the bases was 1900 mm and the net length between reaction points was 1500 mm.

Figure 4-2 (a) shows the PC specimens. They were made of two separate PC members (column and base) and then connected by splice sleeve connections. The base was made of normal concrete and the column was made of either normal or geopolymer concrete. The 50-mm grouting gap was located between the face of the base and the column to consider a construction error and enhance the connectivity. D13 hoops and crossties (bar diameter d_b = 12.9 mm and yield strength f_y = 620.0 MPa for C-N1, C-N2, C-G2, C-G1-IMP, and C-G4-IMP; f_y = 571.3 MPa for C-G1 and C-G3) were arranged in the column, starting from 70–90 mm apart from the grouting gap. Their spacing was 200 mm (≒ d/2),

and in case of C-G4-IMP it was 100 mm (≒ d/4). The spacing was closer (50 mm) near the loading point to prevent local shear failure, and in the sleeve zone the spacing was about 75 mm to prevent transverse reinforcements from being unfastened. In overall, the PC specimens followed typical PC reinforcement details using splice sleeves for ordinary moment frames (for moment frame, refer to **2.1 (h)**).

Figure 4-2 (b) shows the monolithic specimen. The column and the base were made monolithically together. It was made of normal concrete. The spacing of D13 hoops and crossties in the column was 200 mm (≒ d/2), but near the loading point, 50 mm to prevent local shear failure. They started from 100 mm (= s/2) apart from the face of the base. The monolithic specimen was designed as an ordinary moment frame without seismic details.

Figure 4-2 (c) shows the section A-A of the columns, which represents the connection details between the column and the base. In C-N1, eight D25 bars (bar diameter d_b = 25.4 mm and yield strength f_y = 661.1 MPa for C-N1, C-N2, C-G1-IMP, C-G4-IMP; f_y = 646.4 MPa for C-G1 and C-G3) were used for the longitudinal reinforcements without sleeves. In C-N2, C-G1, C-G1-IMP, C-G4-IMP, D25 bars and D25 sleeves were used, in C-G3, D25 bars and D29 sleeves, and in C-G2, D32 bars (bar diameter d_b = 32.3 mm and yield strength f_y = 636.0 MPa) and D32 sleeves were used.

Figure 4-2 (c) also shows the details of column transverse reinforcements and the concrete cover. The hoops and the crossties in the columns were designed with 135° hook anchorage at one end and 90° at the other end. The

target value of concrete cover was 30 mm from the concrete surface to the transverse reinforcement confining the sleeves, which resulted in the slightly different locations of the longitudinal reinforcements of each test specimens.

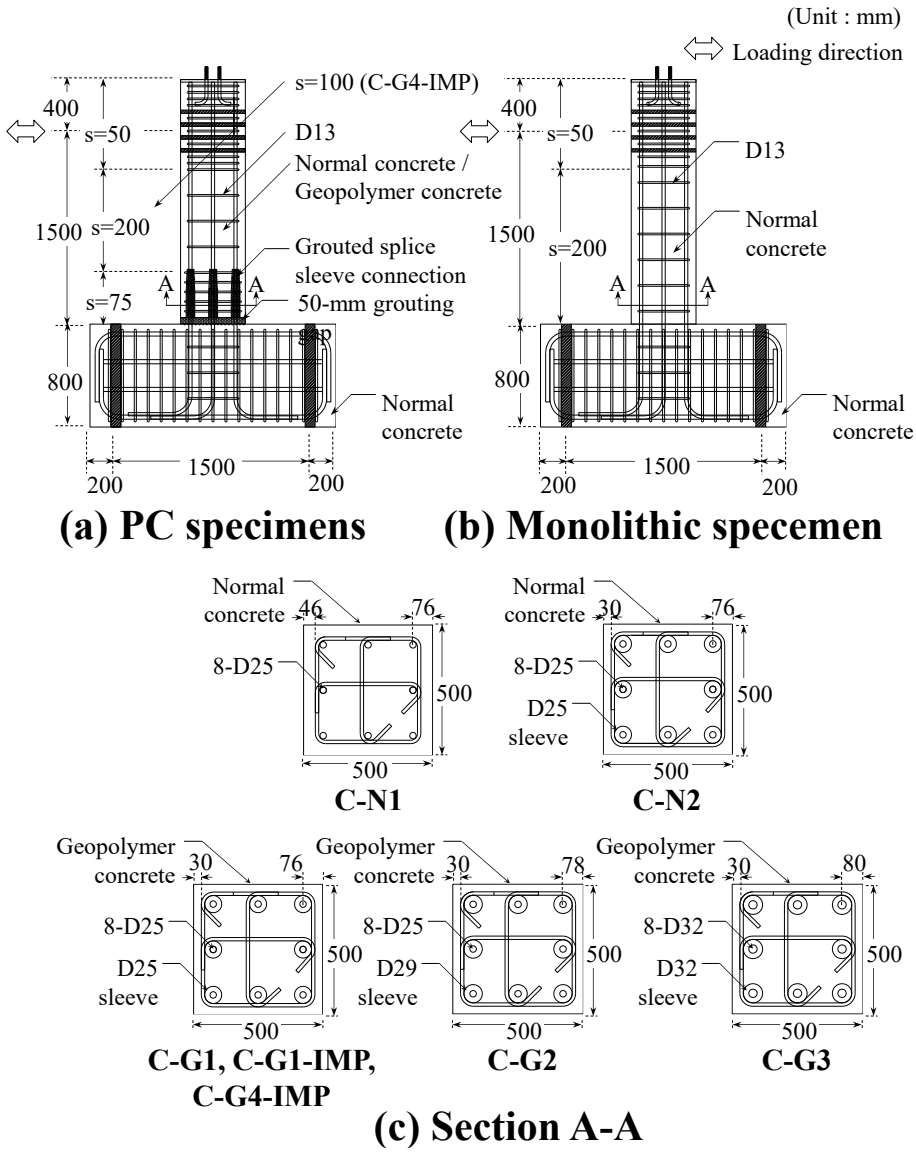

Figure 4-2 Details of column specimens

4.2.3 Specimen construction

The construction of the column specimens can be divided into three parts: base construction, column construction, and column-base connection. The procedures of the construction are illustrated in **Figure 4-3** to **4-5**.

(a) Assembling steel cages · Attaching strain gauges · Manufacturing mold

(b) Placing concrete

Figure 4-3 Construction procedures of column specimens: base construction

(a) Assembling steel cages

(b) Attaching strain gauges

Figure 4-4 Construction procedures of column specimens: column construction

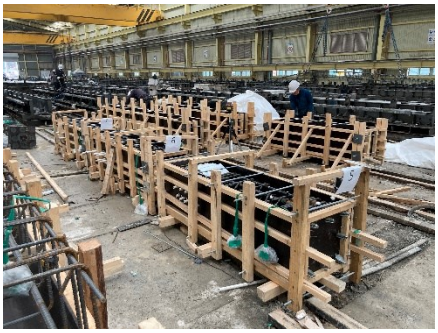

(c) Manufacturing mold

(d) Placing concrete and curing

Figure 4-4 Construction procedures of column specimens: column construction (continued)

(a) Before assembling

(b) Column-base assembling and manufacturing mold

(c) Injecting non-shrinkage grout

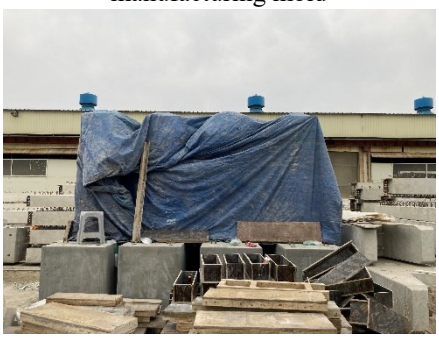

(d) Curing

Figure 4-5 Construction procedures of column specimens: the column-base connection

4.2.4 Grouted splice sleeves

In this study, three sizes of sleeves were used, D25, D29, and D32. As the standard size of a rebar inserted into a sleeve increases, the total length and the insertion length also increase. Inside the sleeves, non-shrinkage grout was injected to fill a void and integrate the members. The total lengths and the insertion lengths of each sleeve used in the study were summarized in **Table 4-2**.

Table 4-2 Lengths of sleeves used in the study

Sleeve size	Insertion length (mm)		Total length (mm)
	Upper	Lower	
D25	170	180	375
D29	190	210	430
D32	220	240	480

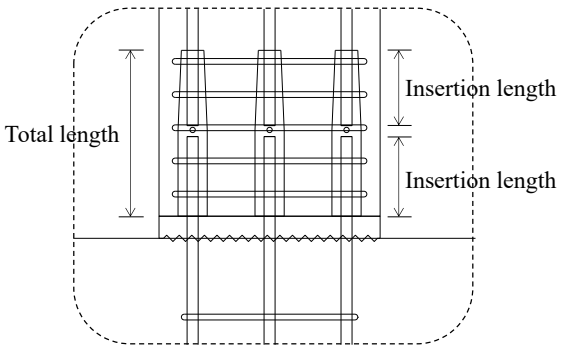

(a) Lengths of splice sleeve

(b) Sleeves used in the study

Figure 4-6 Grouted splice sleeves

4.2.5 Material strength

Figure 4-7, 4-8 and **Table 4-3**, **4-4** show the material strength tests and the resulting material strengths. When placing concrete, concrete cylinders (100 mm diameter × 200 mm height) were prepared for compressive test per KS F

2403. They were cured under the same condition as that of the test specimens. The compressive tests of concrete cylinder were conducted on each day of the structural tests as shown in **Figure 4-7 (a)**. The speed of loading was 0.4 MPa/s by the load control method per KS F 2405. On the both sides of the cylinders, concrete strain gauges were attached to measure strains. The compressive strengths of concrete cylinders of each test specimen are shown in **Table 4-3**.

When grouting, non-shrinkage grout specimens (40 mm × 40 mm × 160 mm) were prepared for compressive tests per KS F 2403. The compressive tests of non-shrinkage grout specimens were conducted as shown in **Figure 4-7 (b)**. The speed of loading was 1 mm/s by the displacement control method per KS F 4044. Concrete strain gauges were attached on the both sides to measure strains. The average compressive strengths of the non-shrinkage grout of the test specimens are shown in **Table 4-3**.

When assembling steel cages, steel rebar specimens (600 mm length, in case of D32, 700 mm length) cut from the rebars used for manufacturing the test specimens were prepared for tensile test per KS B 0801. The steel rebar tensile tests were conducted as shown in **Figure 4-7 (c)**. The speed of loading was 2 mm/s by the displacement control method, and after the rebars yielded, gradually increased up to 8 mm/s per KS B 0802. On the center of the steel rebar specimens, steel strain gauges were attached to measure strains. The material strengths and the stress-strain relationships of steel rebars of the test specimens are shown in **Table 4-4** and **Figure 4-8**, respectively.

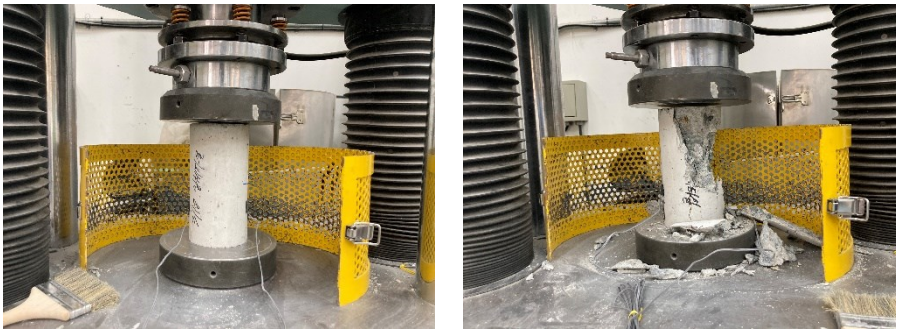

(a) Concrete cylinder compressive test

(b) Non-shrinkage grout compressive test

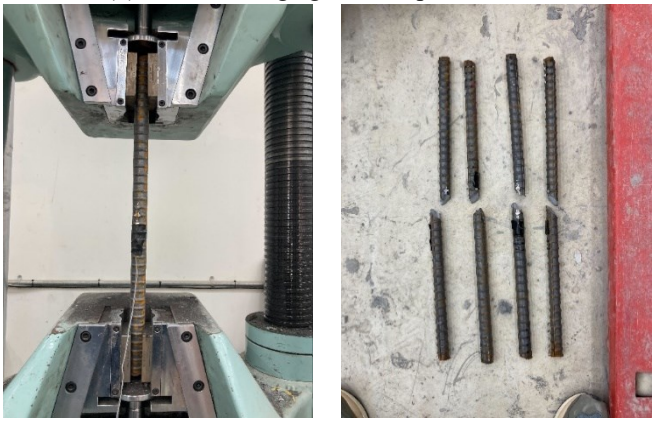

(c) Steel rebar tensile test

Figure 4-7 Material strength tests of columns

Table 4-3 Compressive material strength test results of columns

Specimen	Average compressive strength, f_c' (MPa)
C-N1	59.5
C-N2	59.5
C-G1	69.4
C-G2	60.4
C-G3	70.5
C-G1-IMP	63.5
C-G4-IMP	60.4
Base	80.1
Non-shrinkage grout	75.0 (for C-N1, C-N2, C-G2, C-G1-IMP, C-G4-IMP) 83.7 (for C-G1, C-G3)

Table 4-4 Tensile material strength test results of columns

Rebar	Bar diameter d_b (mm)	Specimen	Yield strength f_y (MPa)	Ultimate strength f_u (MPa)	Yield strain ε_y (mm/mm)
SD500 D13	12.9	C-N1 C-N2 C-G2 C-G1-IMP C-G4-IMP	620.0	725.4	0.00310
		C-G1 C-G3	571.3	675.6	0.00286
SD600 D25	25.4	C-N1 C-N2 C-G1-IMP C-G4-IMP	661.1	784.5	0.00331
		C-G1 C-G3	646.4	775.2	0.00323
SD600 D32	32.3	C-G2	636.0	772.3	0.00318

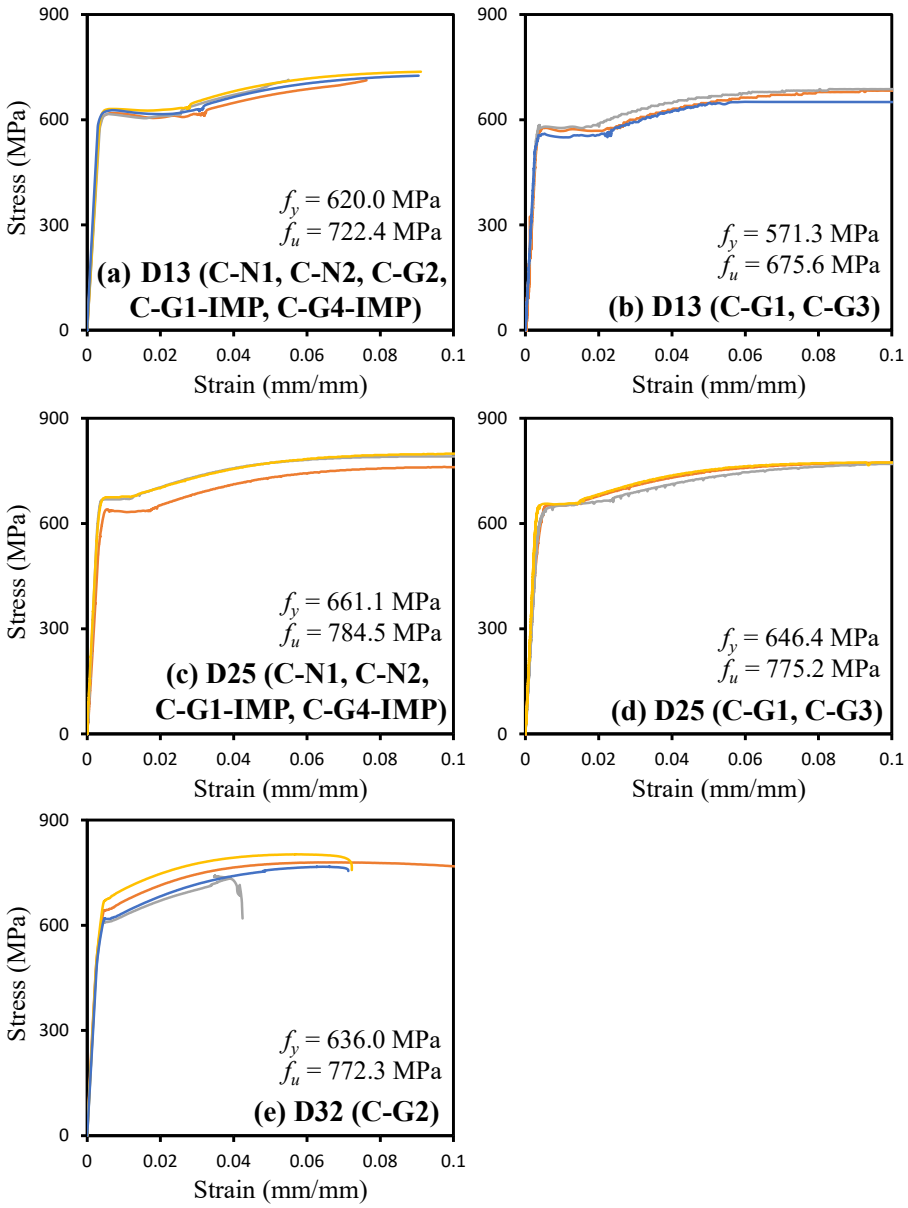

Figure 4-8 Tensile material strength test results of columns

4.2.6 Test setup and loading plan

Figure 4-9 illustrates the test setup for cyclic loading tests of the column specimens under constant axial load. Firstly, 13% of the compressive strength of the concrete section was loaded on the top of each column specimen, which simulated building load effect acting to a column. Here, 3,000 kN hydraulic machine was used. With constant axial load acting, cyclic lateral loading simulated earthquake load acting to a column. Here, 2,000 kN actuator was used.

The loading plan of the beam-column connection tests followed ACI 374.1-05, and is illustrated in **Figure 4-10** and **Table 4-5**. ACI 374.1-05 recommends that each step include three cycles and an incremental ratio of displacements be in a range from 1.25 to 1.5.

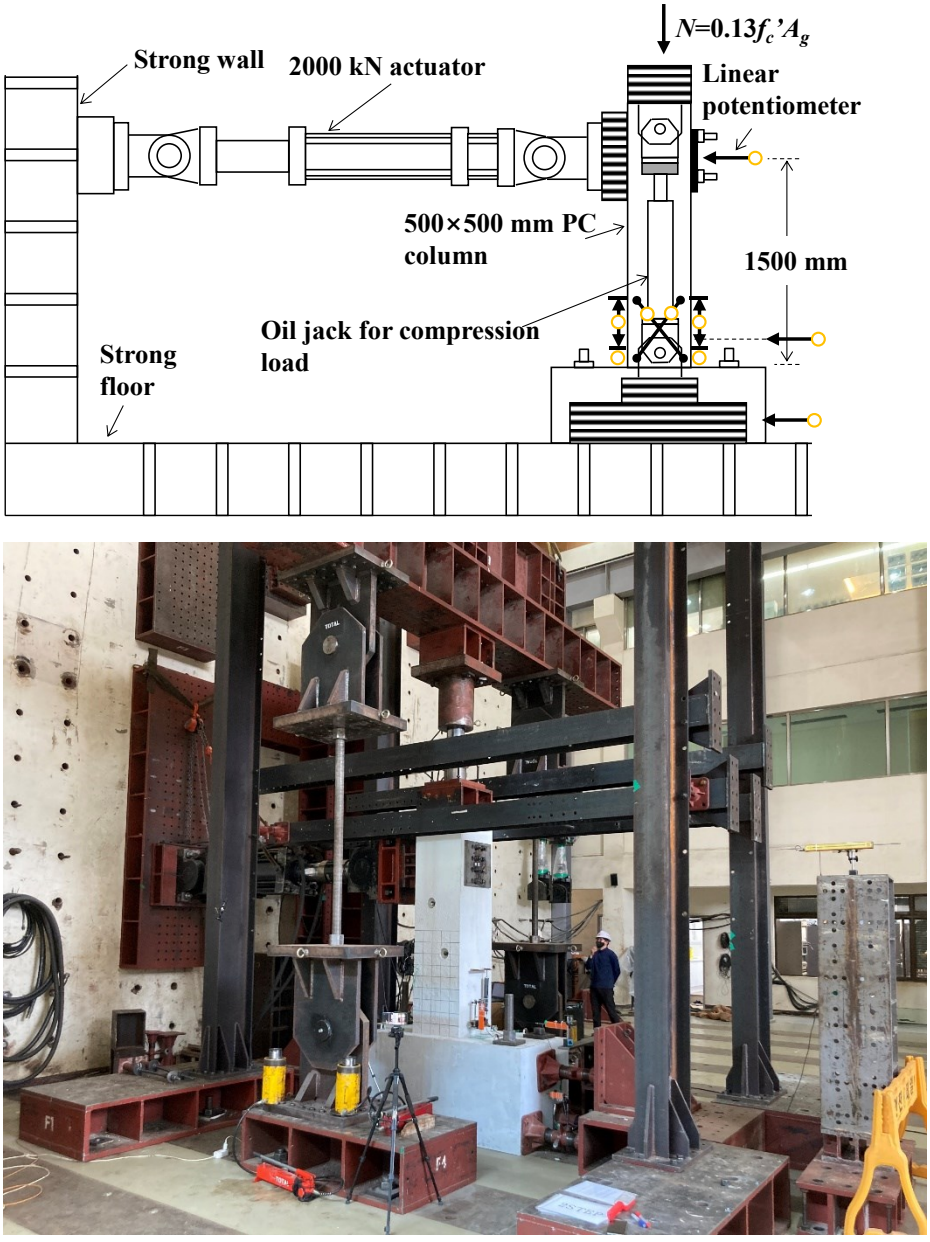

Figure 4-9 Test setup of column tests

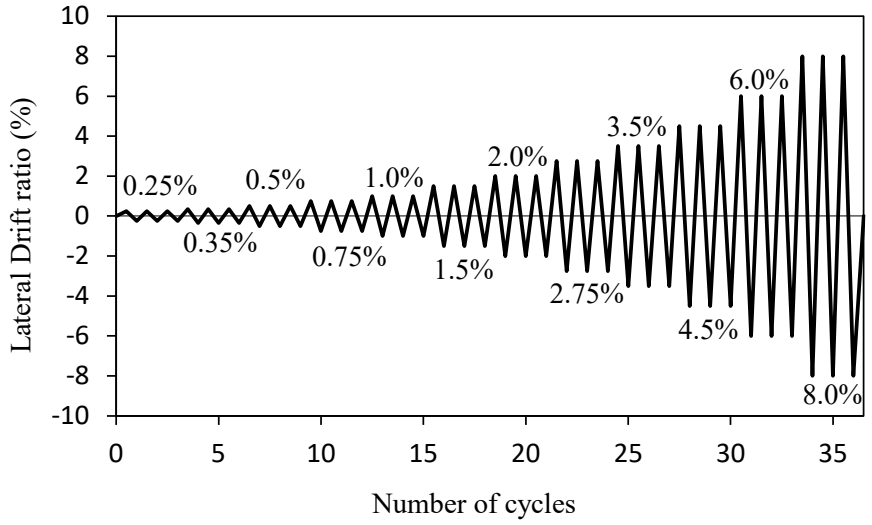

Figure 4-10 Loading plan of column tests

Table 4-5 Loading plan of column tests

Step	Lateral drift ratio[1] (%)	Lateral drift[2] (mm)	Number of load cycles	Incremental ratio[3]
1	0.25	3.75	3	-
2	0.35	5.25	3	1.40
3	0.5	7.5	3	1.42
4	0.75	11.25	3	1.50
5	1.0	15	3	1.33
6	1.5	22.5	3	1.50
7	2.0	30	3	1.33
8	2.75	41.25	3	1.37
9	3.5	52.5	3	1.27
10	4.5	67.5	3	1.28
11	6.0	90	3	1.33
12	8.0	120	3	1.33

1) (Lateral drift) / (Net height of a column)

2) (Displacement of an actuator) – (Base slip)

3) (Current drift) / (Previous drift)

4.2.7 Measurement plan

To measure deformations of reinforcements near the sleeve zone, strain gauges were attached to 8 spots on steel cages. On the longitudinal reinforcements, strain gauges were attached on 20-30 mm above and beneath splice sleeves to investigate deformation near splice sleeves. Strains of longitudinal reinforcements of the base was also measured at 20-30 mm beneath the connection face to investigate transmission of stress from column to base. On the transverse reinforcements, strain gauges were attached on the first and second column hoop from the connection face to investigate amount of stress in shear reinforcements confining splice sleeves. In the monolithic specimen, strain gauges were located at the same spot as the PC specimens.

To measure deformations of the test specimens, 9 linear variable displacement transducers (LVDT) were installed on the specimens. Actuator displacement, base slip, and column slip were measured by laterally-installed LVDTs, flexural deformation and gap opening by LVDTs on both sides, and finally, shear deformation by X-shaped LVDTs on the front.

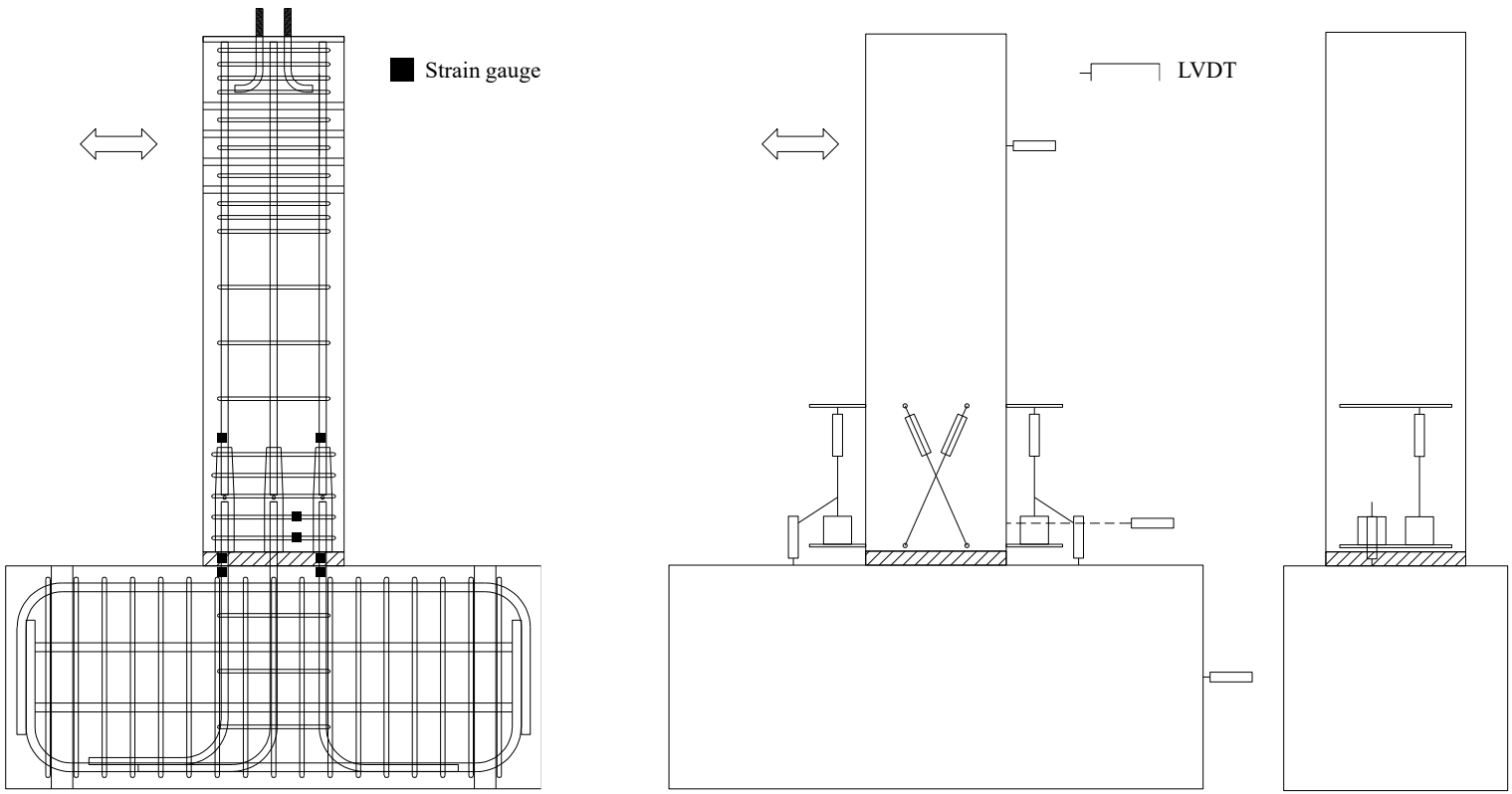

(a) Strain gauge plan (b) LVDT plan

Figure 4-11 Measurement plan of column specimens

4.2.8 Prediction of possible failure mode and estimation of nominal strength

All test specimens were design to fail in flexural failure mode. The test specimens were reinforced enough to avoid shear failure. Nominal moment capacities of the columns were calculated by P-M interaction curve considering design compression. Nominal lateral force capacities were calculated from the nominal moment capacities. All material strengths followed the material test results.

Table 4-6 Strength prediction of column specimens

Specimen	Concrete strength f_c' (MPa)	Rebar strength f_y (MPa)	Reinforcement ratio ρ (%)	Axial compression ratio[1)]	Nominal strength M_n[2)] (kN-m)	Nominal strength P_n[3)] (kN)	Shear strength V_n[4)] (kN)	Design failure mode
C-N1	59.5	666.1	1.62		802	535	1,056	
C-N2	59.5	666.1	1.62		802	535	1,056	
C-G1	69.4	646.4	1.62		849	566	1,077	
C-G2	60.4	636.0	2.54	13%	988	659	1,073	Flexure
C-G3	70.5	646.4	1.62		855	570	1,078	
C-G1-IMP	63.5	666.1	1.62		826	550	1,080	
C-G4-IMP	60.4	666.1	1.62		807	538	1,561	

1) $N/[0.85f_c'(A_g-A_{st})+f_yA_{st})]$
2) nominal moment capacity under the compression
3) nominal lateral force capacity when nominal moment capacity develops
4) nominal shear capacity under the compression (refer to **2.1 (g)**)

4.3 Test Results and Observations

4.3.1 Load-displacement relationship

Figure 4-12 shows relationships between lateral load (P) and lateral drift ratio (δ) of column specimens with either the geopolymer concrete or the normal concrete. Lateral drift ratio was calculated by dividing lateral drift with loading height (a). Lateral drift was calculated by deducting effect of slip at a base. Test strength (P_u) is presented by a round mark, and predicted strength (P_n) is presented by a horizontal dashed line. The predicted strength (P_n) is calculated in **4.2.8**. Column moment is a bending moment at the bottom face of a column, which is calculated by $M = P \times a$.

All specimens showed higher test strengths than the predicted strengths except negative loading of C-G1. The geopolymer concrete PC specimens (C-G1, C-G3) showed equivalent load-displacement relationships to the normal concrete PC specimen (C-N2) as reported in the previous cyclic loading tests of geopolymer beam-column connections (Raj et al., 2016).

The normal concrete monolithic specimen (C-N1) failed in lower drift ratio than the PC specimens due to the sparse spacing of column transverse reinforcements. The PC column with sleeve connections (C-N2) showed superior seismic performance to the monolithic column (C-N1) due to use of close spacing of column transverse reinforcements and high-strength PC materials (splice sleeve and grout). It was reported that the use of high-strength PC material can improve seismic performance and even move plastic hinge region (Lu at el., 2017).

Some PC specimens (C-G1-IMP, C-G4-IMP) failed earlier than the others because of grouting defects in splice sleeves, which was not related to concrete types. The PC specimens with grouted splice sleeve connections (C-N2, C-G1, C-G3, C-G1-IMP, C-G4-IMP) showed the pinching effect in the hysteresis curve. The splice sleeve connections lost bond capacity due to crushing of grouting inside the splice sleeves after peak loads, so that load-carrying capacity and steel strains decreased. The PC specimen with higher reinforcement ratio (C-G2) showed desirable hysteresis curve and showed no pinching effect.

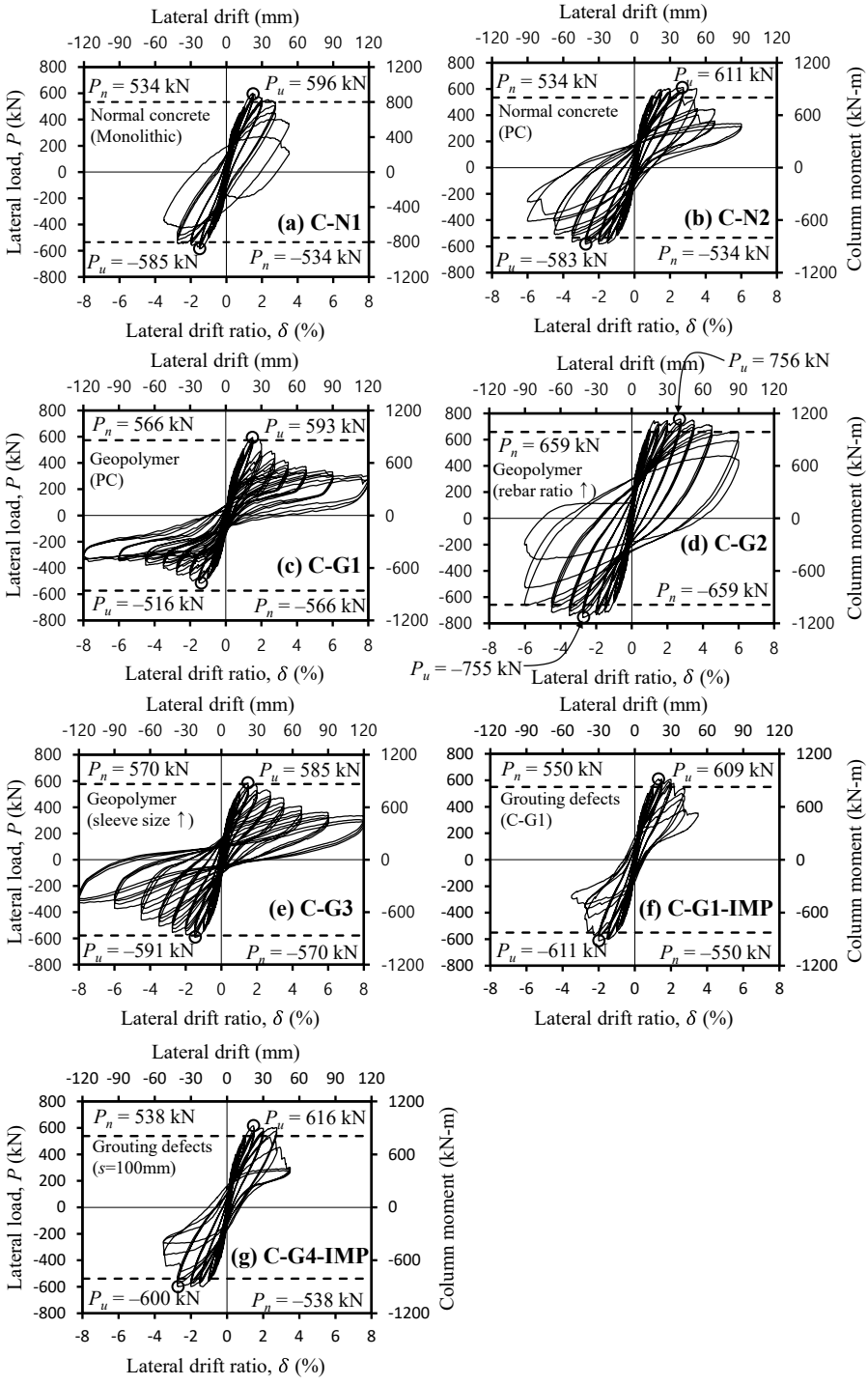

Figure 4-12 Load-displacement relationship of column specimens

Specimen C-N1 is the monolithic specimen with the normal concrete. C-N1 used eight D25 as column longitudinal reinforcements and D10@200 mm as column transverse reinforcements. The test strength was +596 kN (δ = 1.5%) and –585 kN (δ = 1.5%), and this was respectively 13% and 11% higher than the predicted strength, 529 kN. After the peak load, the strength was degraded as concrete cover of a compressive side started to be spalled at 2.0% drift ratio. At the first cycle of 3.5% drift ratio, the test ended due to severe strength degradation as shear cracking developed and shear failure and buckling of a compressive longitudinal reinforcement occurred. This is because the spacing of the column transverse reinforcements was sparse ($s \fallingdotseq d/2$).

Specimen C-N2 is the PC specimen with the geopolymer concrete. C-N2 used the same reinforcement detail as that of C-N1 and used D25 splice sleeves. The test strength was +611 kN (δ = 2.75%) and –583 kN (δ = 2.75%), and this was respectively 15% and 10% higher than the predicted strength, 531 kN. After the peak load, at the third load cycle of 2.75% drift ratio, the strength was degraded as concrete cover of a tensile side in the sleeve zone was spalled with sound of rupture. The test ended at 6.0% drift ratio. The pinching effect was observed.

Specimen C-G1 is the PC specimen with the geopolymer concrete. C-G1 used the same reinforcement detail as that of C-N2. The test strength was +593 kN (δ = 1.5%) and –516 kN (δ = 1.5%). In the positive loading, the test strength was 5% higher than the predicted strength, 566 kN. In the negative loading, the test strength was 9% lower than the predicted strength, 566 kN. The reason may be grouting defects inside the splice sleeves. The grouting defects can be detected by the pinching effect of the hysteresis curve; convex curve in the

unloading phase of the negative loading (Xie et al., 2022). After the peak load, the strength was degraded as the corner concrete was crushed. The test ended at 8.0% drift ratio.

Specimen C-G2 increased reinforcement ratio from ρ = 1.62% to ρ = 2.54% based on C-G1. The test strength was +756 kN (δ = 2.75%) and –755 kN (δ = 2.75%), and this is 15% higher than the predicted strength, 659 kN. At the first load cycle of 4.5% drift ratio, a concrete cover of a tensile side in the sleeve zone was spalled with sound of rupture Unlike C-N2 and C-G1, the strength degradation was limited until 6.0% drift ratio. The test ended at 6.0% drift ratio as shear failure occurred in the lower part of the column. Since high reinforcement ratio caused high moment capacity and high shear force, the column failed in shear failure after flexural yielding. Unlike C-N2 and C-G1 which used D25 rebars and D25 splice sleeves, the pinching effect was not observed.

Specimen C-G3 changed the size of splice sleeves from D25 to D29 based on C-G1. The test strength was +585 kN (δ = 1.5%) and –591 kN (δ = 2.75%), and this is 3-4% higher than the predicted strength, 570 kN. At the peak load, concrete cover of a compressive side started to be spalled. At 2.0% drift ratio, the strength was degraded as concrete cover of a tensile side in the sleeve zone was spalled. The test ended at 8.0% drift ratio as the strength gradually decreased. Unlike C-N2 and C-G1 which used D25 rebars and D25 splice sleeves, the pinching effect was not observed.

Specimen C-G1-IMP was a specimen with the same details as C-G1. The test strength was +609 kN (δ = 1.5%) and –611 kN (δ = 2.0%), and this is 12%

higher than the predicted strength, 543 kN. The grouting defects can be detected by the pinching effect of the hysteresis curve; curvature in the unloading. At the first load cycle of 2.75% drift ratio, the strength was degraded as concrete cover of a tensile side in the sleeve zone was spalled. In following load cycles, the strength kept being degraded. The test ended at 3.5% drift ratio, earlier than C-N2 or C-G3 due to grouting defects.

Specimen C-G4-IMP changed spacing of transverse reinforcements from 200 mm to 100 mm in the column out of the sleeve zone. The test strength was +616 kN (δ = 1.5%) and –600 kN (δ = 2.75%), and this is 12-14% higher than the predicted strength, 538 kN. At the first load cycle of 2.0% drift ratio, concrete cover of a compressive side started to be spalled. Like C-G1-IMP, the grouting defects can be detected by the pinching effect of the hysteresis curve; curvature in the unloading phase. At the first cycle of 3.5% drift ratio, the strength was degraded as concrete cover of a tensile side in the sleeve zone was spalled. After then, at the first and second load cycles of 3.5% drift ratio, the strength kept degraded as concrete cover of a tensile side in the sleeve zone was spalled. The test ended at 3.5% drift ratio, which was earlier than C-N2 or C-G3 due to grouting defects.

4.3.2 Failure mode

As shown in **Figure 4-13**, the failure modes of the geopolymer concrete PC specimens were similar to that of the normal concrete PC specimen (C-N2). The monolithic specimen (C-N1) failed in shear failure after flexural yielding after concrete crushing of a compressive side. This is thought to be caused by

sparse spacing of transverse reinforcements of ordinary moment frames ($s \fallingdotseq d/2$).

The PC specimens with splice sleeves (C-N2, C-G1, C-G2, C-G3, C-G1-IMP, C-G4-IMP) suffered damage mainly around the grouting gap and the splice sleeves, which disagrees with the existing test results where damage occurred above the splice sleeves (Lu at el., 2017). The reason behind the disagreement may be related to low relative strength of grout to concrete; 20-25% higher in this study whereas 144% higher in Lu at el. (2017). If extremely high relative strength of grout is used, plastic hinge zone may move above the splice sleeve zone, resulting splice sleeve connection to be a strong connection.

The PC specimens with D25 rebars (C-N2, C-G3, C-G1-IMP, C-G4-IMP) failed in flexural failure after concrete crushing of a compressive side and concrete spalling of corners of a tensile side. C-G1 failed in sleeve rupture and grout crushing after flexural yielding, experiencing the same procedure as that of the other PC specimens. This happened due to grouting defects. The PC specimen with high reinforcement ratio (C-G2) failed in shear failure after flexural yielding after the same procedure as that of the other PC specimens. This happened because higher reinforcement ratio allowed the specimen to go through large deformation.

The grouted splice sleeve connections in PC specimens lost bond capacity due to crushing of grouting inside the splice sleeves after peak loads, so that load-carrying capacity and steel strains decreased. In other words, the difference in ductility and energy dissipation of the test specimens was affected by the time of crushing of grouting inside sleeves and spalling of concrete cover.

(a) C-N1 (b) C-N2 (c) C-G1 (d) C-G2

(e) C-G3 (f) C-G1-IMP (g) C-G4-IMP

Figure 4-13 Final failure pictures of column specimens

In C-N1 (normal concrete, monolithic), at 2.0% drift ratio, cracking of concrete cover started (**Figure 4-14 (a)**), and at 2.75% drift ratio, concrete was crushed and concrete cover was spalled in a compressive side (**Figure 4-14 (b)**). At 3.5% drift ratio, shear failure and buckling of the column longitudinal reinforcement occurred in the lower part of the column due to sparse spacing of column transverse reinforcements of an ordinary moment frame ($s \fallingdotseq d/2$) (**Figure 4-14 (c)**). Finally, at 3.5% drift ratio, the specimen failed as shown in **Figure 4-14 (e)**. After ending of the test, concrete cover was removed as shown in **Figure 4-14 (d)**.

In C-N2 (normal concrete, PC), at 1.5% drift ratio, vertical cracking occurred in concrete cover (**Figure 4-15 (a)**). At 2.0% drift ratio, cover of non-shrinkage grout started to be delaminated (**Figure 4-15 (b)**). At 2.75% drift ratio, concrete cover of a tensile side in the sleeve zone was spalled (**Figure 4-15 (c)**). Finally, at 6.0% drift ratio, the specimen failed as shown in **Figure 4-15 (e)**. Column transverse reinforcements were not unfastened as shown in the picture taken after removing concrete cover after ending of the test (**Figure 4-15 (d)**).

In C-G1 (geopolymer concrete, PC) the failure mode was similar to that of C-N2 except the failure occurred at a sleeve and grout. At 1.5% drift ratio, cover of non-shrinkage grout was delaminated (**Figure 4-16 (a)**), which was followed by vertical cracking in concrete cover (**Figure 4-16 (b)**). At the first load cycle of 2.75% drift ratio, concrete cover of a tensile side in the sleeve zone was spalled (**Figure 4-16 (c)**). At 8.0% drift ratio, a sleeve was ruptured and grout was crushed (**Figure 4-16 (d)**). Column transverse reinforcements were not unfastened as shown in the picture taken after removing concrete cover after ending of the test (**Figure 4-16 (e)**). The failure of non-shrinkage grout inside the sleeve was observed (**Figure 4-16 (f)**).

In C-G2 which used D32 as column longitudinal reinforcements, at 1.5% drift ratio, cover of non-shrinkage grout was delaminated (**Figure 4-17 (a)**), which was followed by vertical cracking in concrete cover (**Figure 4-17 (b)**). Unlike C-G1 which used D25 as column longitudinal reinforcements, spalling of concrete cover was delayed, which occurred at 4.5% drift ratio at first (**Figure (c)**). Finally, at 6.0% drift ratio, the specimen failed in shear failure after flexural yielding (**Figure 4-17 (e)**). This caused column transverse reinforcements to be unfastened as shown in the picture taken after removing

concrete cover after ending of the test (**Figure 4-17 (d)**).

In C-G3 which used D29 sleeve, at 1.5% drift ratio, cover of non-shrinkage grout was delaminated (**Figure 4-18 (a)**), which was followed by vertical cracking in concrete cover (**Figure 4-18 (b)**). At the first load cycle of 3.5% drift ratio, concrete cover of a tensile side in the sleeve zone was spalled (**Figure 4-18 (c)**). Finally, at 8.0% drift ratio, the specimen failed in flexural failure (**Figure 4-18 (e)**). Column transverse reinforcements were not unfastened as shown in the picture taken after removing concrete cover after ending of the test (**Figure 4-18 (d)**).

In C-G1-IMP which is the same specimen as C-G1, at 1.5% drift ratio, cover of non-shrinkage grout was delaminated (**Figure 4-19 (a)**), which was followed by vertical cracking in concrete cover (**Figure 4-19 (b)**). At the first cycle of 2.75% drift ratio, concrete cover of a tensile side in the sleeve zone was spalled (**Figure 4-19 (c)**). Finally, at 3.5% drift ratio, the specimen failed in sleeve failure (**Figure 4-19 (e)**). Column transverse reinforcements were not unfastened as shown in the picture taken after removing concrete cover after ending of the test (**Figure 4-19 (d)**).

In C-G4-IMP which used closer spacing of transverse reinforcements, at 1.5% drift ratio, cover of non-shrinkage grout was delaminated (**Figure 4-20 (a)**), which was followed by vertical cracking in concrete cover (**Figure 4-20 (b)**). At the first cycle of 3.5% drift ratio, concrete cover of a tensile side in the sleeve zone was spalled (**Figure 4-20 (c)**). Finally, at 3.5% drift ratio, the specimen failed in flexural failure (**Figure 4-20 (e)**). Column transverse reinforcements were not unfastened as shown in the picture taken after removing concrete

cover after ending of the test (**Figure 4-20 (d)**).

(a) Concrete cover cracking (δ = 2.0%)

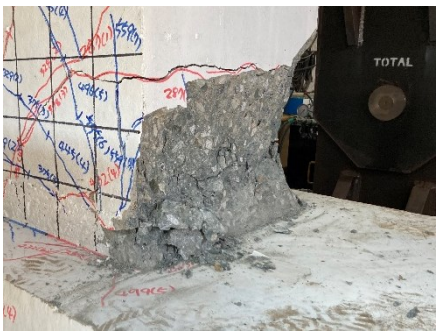

(b) Concrete cover spalling of a compressive side (δ = 2.75%)

(c) Shear cracking & rebar buckling (δ = 3.5%)

(d) Concrete cover removal after test

(e) Final failure (front) (δ = 3.5%)

Figure 4-14 C-N1 detailed failure pictures

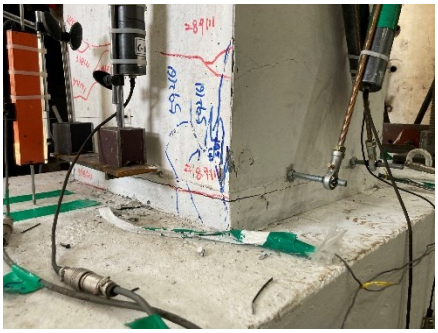

(a) Concrete cover cracking (δ = 2.0%)

(b) Grout cover delamination (δ = 2.0%)

(c) Sleeve cover spalling of a tensile side (δ = 2.75%)

(d) Concrete cover removal after test

(e) Final failure (front) (δ = 6.0%)

Figure 4-15 C-N2 detailed failure pictures

(a) Grout cover delamination (δ = 1.5%)

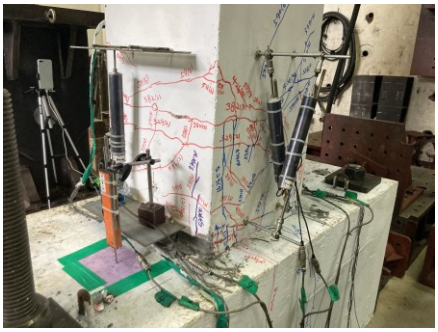

(b) Concrete cover vertical cracking

(c) Sleeve cover spalling of a tensile side (δ = 4.5%)

(d) Sleeve rupture & grout crushing δ = 8.0%)

(e) Concrete cover removal after test

(f) Grout failure inside a sleeve

Figure 4-16 C-G1 detailed failure pictures

(a) Grout cover delamination (δ = 1.5%)

(b) Concrete cover vertical cracking

(c) Sleeve cover spalling of a tensile side (δ = 4.5%)

(e) Final failure (front) (δ = 6.0%)

(e) Concrete cover removal after test

Figure 4-17 C-G2 detailed failure picture s

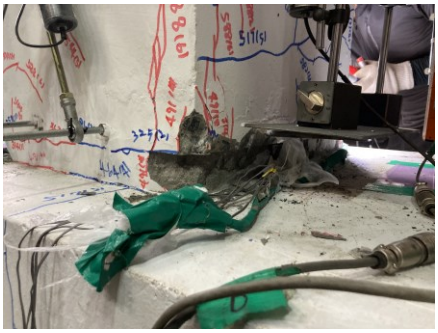

(a) Grout cover delamination (δ = 1.5%)

(b) Concrete cover vertical cracking

(c) Sleeve cover spalling of a tensile side (δ = 2.0%)

(d) Concrete cover removal after test

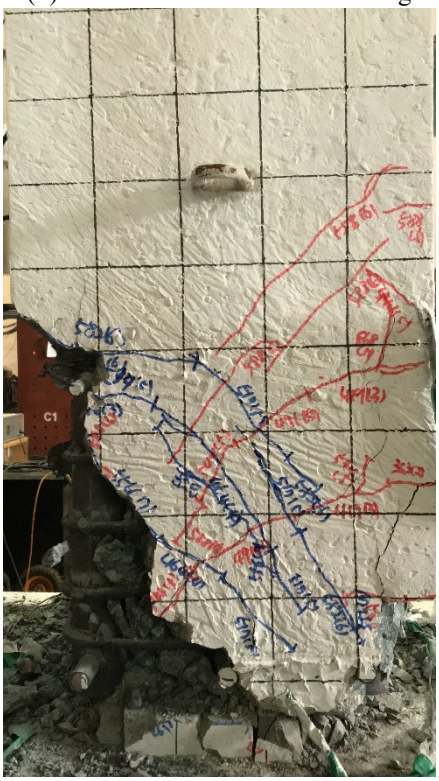

(e) Final failure (front) (δ = 8.0%)

Figure 4-18 C-G3 detailed failure pictures

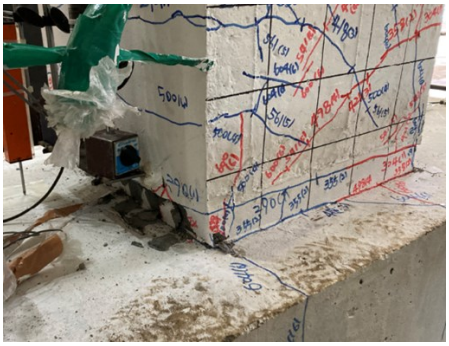

(a) Grout cover delamination (δ = 1.5%)

(b) Concrete cover vertical cracking

(c) Sleeve cover spalling of a tensile side (δ = 2.75%)

(d) Concrete cover removal after test

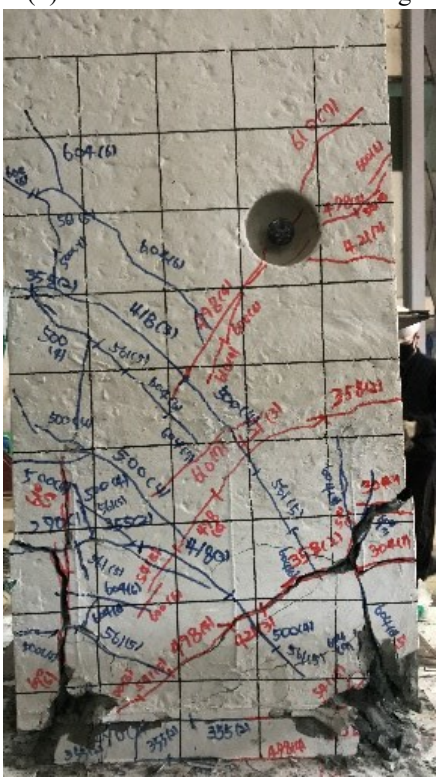

(e) Final failure (front) (δ = 3.5%)

Figure 4-19 C-G1-IMP detailed failure pictures

(a) Grout cover delamination (δ = 1.5%)

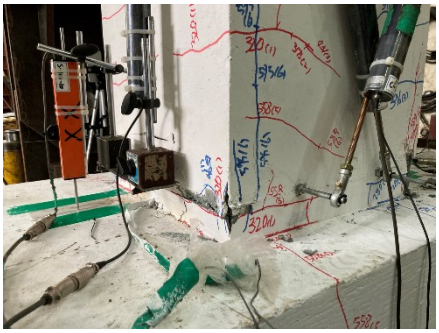

(b) Concrete cover vertical cracking

(c) Sleeve cover spalling of a tensile side (δ = 2.75%)

(d) Concrete cover removal after test

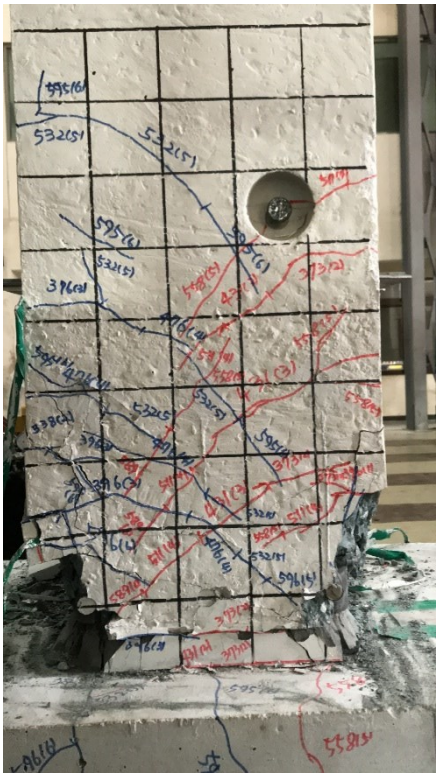

(e) Final failure (front) (δ = 3.5%)

Figure 4-20 C-G4-IMP detailed failure pictures

4.3.3 Strains of steel reinforcements

From **Figure 4-21** to **Figure 4-23** show strains of longitudinal reinforcements of the column specimens. The strain gauges of **Figure 4-21** were attached in the 50-mm grouting gap between PC columns and base. The strain gauges of **Figure 4-22** were attached just above splice sleeves (450-560 mm away from the base face). The strain gauges of **Figure 4-23** were attached to 30 mm under the face of the base. Stain gauges of the monolithic specimen were attached to the same location as that of PC specimens.

As shown in **Figure 4-21**, all steel strains in the 50-mm grouting gap were higher than the yield strains. This occurred regardless of a type of concrete and whether monolithic or PC.

As shown in **Figure 4-22** and **4-23**, the steel deformation of PC specimens except the grouting gap was mostly less than the yield strains. Gauge 6 of C-G3 showed a higher strain than the yield strain for a short time, but the strain decreased to be less than the yield strain as the lateral drift increased.

This means that, in PC specimens, the deformation of steel reinforcements was concentrated on the grouting gap between the column and the base.

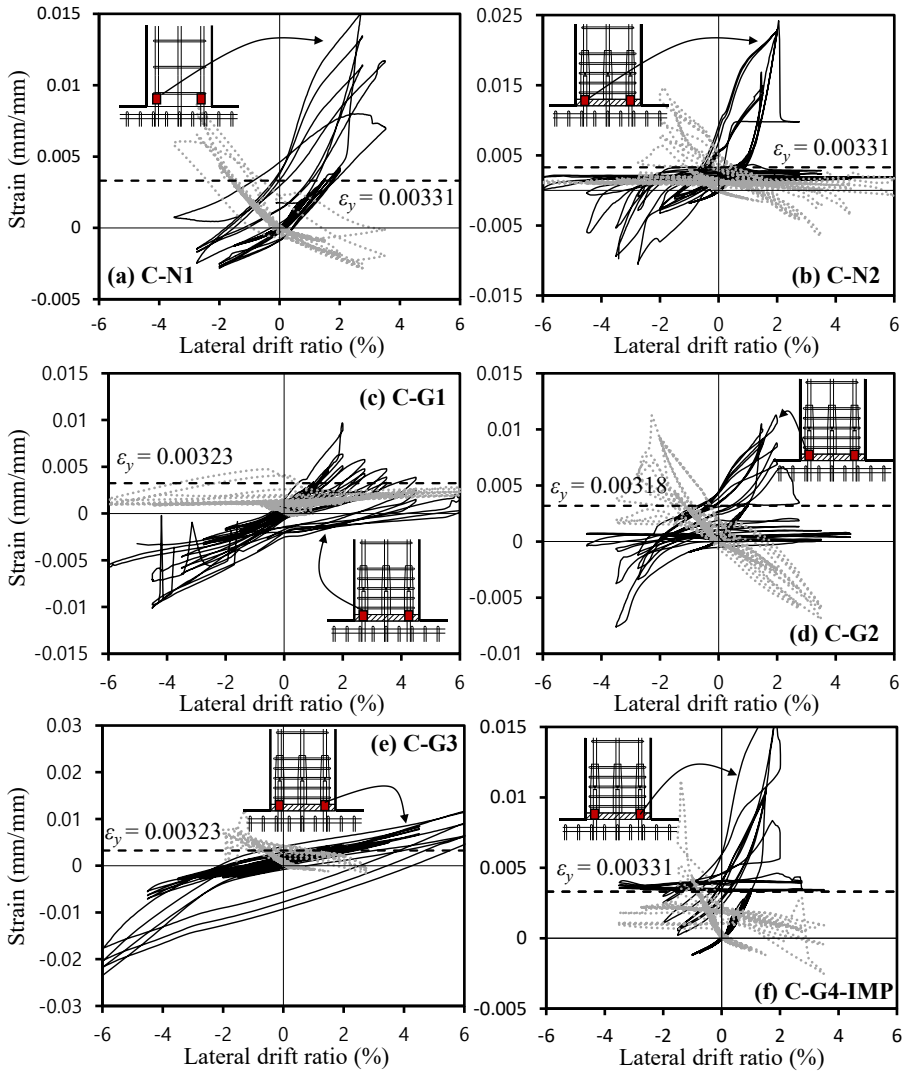

Figure 4-21 Strain of column longitudinal reinforcement in grouting gap

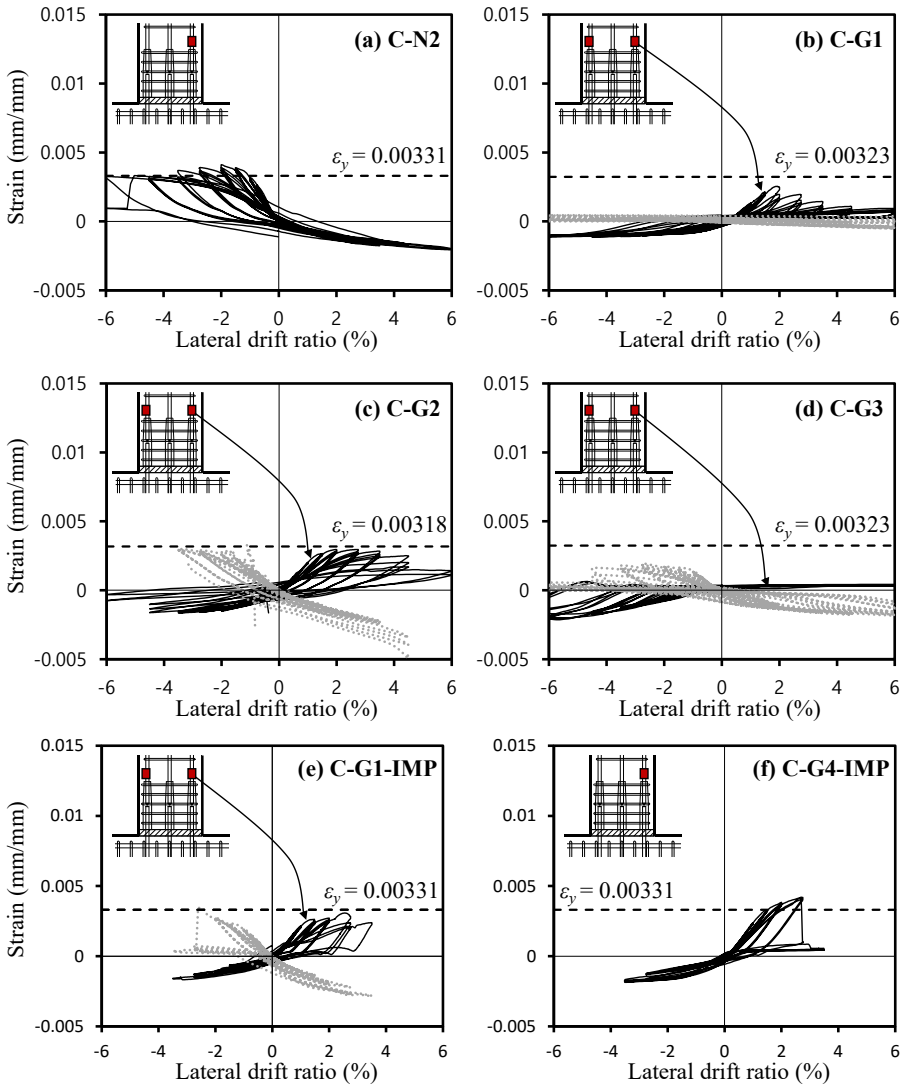

Figure 4-22 Strain of column longitudinal reinforcement above splice sleeve

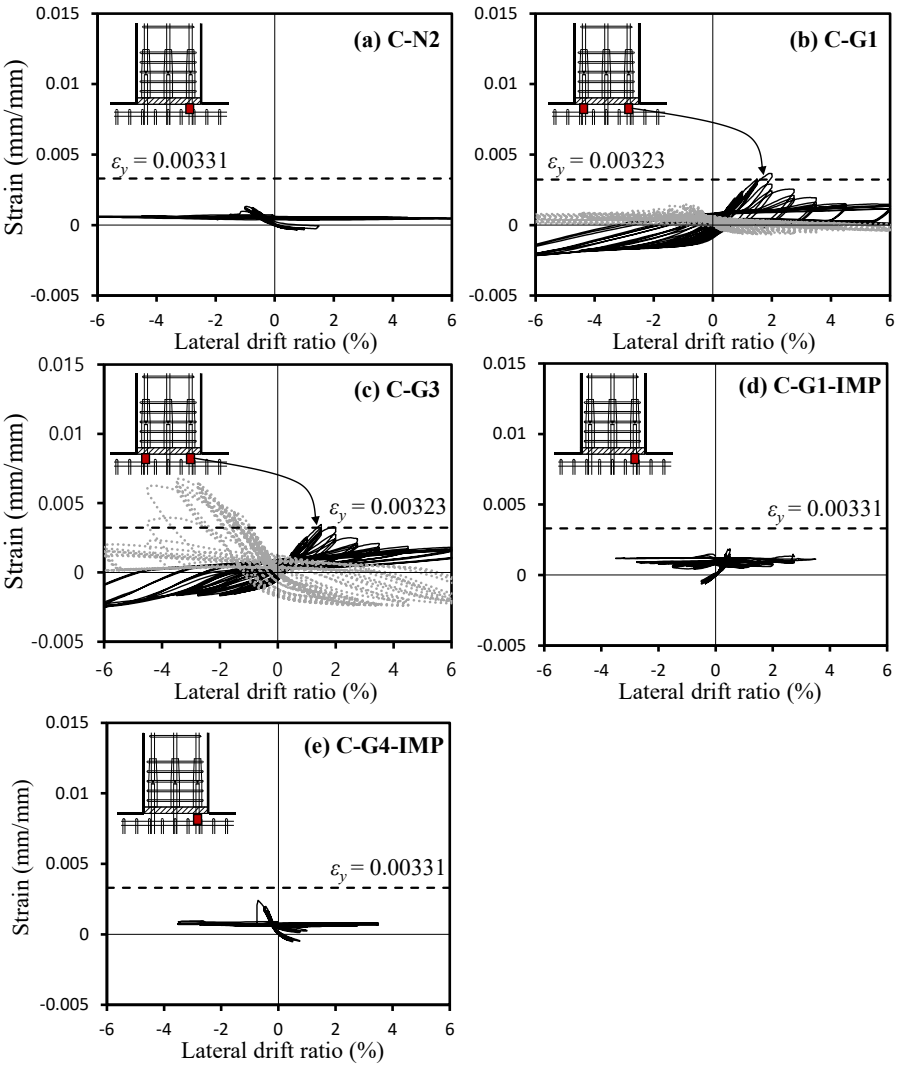

Figure 4-23 Strain of column longitudinal reinforcement under face of base

4.3.4 Secant stiffness

Figure 4-24 shows the variation of the secant stiffness of the specimens. The secant stiffness is defined by the slope between the peak load point and the origin either in positive or negative loading at each drift ratio. The secant stiffness degraded as the lateral drift increased. The stiffness degradation of all specimens except specimen C-G2 was similar regardless of concrete type or fabrication method. In the precast specimen with higher reinforcement ratio (C-G2), the stiffness was greater or degraded slower. The secant stiffness of specimen C-G2 was 23-92% higher than specimen C-G1 after 1.0% drift ratio.

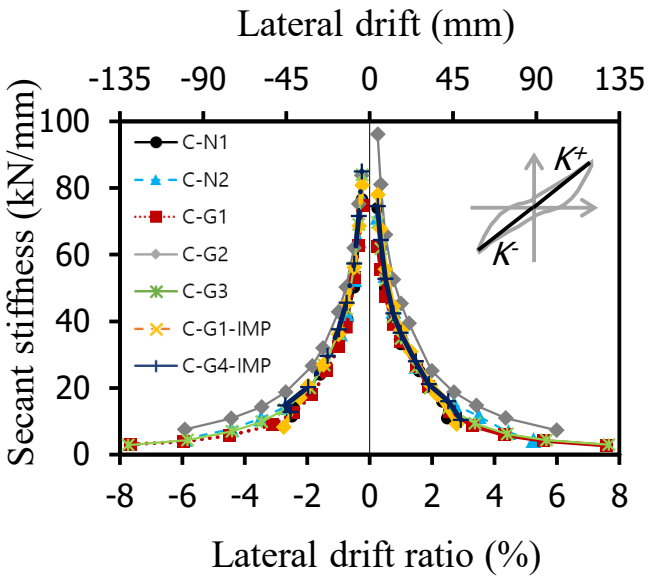

Figure 4-24 Secant stiffness of columns

4.3.5 Energy dissipation

Figure 4-25 shows cumulative energy dissipation of the column specimens according to lateral drift ratio. Energy dissipation is defined by an area of a closed loop in each drift ratio in a hysteresis curve. At 3.5% drift ratio, energy dissipation of C-G2 with high reinforcement ratio was the greatest, followed in order of C-N2, C-G3, C-G4-IMP, C-N1, C-G1, and C-G1-IMP.

Comparing the normal concrete specimens with the geopolymer concrete specimens, the monolithic specimen with normal concrete (C-N1) showed similar energy dissipation with other PC specimens, but failed early at 3.5% drift ratio. The PC specimen with the normal concrete (C-N2) showed higher energy dissipation than the PC specimen with the geopolymer concrete (C-G1, C-G1-IMP, C-G4-IMP). This occurred because of the poor injecting quality of grouting of C-G1, C-G1-IMP, C-G4-IMP. Instead, C-G3 which used one-size larger sleeves showed almost the same energy dissipation as that of C-N2.

Comparing between the geopolymer concrete specimens, energy dissipation of C-G2 with high reinforcement ratio was the highest. Energy dissipation of C-G3 with larger sleeves was 26-40% higher than that of C-G1 after 3.5% drift ratio. The specimens with grouting defects (C-G1-IMP, C-G4-IMP) showed similar energy dissipation but failed early at 3.5% drift ratio. This implies that grouting defects harm energy dissipation capacity and using one-size large sleeves can prevent it.

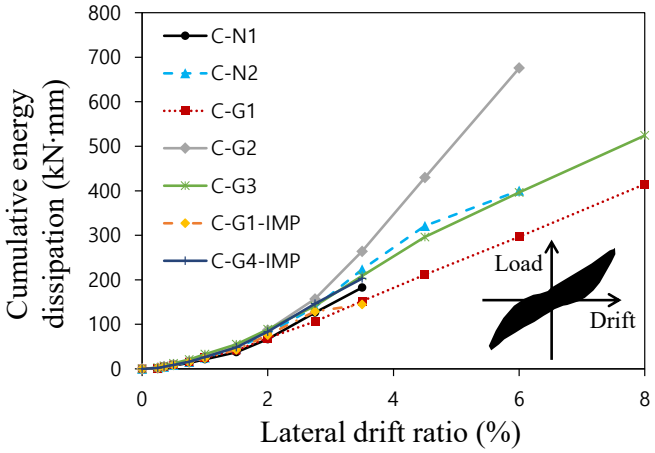

Figure 4-25 Cumulative energy dissipation of column specimens

Figure 4-26 shows energy dissipation per load cycle of the column specimens according to lateral drift ratio. the monolithic specimen (C-N1) and the PC specimen with grouting defects (C-G1-IMP, C-G4-IMP) failed early at 3.5% drift ratio. In PC specimens, energy dissipation of the second load cycle was similar with that of the first load cycle, which was 73-102% of the first load cycle. Energy dissipation of the third cycle decreased than that of the second cycle but showed a similar pattern.

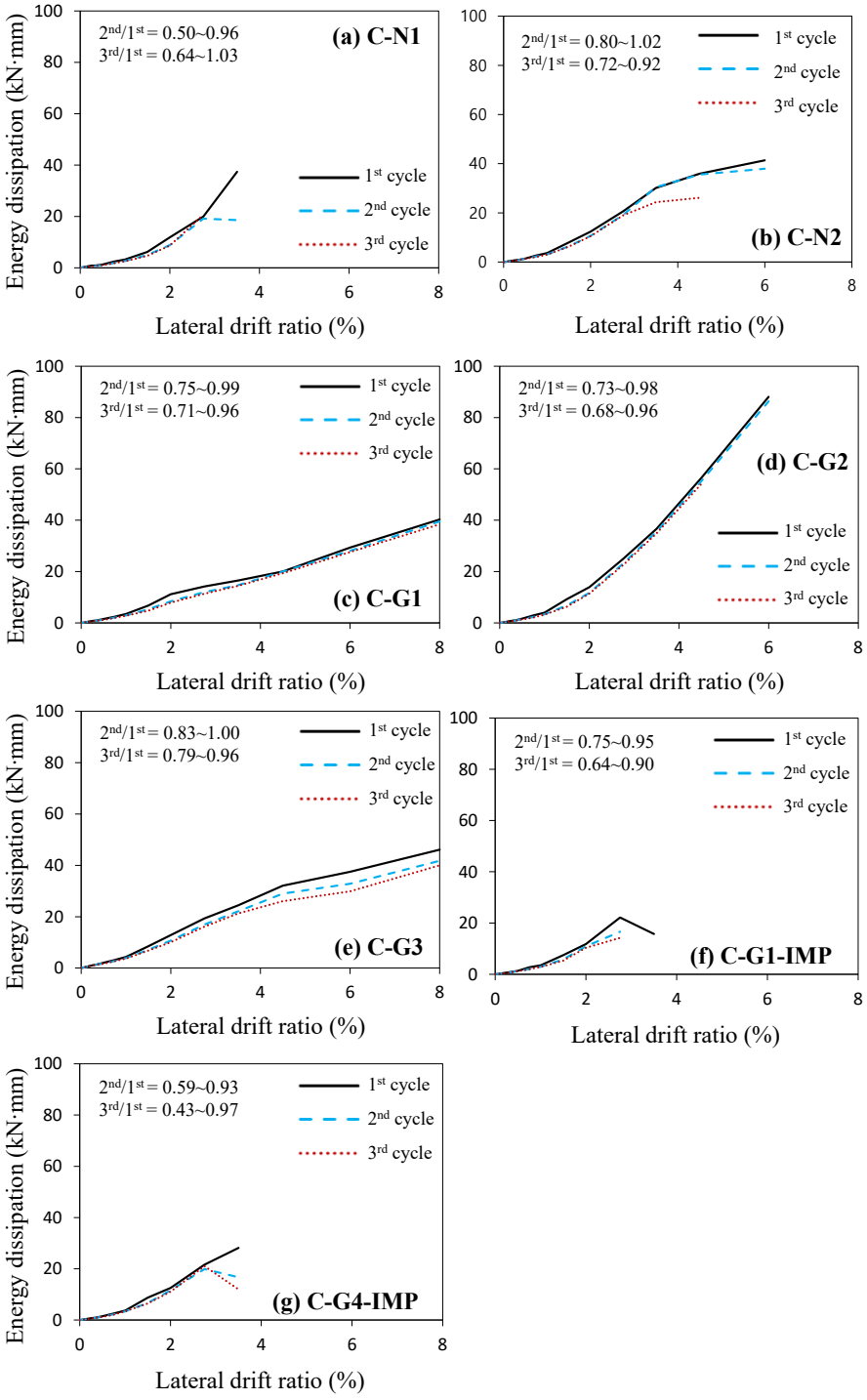

Figure 4-26 Energy dissipation per load cycle of column specimens

4.3.6 Deformation capacity

Deformation capacity was calculated using a method illustrated in **Figure 4-27 (b)** based on the envelop curve shown in **Figure 4-27 (a)**. The envelop curve was drawn by connecting maximum load points at each drift ratio. The deformation capacity was characterized by yield strength, yield stiffness, maximum strength, yield displacement, yield drift ratio, ultimate displacement, ultimate drift ratio, and ductility. Yield displacement was defined by the drift ratio at the peak load of a straight line passing the origin and the point of 75% of peak load. Ultimate displacement was defined by the drift ratio at the point of 85% of peak load after the peak load. Yield stiffness was defined by a value dividing the peak load with yield displacement.

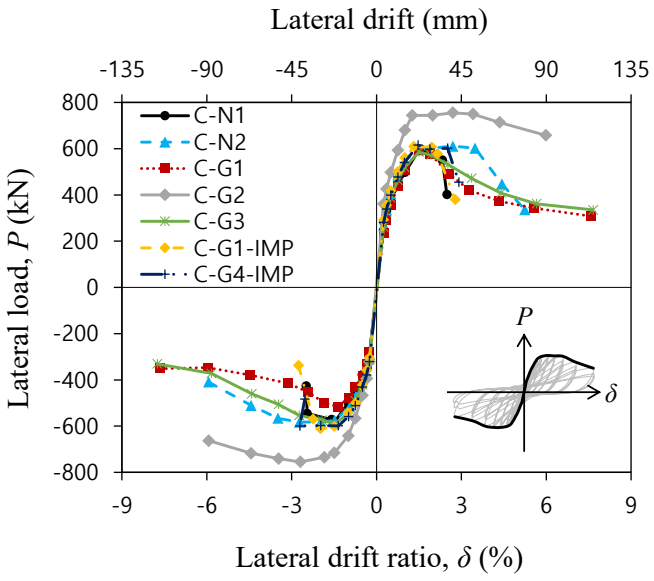

(a) Envelop curve

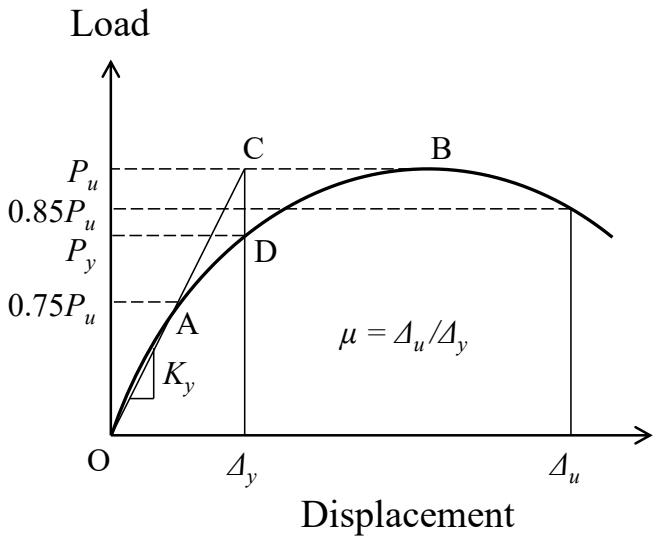

(b) Definition of deformation capacity

Figure 4-27 Envelop curve and definition of deformation capacity of column specimens

As shown in **Table 4-7**, the yield stiffnesses and the yield displacements of the test specimens were similar. However, the ultimate displacements of the PC specimens were higher than that of C-N1 except C-G1-IMP; 79%, 6%, 146%, 35%, and 9% higher in order of C-N2, C-G1, C-G2, C-G3, and C-G4-IMP. Therefore, the ductility of the PC specimens was higher than that of C-N1;105%, 32%, 156%, 64%, 18%, and 31% higher in order of C-N2, C-G1, C-G2, and C-G3, C-G1-IMP, and C-G4-IMP.

When comparing C-G1 (positive loading) and C-G3 to C-N2 (**Figure 4-28**), the ductility of C-G1 (positive loading) C-G3 was respectively 35% and 20% lower than that of C-N2 (normal concrete) in average, as reported in the previous cyclic loading tests of beam-column connections (Ngo et al., 2021). When comparing C-G1, C-G3, C-G1-IMP, and C-G4-IMP, ductility of C-G3

(larger sleeve) was higher than the specimens with grouting defects; 24%, 39% and 25% in order of C-G3, C-G1-IMP, and C-G4-IMP).

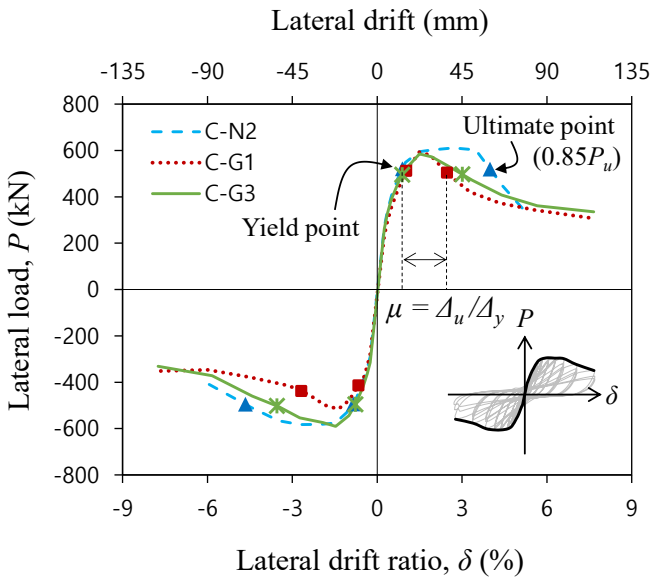

Figure 4-28 Comparison of deformation capacities between specimens C-N2, C-G1 and C-G3

Table 4-7 Deformation capacity of column specimens

	Yield strength P_y (kN)		Yield stiffness K_y (kN/mm)		Peak strength P_u (kN)		Yield drift ratio δ_y (%)		Ultimate drift ratio δ_u (%)		Ductility μ	
Specimen	Pos.	Neg.	Pos.	Neg.	Pos.	Neg.	Pos.	Neg.	Pos.	Neg.	Pos.	Neg.
C-N1	500	-494	39.1	40.0	596	-585	1.01	-0.97	2.37	-2.47	2.34	2.53
C-N2	520	-494	46.0	46.0	611	-583	0.89	-0.85	3.99	-4.66	4.50	5.51
C-G1	512	-415	38.3	52.0	593	-516	1.03	-0.66	2.47	-2.69	2.40	4.05
C-G2	649	-642	55.2	50.2	756	-755	0.91	-1.00	5.99	-5.93	6.56	5.92
C-G3	495	-496	44.0	50.9	585	-591	0.89	-0.77	3.01	-3.55	3.39	4.59
C-G1-IMP	519	-512	49.3	49.9	609	-612	0.82	-0.82	2.35	-2.35	2.84	2.88
C-G4-IMP	527	-510	43.8	53.7	616	-600	0.94	-0.74	2.73	-2.57	2.91	3.46

4.3.7 Seismic performance evaluation by ACI 374.1-05

ACI 374-05 specifies acceptance criteria for evaluating seismic performance of reinforced concrete moment frames by experiments. If all the acceptance criteria are satisfied, the test specimen is considered to have equivalent seismic performance to special moment frames according to ACI 318-19 (**refer to 2.1 (m)**).

As shown in **Table 4-8**, C-N1 and C-G1-IMP were unable to evaluate their seismic performance because it failed before the third load cycle of 3.5% drift ratio. Criterion (a) is excluded in this study because the allowable story drift in criterion (a) differs according to required ductility when designing structure. And also, criterion (b) is excluded because that criterion is for beam-column connection tests.

The test specimens except C-N1 and C-G1-IMP satisfied criterion (d) and (e) regardless of the type of concrete. In case of C-G2 with high reinforcement ratio satisfied all criteria including (c).

Table 4-8 Seismic performance evaluation by ACI 374.1-05

Criterion		C-N1		C-N2		C-G1		C-G2		C-G3		C-G1-IMP		C-G4-IMP	
		Pos.	Neg.	Pos.	Neg.	Pos.	Neg.	Pos.	Neg.	Pos.	Neg.	Pos.	Neg.	Pos.	Neg
(c) Lateral force at 3.5% (kN)	$0.75E_{max}$	447	-439	458	-437	444	-387	567	-566	439	-443	457	-459	462	-450
	E at 3.5%	-	-	441	-498	363	-363	695	-686	402	-445	-	-	455	-484
	Judgement	-	-	NG	OK	NG	NG	OK	OK	NG	OK	-	-	NG	OK
(d) Energy dissipation (kN-m)	Elastic plastic	-		86.8		68.4		124.0		79.4		-		87.5	
	Actual	-		24.4		14.5		34.8		21.2		-		12.0	
	Ratio	-		0.281		0.211		0.281		0.267		-		0.137	
	Judgement	-		OK		OK		OK		OK		-		OK	
(e) Stiffness (kN/mm)	5% of initial *K*	3.70	3.82	3.57	3.83	3.07	3.73	4.81	4.28	3.42	4.20	3.90	4.04	3.73	4.25
	K at 3.5%	-	-	10.5	16.3	4.2	14.8	14.3	5.4	10.1	14.1	-	-	8.1	8.2
	Judgement	-	-	OK	OK	OK	OK	OK	OK	OK	OK	-	-	OK	OK

4.3.8 Seismic performance evaluation by AIJ 2002 Guidelines

AIJ 2002 Guidelines specifies structural performance goals so that PC structure can ensure the performance of RC structure. If PC members on ultimate limit state under earthquake load satisfy all the acceptance criteria, PC members can ensure the equivalent performance to RC members (**refer to 2.1 (n)**). As shown in **Table 4-9**, criterion (c) and (e) are excluded because they are applied to PC beam-column joints.

The PC geopolymer concrete column specimens (positive loading of C-G1, C-G2, C-G3) satisfied the acceptance criteria compared with the monolithic normal concrete specimen (C-N1) in overall except the specimens with grouting defects (negative loading of C-G1, C-G1-IMP, C-G4-IMP). The yield strengths and the peak strengths of the PC geopolymer specimens were 99-130% and 79-103% of the normal monolithic specimen, respectively. The yield drift ratios of the PC geopolymer concrete specimens were 79-103% of the monolithic normal concrete specimen, which were more than 80% of the monolithic specimen in overall as AIJ 2002 Guideline suggests.

When comparing the PC geopolymer concrete specimens (C-G1, C-G3) with the PC normal concrete specimen (C-N2), the PC geopolymer concrete specimens showed similar seismic performance with the PC normal concrete specimen. The yield strengths and the peak strengths of the PC geopolymer concrete specimens were 95-100% and 96-101% of the PC normal concrete specimen, respectively. The yield drift ratios of the PC geopolymer concrete specimens were 91-116% of the PC normal concrete specimen.

Table 4-9 Seismic performance evaluation by AIJ 2002 Guidelines

Criterion		C-N1		C-N2		C-G1		C-G2		C-G3		C-G1-IMP		C-G4-IMP	
		Pos.	Neg.	Pos.	Neg.	Pos.	Neg.	Pos.	Neg.	Pos.	Neg.	Pos.	Neg.	Pos.	Neg.
(a) Yield strength	P_y (kN)	500	-494	520	-494	512	-415	649	-642	495	-496	519	-512	527	-510
	/C-N1	-	-	1.04	1.00	1.02	0.84	1.30	1.30	0.99	1.00	1.04	1.04	1.05	1.03
	/C-N2	-	-	-	-	0.98	0.84	1.25	1.30	0.95	1.00	1.00	1.04	1.01	1.03
(b) Peak strength	P_u (kN)	596	-585	611	-583	593	-516	756	-755	585	-591	609	-612	616	-600
	/C-N1	-	-	1.03	1.00	1.00	0.88	1.27	1.29	0.98	1.01	1.02	1.05	1.03	1.03
	/C-N2	-	-	-	-	0.97	0.89	1.24	1.29	0.96	1.01	1.00	1.05	1.01	1.03
(d) Yield drift ratio	δ_u (%)	1.01	-0.97	0.89	-0.85	1.03	-0.66	0.91	-1.00	0.89	-0.77	0.82	-0.82	0.94	-0.74
	/C-N1	-	-	0.87	0.87	1.02	0.68	0.90	1.03	0.87	0.79	0.81	0.84	0.92	0.76
	/C-N2	-	-	-	-	1.16	0.78	1.03	1.18	1.00	0.91	0.93	0.97	1.06	0.88

4.4 Effect of Parameters

4.4.1 Effect of concrete types

Specimens C-N2 and C-G1 shared the same geometry, design and construction method but used different concrete types. As shown in **Figure 4-29**, the geopolymer concrete PC specimen (C-G1) showed equivalent performance until the peak loads to the normal concrete PC specimen (C-N2). Specimen C-G1 experienced strength degradation earlier than specimen C-N2. The yield points were similar but the ultimate points differed. This resulted in lower ductility of specimen C-G1 (35% lower than specimen C-N2) (**Table 4-10**).

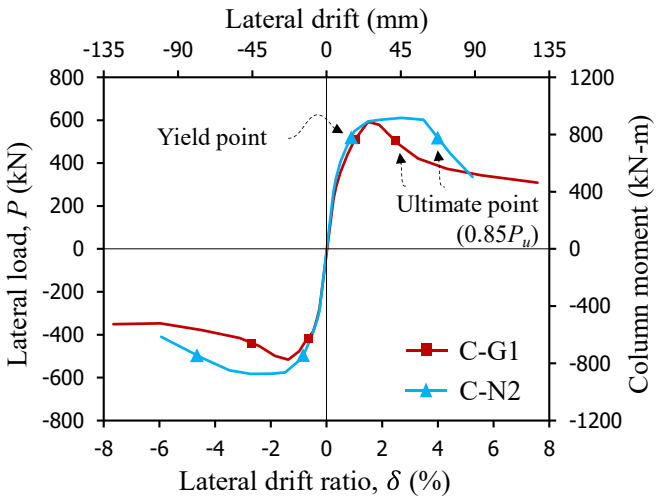

Figure 4-29 Envelop curves of specimens using different concrete types

Table 4-10 Deformation capacity of specimens using different concrete types

	Ultimate drift ratio δ_u (%)		Ductility μ		
Specimen	Pos.	Neg.	Pos.	Neg.	Avg.
C-N2	3.99	-4.66	4.50	5.51	5.01
C-G1	2.47	-2.69	2.40	4.05	3.23

Investigating the previous studies (**Table 4-11**), low ductility of geopolymer beam-column joints has been reported by Ngo et al. (2021) and Mao et al. (2022). Mao et al. (2022) used brittle geopolymer materials, and suggested that micro-cracks of geopolymer concrete induced more significant crack and faster crack development. This brittleness and micro-cracks affected strength degradation, stiffness, stiffness degradation and ductility.

Figure 4-30 exhibits cracking patterns of specimens C-N2 and C-G1. It is found that no significant difference lied in cracking patterns of the specimens using either the normal concrete or the geopolymer concrete. Even the normal concrete specimen (C-N2) suffered the greater number of cracks during the test. Thus, the different performance between specimens C-N2 and C-G1 may be caused by grouting defects, not by concrete types.

Table 4-11 Deformation capacities of geopolymer concrete elements of previous studies

Study	Material			Element	Ductility μ		
	Powder	Activator	A/B ratio		Normal	Geopolymer	Ratio
Ngo et al. (2021)	GGBS, Fly ash	NaOH, Na_2SiO_3	60%	Beam-column connection	2.4	1.8	75%
Raj et al. (2016)	Fly ash	NaOH, Na_2SiO_3	35%	Beam-column connection	2.50	3.68	147%
Saranya et al. (2021)	GGBS, Dolomite	NaOH, Na_2SiO_3	60%	Beam-column connection	3.6	3.4	94%
Mao et al. (2022)	Slag, Fly ash	NaOH, Na_2SiO_3, Na_2CO_3	38-50%	Beam-column connection	4.12 (C30) 3.96 (C50) 3.74 (C70)	3.11 (C30) 2.92 (C50) 2.86 (C70)	75% (C30) 74% (C50) 76% (C70)

1) Activator-solution-to-binder ratio

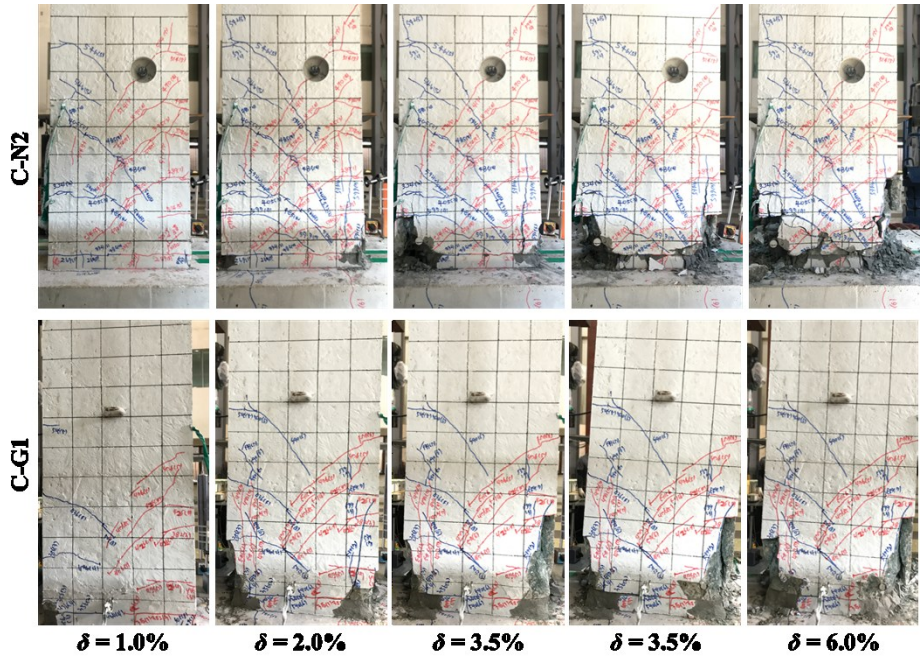

Figure 4-30 Comparison of cracking patterns

4.4.2 Effect of grouting defects

In this study, the PC specimens with grouting defects showed common characters to the previous study on grouting defects of splice sleeves (Xie at el., 2022). The effect of grouting effects was detected in forms of pinching effect of hysteresis curve, lower strength, early failure, failure mode, energy dissipation, and deformation capacity

Xie et al. (2022) reported that pinching effect of hysteresis curves is one of the characters of grouting defects. In the unloading phase of C-G1, C-G1-IMP, and C-G4-IMP, the hysteresis curves were convex in the positive loading and concave in the negative loading, which were opposite to a desirable load-displacement relationship (**Figure 4-31**).

In C-G1, the test strength was 9% lower than the predicted strength in the negative loading. C-G1-IMP and C-G4-IMP failed earlier at 3.5% drift ratio than the others because of grouting defects in splice sleeves. Furthermore, C-G1 failed in sleeve rupture and grout crushing after flexural yielding (**Figure 4-32**).

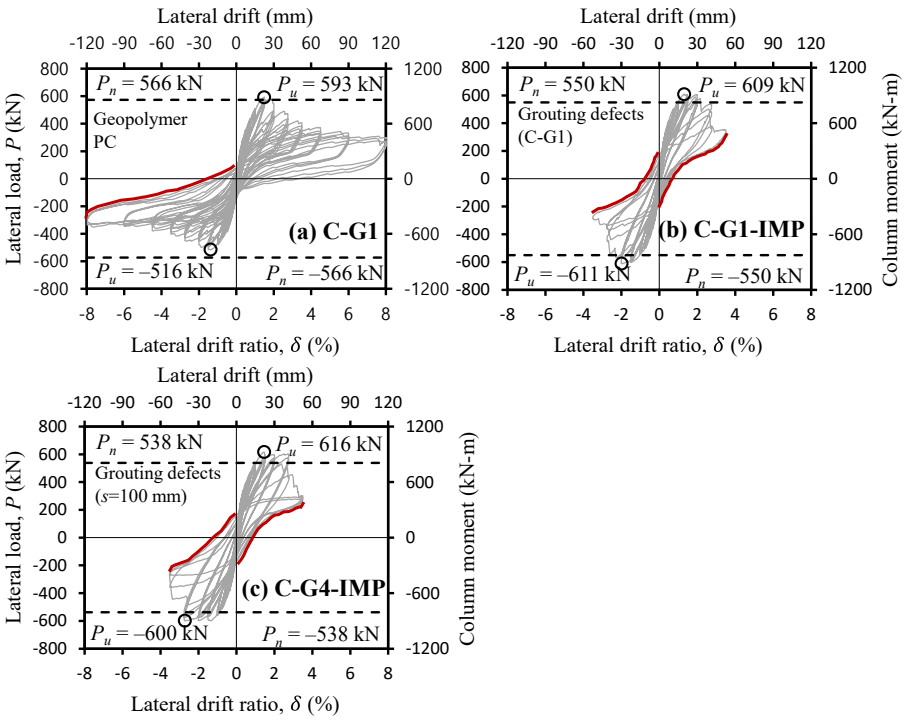

Figure 4-31 Load-displacement relationships of specimens with grouting defects

(a) Sleeve rupture (b) Grouting crushing

Figure 4-32 Failure mode of C-G1

The column specimens with grouting defects (C-G1, C-G1-IMP, C-G4-IMP) showed lower energy dissipation than the specimen without grouting defects (C-N2) (**Figure 4-33**). The specimens failed relatively earlier or, even when lasting longer, showed lower energy dissipation. The cumulative energy dissipation of C-G1, C-G1-IMP, and C-G4-IMP was 32%, 35%, and 10% lower than C-N2, respectively.

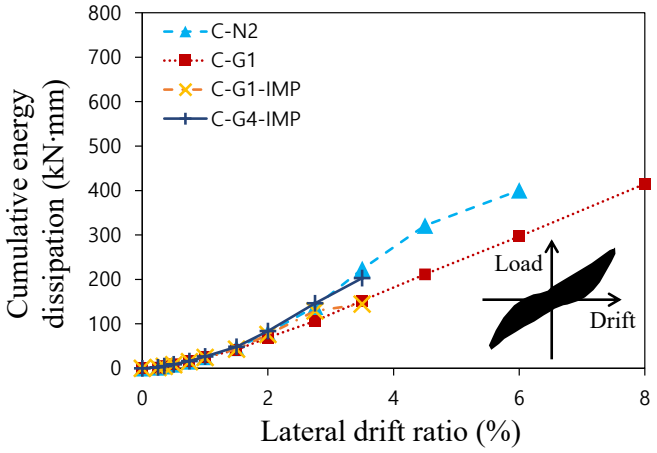

Figure 4-33 Energy dissipation of specimens with and without grouting defects

Poor injecting quality of grouting also affected deformation capacity of the specimens. The specimens with grouting defects (C-G1, C-G1-IMP, C-G4-IMP) showed 26-48% lower ductility than the specimen without grouting defects (C-N2) (**Table 4-12**).

Table 4-12 Deformation capacity of specimens with and without grouting defects

Specimen		Ductility μ		Ductility μ (Specimen/C-N2)	
		Pos.	Neg.	Pos.	Neg.
Without grouting defects	C-N2	4.50	5.51	1.00	1.00
With grouting defects	C-G1	2.40	4.05	0.53	0.74
	C-G1-IMP	2.84	2.88	0.63	0.52
	C-G4-IMP	2.91	3.46	0.65	0.63

4.4.3 Effect of larger-size splice sleeves

Grouting defects can be prevented by using larger-size splice sleeves. This helps injecting quality of grouting better and is frequently used in practice. No study has reported the effect of using larger-size splice sleeves on seismic performance. C-G3 in the study used one-size-larger sleeves than other specimens to investigate the effect of using larger-size splice sleeves. C-G3 used D29 splice sleeves while maintaining D25 rebars.

As illustrated in **Figure 4-34 (a)-(c)**, the specimen with larger-size sleeves (C-G3) showed better load-displacement relationship than the specimens with standard-size sleeves (C-G1, C-G1-IMP, C-G4-IMP). C-G3 did not show any character of grouting defects such as pinching effects in the unloading phase.

The envelope curves in **Figure 4-34 (d)** also presents the same results. The specimen with grouting defects failed at 3.5% drift ratio or showed uneven performance in positive and negative loading. Otherwise, C-G3 showed even and quality load-carrying performance in both positive and negative loading.

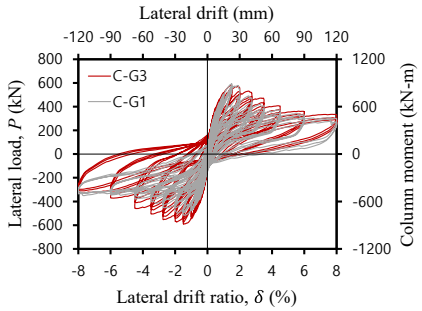

(a) Comparison of C-G1 and C-G3

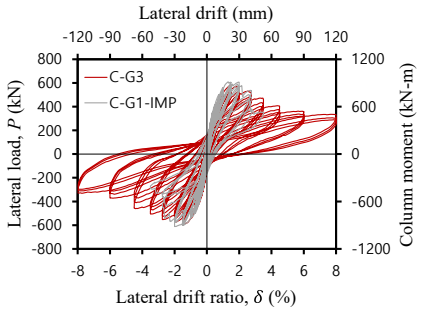

(b) Comparison of C-G1-IMP and C-G3

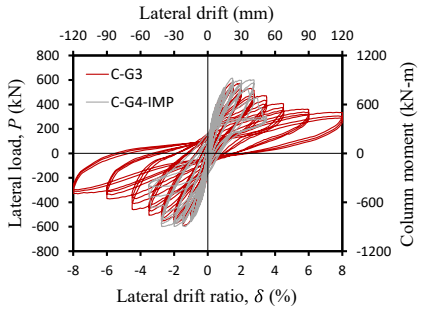

(c) Comparison of C-G4-IMP and C-G3

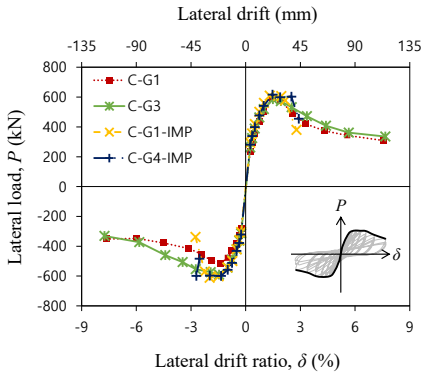

(d) Envelope curves

Figure 4-34 Load-displacement relationships and envelope curves of specimen with and without larger-size sleeves

Good injecting quality of grouting also affected energy dissipation. As illustrated in **Figure 4-35**, The specimens with larger-size sleeves (C-G3) showed higher energy dissipation and lasted longer. Energy dissipation of C-G3 with larger sleeves was 26-40% higher than that of C-G1 after 3.5% drift ratio. The specimens with grouting defects (C-G1-IMP, C-G4-IMP) showed

similar energy dissipation but failed early at 3.5% drift ratio. This implies that grouting defects harm energy dissipation capacity and using one-size large sleeves can prevent it.

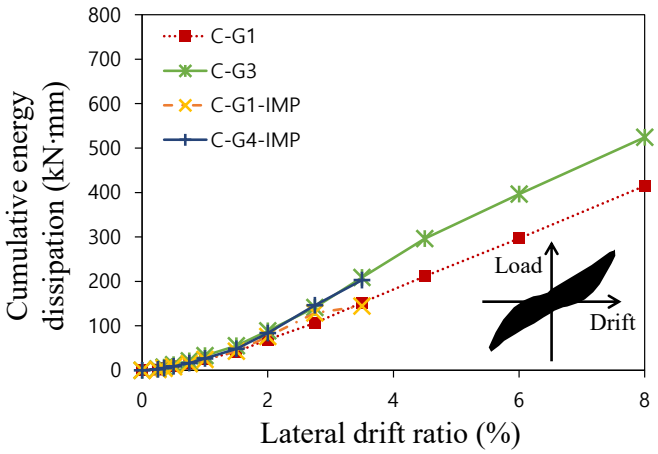

Figure 4-35 Energy dissipation with and without larger-size sleeves

Good injecting quality of grouting induced by using larger-size splice sleeves also affected deformation capacity of the specimens. The specimen with larger-size splice sleeves (C-G3) showed 13-59% higher ductility than the specimens with grouting defects (C-G1, C-G1-IMP, C-G4-IMP) (**Table 4-13**).

Table 4-13 Deformation capacity of specimens with and without larger-size sleeves

Specimen		Ductility μ		Ductility μ (Specimen/C-G3)	
		Pos.	Neg.	Pos.	Neg.
D29 sleeve	C-G3	3.39	4.59	1.00	1.00
D25 sleeve with grouting defects	C-G1	2.40	4.05	0.71	0.88
	C-G1-IMP	2.84	2.88	0.84	0.63
	C-G4-IMP	2.91	3.46	0.86	0.75

4.4.4 Effect of reinforcement ratio

In this study, the geopolymer concrete PC specimens included two different reinforcement ratios. Specimen C-G1 used ρ = 1.62% (8-D25) and specimen C-G2 used ρ = 2.54% (8-D32). The specimen with higher reinforcement ratio (C-G2) showed better performance in terms of load-displacement relationship, energy dissipation and deformation capacity (**Figure 4-36** and **Table 4-14**). No pinching effect was detected in specimen C-G1 unlike specimen C-G1.

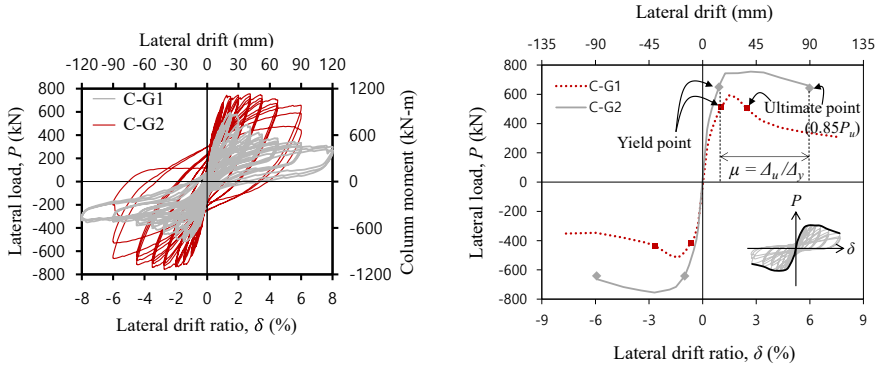

(a) Load-displacement relationship (b) Envelop curve

Figure 4-36 Load-displacement relationships and envelop curves of specimens with different reinforcement ratios

Table 4-14 Deformation capacity of specimens with different reinforcement ratios

	Ultimate drift ratio δ_u (%)		Ductility μ		
Specimen	Pos.	Neg.	Pos.	Neg.	Avg.
C-G1	2.47	-2.69	2.40	4.05	3.23
C-G2	5.99	-5.93	6.56	5.92	6.24

Investigating the failure modes of the PC specimens (from **Figure 4-15** to **Figure 4-20**), the failure mode of specimen C-G2 was different from the other

PC specimens. In overall, the PC specimens suffered limited concrete damage under compression and sudden grout crushing or gradual bond-slip under tension. On the other hand, specimen C-G2 suffered severe concrete crushing.

Figure 4-37 shows the strains of the main bars at each drift ratio. At first, the moment-curvature relationship of the specimens was estimated by a cross-sectional analysis (**Figure 4-37 (a)**). Then, the strains of the main bars could be obtained from strain distribution at each point of the M-ϕ relationship (**Figure 4-37 (b)**). Lastly, the test moment strengths at each drift ratio were matched with the moments of the M-ϕ relationship (**Figure 4-37 (c)**).

When the reinforcement ratio of the section became higher, the strains of the longitudinal reinforcements at the section became lower at the same drift ratio and the compressive zone became deeper. In general, this low steel strain and deep compressive zone cause the concrete to reach the limit state earlier than the steel reinforcements, leading to a less ductile behavior of the section.

However, the specimens in this study failed mainly due to the tensile damage regarding the sleeves or the grout, while the compressive damage of concrete was limited at the concrete cover locally around the column-base interface (**Figure 4-15, Figure 4-16** and from **Figure 4-18** to **Figure 4-20**). If the failure of the specimens is not governed the compressive zone, bond capacity of the longitudinal reinforcements may decide the ductile behavior.

Indeed, in the PC specimens with the same reinforcement ratio (C-N2, C-G1, C-G3), locally high strains of the longitudinal reinforcements at the column-base interface caused gradual bond-slip inside the sleeves (**Figure 4-15, Figure 4-16** and **Figure 4-18**). In this point of view, the precast specimen with higher

reinforcement ratio (C-G2) could prevent bond failure of the longitudinal reinforcements because of the low steel strain so that could maintain the strength after the peak load.

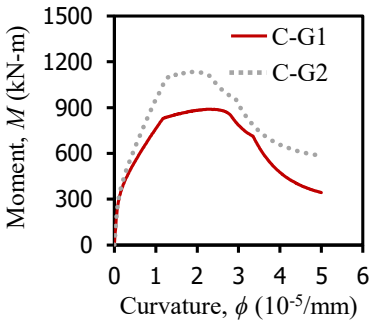

(a) Moment-curvature relationship

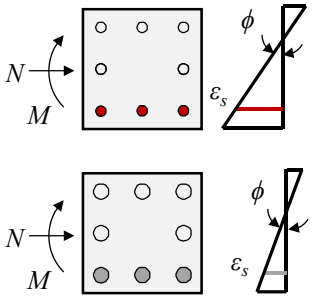

(b) Strain distribution

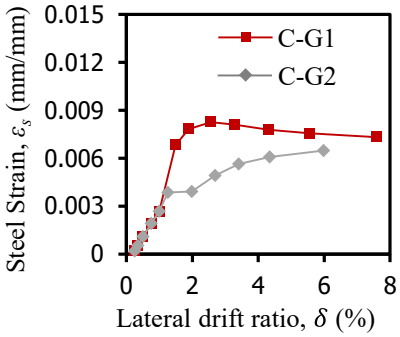

(c) Strain of main bar at each lateral drift

Figure 4-37 Strain of main bar at each lateral drift

4.5 Summary

In this chapter, the cyclic loading tests were conducted to investigate seismic performance of the PC columns using the geopolymer concrete. Total 7 column specimens (2 normal concrete and 5 geopolymer concrete) were tested for cyclic loading tests with 13% compression ratio loaded on the top of the columns. The test parameters included concrete types (normal or geopolymer), construction methods (monolithic or PC), sizes of sleeves (D25, D29), reinforcement ratio (0.0162 or 0.0254), and transverse rebar spacing (100 mm or 200 mm). The same reinforcements details and fabrication methods used in practical PC construction were adopted. The seismic performance of the column specimens was investigated in terms of strength, load-displacement relationship, failure mode, secant stiffness, energy dissipation, and ductility. The seismic performance of each specimen was evaluated by ACI 374.1-05 and AIJ 2002 Guidelines.

For the seismic performance of the PC columns using the geopolymer concrete, the major findings are summarized as follows:

1) The geopolymer concrete columns (C-G1, C-G2, C-G3, C-G1-IMP, and C-G4-IMP) developed the predicted strengths calculated by the design codes (P_u/P_n = 1.03-1.15, except negative loading of C-G1 which had grouting defects).

2) The PC geopolymer concrete columns (C-G1 (positive loading) and C-G3) showed similar or superior seismic performance to the monolithic normal concrete column (C-N1). The PC geopolymer concrete columns resisted

until 8.0% drift ratio, whereas the monolithic normal concrete column failed at 3.5% drift ratio.

3) The PC geopolymer concrete columns (C-G1 (positive loading) and C-G3) showed equivalent seismic performance to the PC normal concrete column (C-N2). The strength, load-displacement relationship, failure mode, and energy dissipation of the PC geopolymer concrete columns were similar to those of the PC normal concrete column. the PC geopolymer concrete columns (C-G1 (positive loading), C-G3) satisfied AIJ 2002 Guidelines for ensuring equivalent performance to the PC normal concrete columns (C-N2).

4) However, ductility of the PC geopolymer concrete columns (C-G1) was 35% lower than that of the PC normal concrete column (C-N2) due to the effect of grouting quality. The cracking patterns and the stress-strain curves were almost the same.

5) The PC columns with grouting defects (C-G1 (negative loading), C-G1-IMP, C-G4-IMP) showed inferior performance to the PC column without grouting defects (C-N2). The test strength was 9% lower than the predicted strength calculated by the design codes. The PC columns with grouting defects showed 10-35% lower energy dissipation and 26-48% lower ductility than the PC column without grouting defects.

6) The PC column with larger-size sleeves (C-G3) prevented grouting defects caused by poor injecting quality of grouting. However, using larger-size sleeves does not mean better seismic performance.

7) The PC column with higher reinforcement ratio (C-G2) showed better performance. It could prevent bond failure of the longitudinal reinforcements inside the splice sleeves because of the low steel strains, so that could maintain the strength after the peak load.

Chapter 5. Cyclic Loading Tests for Beam-column Connections

5.1 Introduction

Only few studies have been reported on the seismic performance of geopolymer concrete members by cyclic loading tests. The results of the studies vary in terms of seismic performance, and the studies adopted various properties of materials including the type of binder materials and the amount of the activator solution.

Monolithic beam-column connections let beam longitudinal reinforcements pass through the joint, while PC beam-column connections require beam bottom longitudinal reinforcements to be anchored in the joint by hooked bars. Design codes specify that when beam reinforcements pass through a joint, the beam reinforcements inside the joint can suffer high bond stresses and bar slip under cyclic loading (refer to **2.1 (k)**).

Design codes denote that hooked bars terminated in a joint should extend far to the opposite face of the joint to help a diagonal compression strut inside the joint to form well (refer to **2.1 (i)**). Proposed nominal strength models of beam-column joints are affected by the point where the hooked bar is terminated or implicitly assume the hooked bar must extend to the far end (refer to **2.4**). However, hooked bars from the opposite sides of a joint are often constructed not to overlap each other due to congestion of reinforcements inside the joint. Furthermore, no study was found on the effect of overlap lengths of hooked bars terminated in a joint.

In this chapter, cyclic loading tests were conducted to investigate seismic performance of PC geopolymer concrete beam-column connections with 90° hooked bars anchored in the joint. The structural performance of PC geopolymer concrete beam-column connections was evaluated by whether the specimens developed nominal strengths calculated by design codes. The test results of PC geopolymer concrete beam-column connection specimens were compared with that of monolithic normal concrete specimen in terms of seismic performance.

Moreover, the effect of PC construction method using joint hook anchorage on the seismic performance of beam-column connections was evaluated. The effect of presence of joint hook anchorage and the effect of different overlap lengths were investigated. Furthermore, the seismic performance of each specimen was evaluated by ACI 374.1-05 and AIJ 2002 Guidelines.

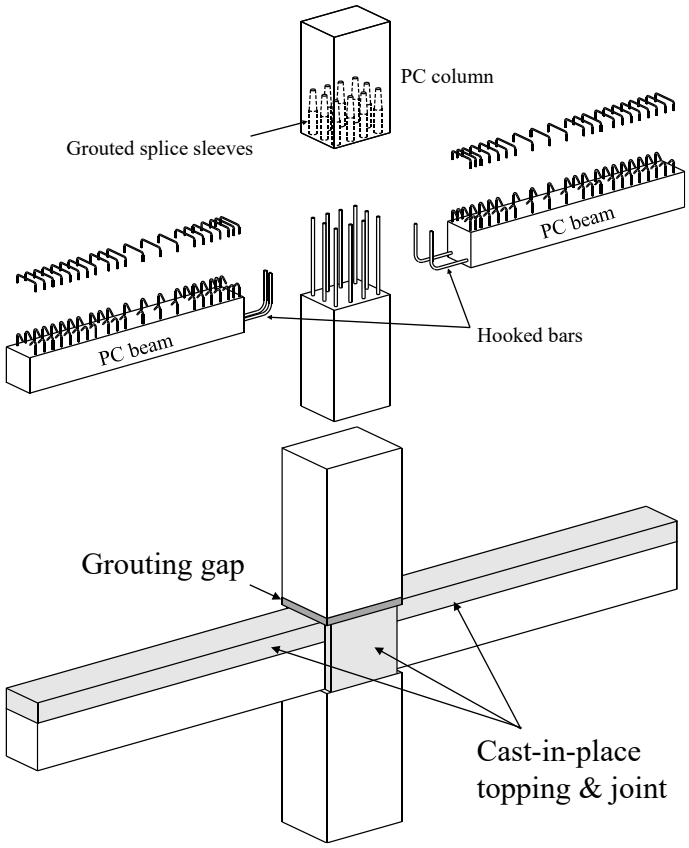

Figure 5-1 PC beam-column connection

5.2 Test Program

5.2.1 Test parameters

Table 5-1 shows the test parameters of beam-column joint specimens, such as concrete types, construction methods, and anchorage hooks. In the specimen names, the letters 'N' and 'G' denote concrete types except panel zone (normal concrete and geopolymer concrete, respectively).

Table 5-1 Test parameters of beam-column connection specimens

Specimen	Concrete type			Construction method	Beam bottom bar detail	Overlap length (mm)
	Joint	Column	Beam			
J-N1	Normal	Normal	Normal	Monolithic	Penetrating	-
J-G1	Normal	Geopolymer	Geopolymer	PC	90° hook	290
J-G2	Normal	Geopolymer	Geopolymer	PC	90° hook	170

The specimens can be grouped by the one control specimen (J-N1) and the two experimental specimens (J-G1 and J-G2). The control specimen (i.e. J-N1) represents monolithic beam-column connections. It was monolithically made with normal concrete and both top and bottom beam longitudinal reinforcements penetrate the joint. On the other hand, the experimental specimens represent PC beam-column connections. The beams and columns were constructed as PC members and connected by the cast-in-place (CIP) panel zone and 150-mm-height topping concrete. The PC members were made of the geopolymer concrete and CIP panel zone and topping used normal concrete. Both two PC specimens have details of 90° anchorage hooks for beam bottom longitudinal reinforcements inside the joints, while beam top longitudinal reinforcements still penetrated the joints. The difference between

two PC specimens is in the overlap length of hooks. J-G1 has relatively long overlap length of hooks, 290 mm. J-G2 has relatively short overlap length, 170 mm. The different overlap lengths were caused by using different sizes of rebars meeting development length specified in the design code.

5.2.2 Details of test specimens

Figure 5-2 shows details of test specimens for cyclic loading beam-column connection tests. The beam-column connection specimens were composed of two beams, two columns and a joint. The section of the columns was 500 mm width × 650 mm height and the section of beams was 350 mm width × 500 mm height. The total vertical height of the columns was 2800 mm and the net height from the loading point at upper column to the reaction point at lower column was 2100 mm. The total horizontal length of the beams was 5600 mm and the net length between the supports was 4800 mm.

Figure 5-2 (a) shows the details of the monolithic specimen (i.e. J-N1). The specimen was monolithically constructed with the normal concrete. Both four top D25 bars (bar diameter d_b = 25.4 and yield strength f_y = 658.0 MPa) and two bottom D25 bars of the beams passed through the joint. The column transverse reinforcements started 100 mm up and 50 mm down from the joint face, respectively. Their spacing was 200 mm, but near the loading and reaction points 50 mm in order to prevent local shear failure.

Figure 5-2 (b) and **(c)** shows the details of the PC specimens (i.e. J-G1 and J-G2). Two columns and two beams were separately constructed with the geopolymer concrete as PC members. They were connected by cast-in-place

(CIP) topping and joint and grouted splice sleeve connection. The normal concrete was used in CIP topping and joint. The 50-mm grouting gap was located between the joint face and the upper column in order to consider a construction error and enhance the connectivity. The column transverse reinforcements started 80 mm up from the grouted face and 50 mm down from the joint face, respectively. Their spacing varied by each zone; 50 mm near the loading point to prevent local shear failure, 60 mm in the sleeve zone to prevent shear reinforcements from being unfastened., and 200 mm in the lower column.

The difference between J-G1 and J-G2 lied in beam bottom longitudinal reinforcements details. J-G1 used two D25 bars as the beam bottom longitudinal reinforcements with standard 90° hook anchorage. The calculated development length was 470 mm, and the overlap length of both anchorage hooks was 290 mm. Meanwhile, J-G2 used three D22 bars (bar diameter d_b = 22.2 mm and yield strength f_y = 672.4 MPa) as the beam bottom longitudinal reinforcements with standard 90° hook anchorage, whose reinforcement ratio was similar to that of J-G1; 0.65% for J-G1 and 0.74% for J-G2. Even though the reinforcement ratios were similar, their development lengths were different since the development lengths are a function of bar diameters. The calculated development length of D22 was 410 mm, and the overlap length of both anchorage hooks was 170 mm.

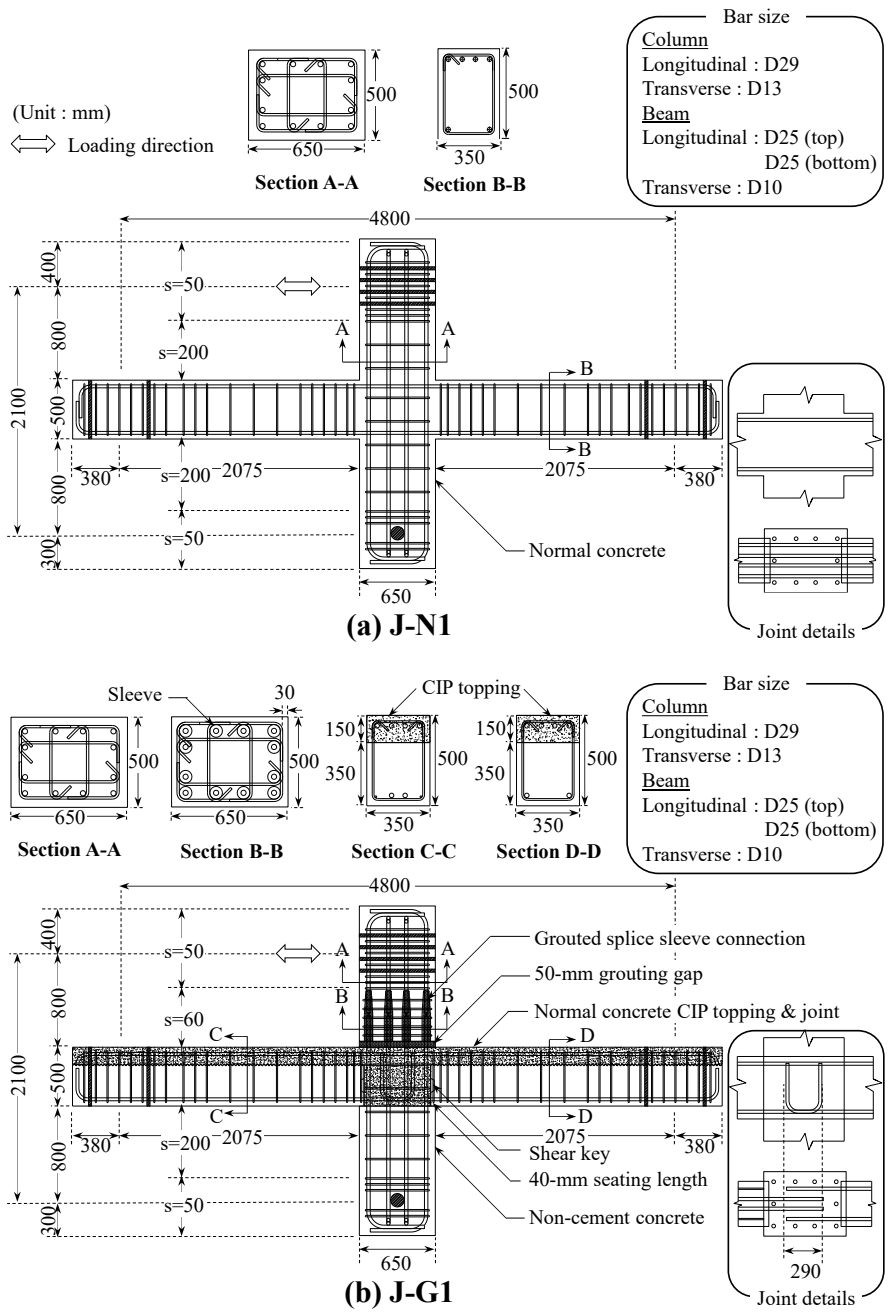

Figure 5-2 Details of beam-column connection specimens

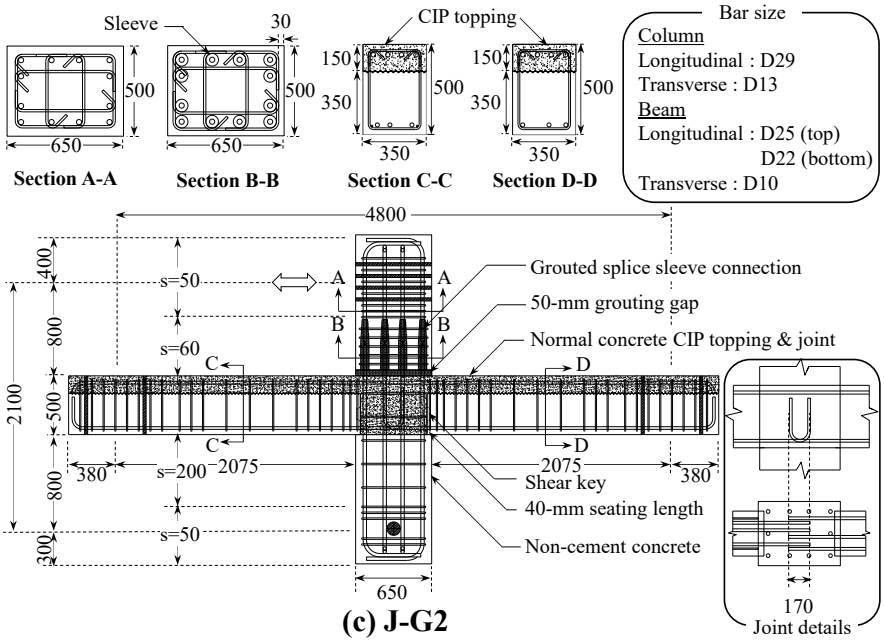

Figure 5-2 Details of beam-column connection specimens (continued)

5.2.3 Specimen construction

The construction of the beam-column connection specimens can be divided into three parts (PC member construction, CIP topping and joint, and upper column assembly). Procedures of the construction are illustrated in **Figure 5-3** to **5-5**.

(a) Assembling steel cages

(b) Attaching strain gauges

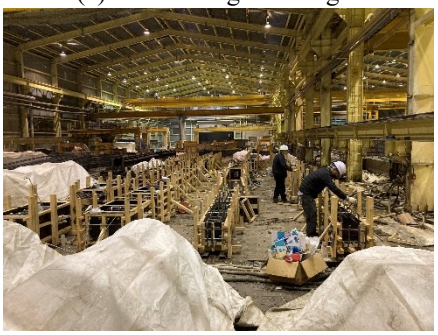

(c) Manufacturing mold

(d) Placing concrete and curing

Figure 5-3 Construction procedures of beam-column connection specimens: PC member construction

(a) Assembling members and manufacturing mold

(b) Assembling beam top bars and stirrups

(c) Details of J-G1 inner-joint hooks

(d) Details of J-G2 inner-joint hooks

(e) CIP topping and joint

(f) Curing

Figure 5-4 Construction procedures of beam-column connection specimens: CIP topping and joint

(a) Before assembling

(b) Assembling upper column and manufacturing mold

(c) Injecting non-shrinkage grout

(d) Curing

Figure 5-5 Construction procedures of beam-column connection specimens: upper column assembly

5.2.4 Material strength

Figure 5-6, 5-7 and **Table 5-2, 5-3** show the material strength tests and the resulting material strength. When placing concrete, concrete cylinders (100 mm diameter × 200 mm height) were prepared for compressive tests. They were cured under the same condition as that of the test specimens. The compressive tests of concrete cylinders were conducted on each day of the experiments as shown in **Figure 5-6 (a)**. The speed of loading was 0.4 MPa/s by the load control method according to KS specification. On the both sides of the cylinders, concrete strain gauges were attached to measure strains. The compressive strengths of the concrete of each test specimen are shown in **Table 5-2**.

When grouting, non-shrinkage grout specimens (40 mm × 40 mm × 160 mm) were prepared for compressive test. The compressive tests of non-shrinkage grout specimens were conducted as shown in **Figure 5-6 (b)**. The speed of loading was 1 mm/s by the displacement control method. Concrete strain gauges were attached on the both sides to measure strains. The average compressive strength of the non-shrinkage grout of the test specimens is shown in **Table 5-2**.

When assembling steel cages, steel rebar specimens (600 mm length, in case of D32, 700 mm length) cut from the rebars used for manufacturing the test specimens were prepared for tensile test. The tensile tests of the steel rebars were conducted as shown in **Figure 5-6 (c)**. The speed of loading was 2 mm/s by the displacement control method, and after a rebar yielded, gradually increased up to 8 mm/s. On the center of the steel rebar specimens, steel strain gauges were attached to measure strains. The material strengths and stress-strain relationships of steel rebars of the test specimens are shown in **Table 5-3**

and **Figure 5-7**, respectively.

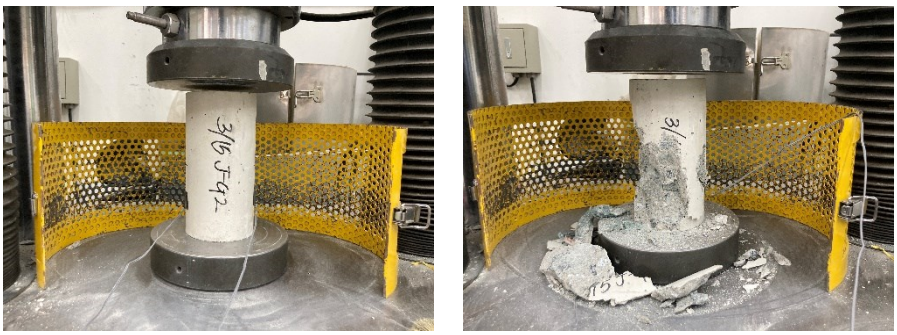

(a) Concrete cylinder compressive test

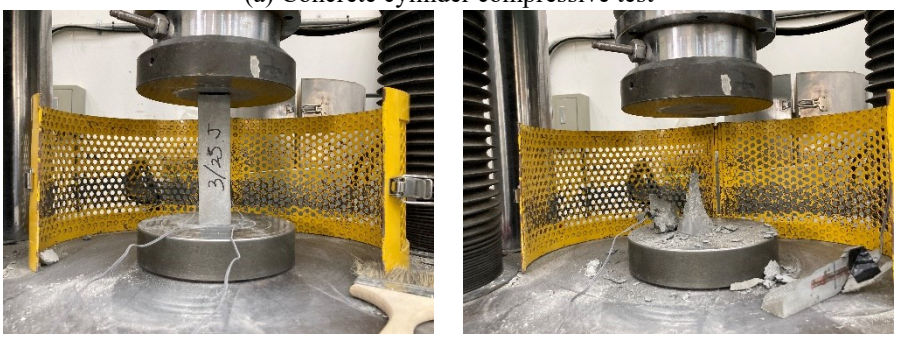

(b) Non-shrinkage grout compressive test

(c) Steel rebar tensile test

Figure 5-6 Material strength tests of the beam-column connections

Table 5-2 Compressive material strength test results of beam-column connections

Specimen	Concrete			Non-shrinkage grout
	Monolithic	PC	CIP topping & joint	
J-N1	62.3	-	-	-
J-G1	-	61.2	52.6	94.3
J-G2	-	62.8	48.5	94.6

Unit: mm

Table 5-3 Tensile material strength test results of beam-column connections

Specimen	Bar diameter d_b (mm)	Yield strength f_y (MPa)	Ultimate strength f_u (MPa)	Yield strain ε_y
SD500 D13	12.7	552.8	653.7	0.00276
SD600 D22	22.2	672.4	789.6	0.00336
SD600 D25	25.4	658.0	775.4	0.00329
SD600 D29	28.7	625.1	741.4	0.00313

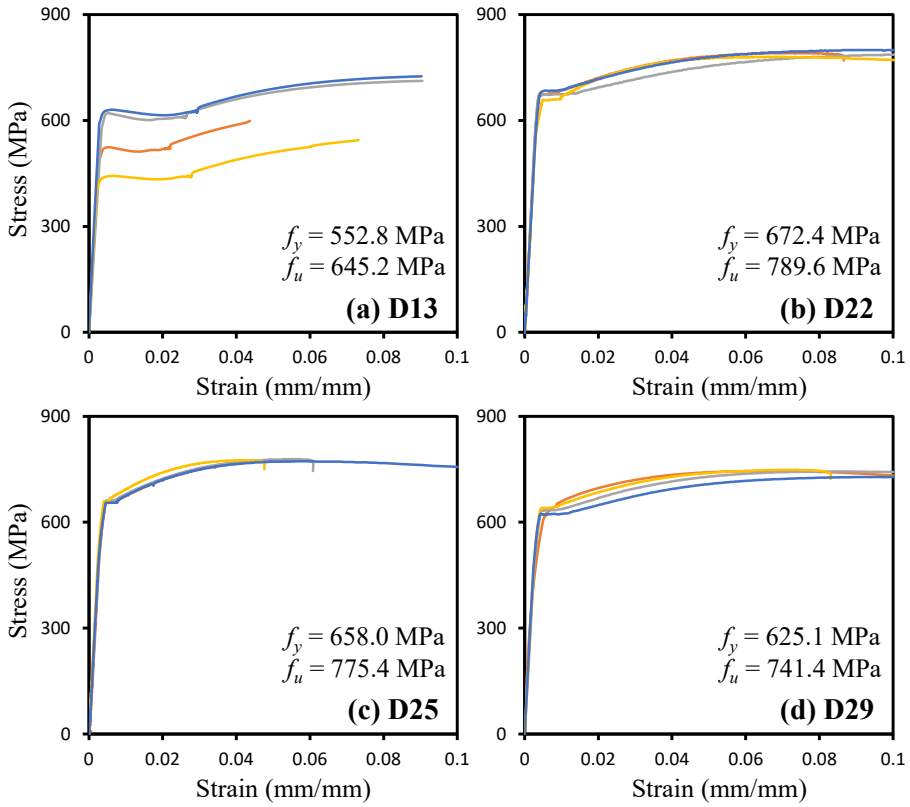

Figure 5-7 Tensile material strength test results of beam-column connections

5.2.5 Test setup and loading plan

Figure 5-8 shows the test setup for cyclic loading tests of the beam-column connection specimens. Both beam ends were roller supported. The bottom of the lower column was pin supported. Cyclic lateral loading applied to the upper column simulated earthquake load acting to the column. Here, 2,000 kN actuator was used.

The loading plan of the beam-column connection tests followed ACI 374.1-05, and are shown in **Figure 5-9** and **Table 5-4**. ACI 374.1-05 recommends that each step include three cycles and an incremental ratio of displacements be in the range from 1.25 to 1.5.

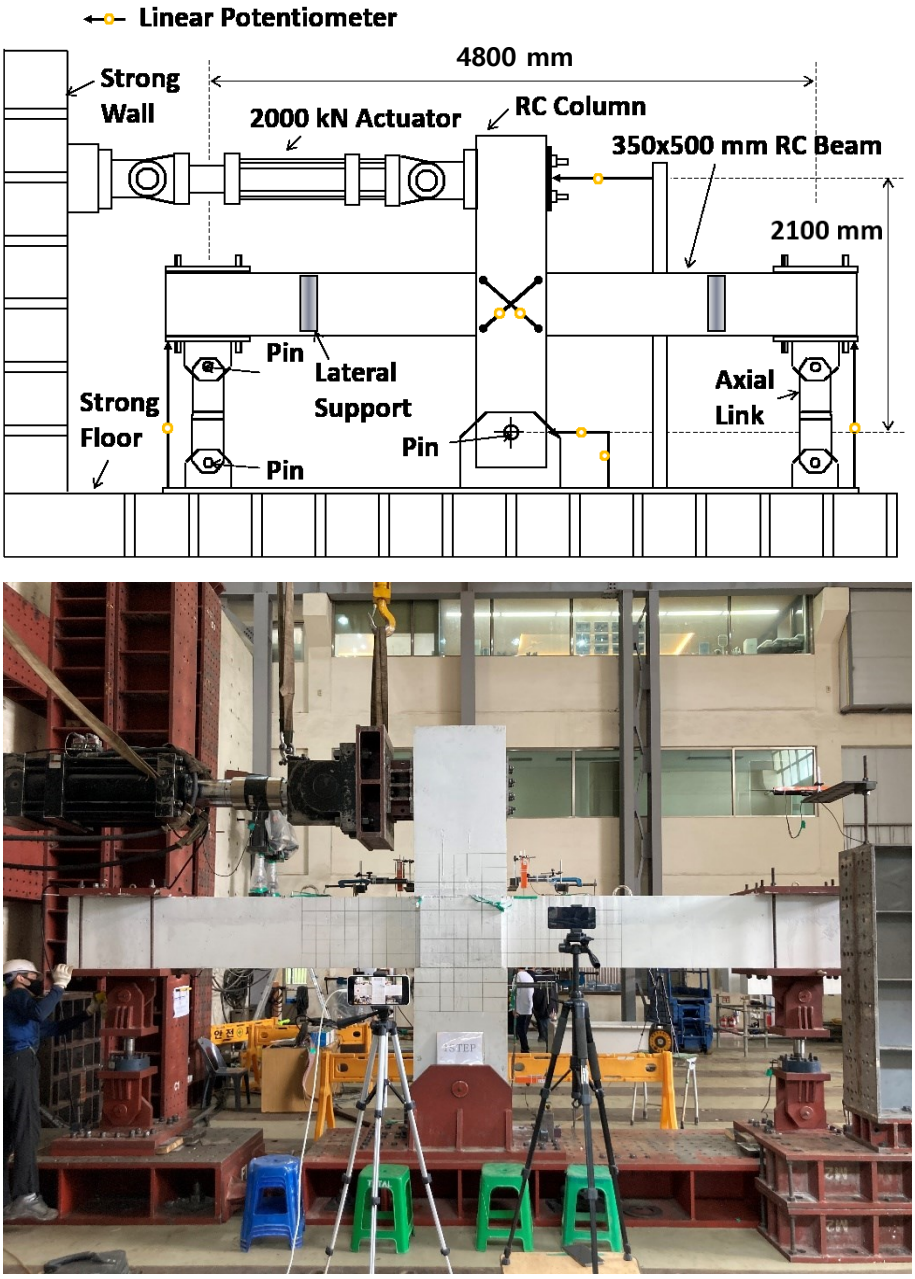

Figure 5-8 Test setup of the beam-column connection tests

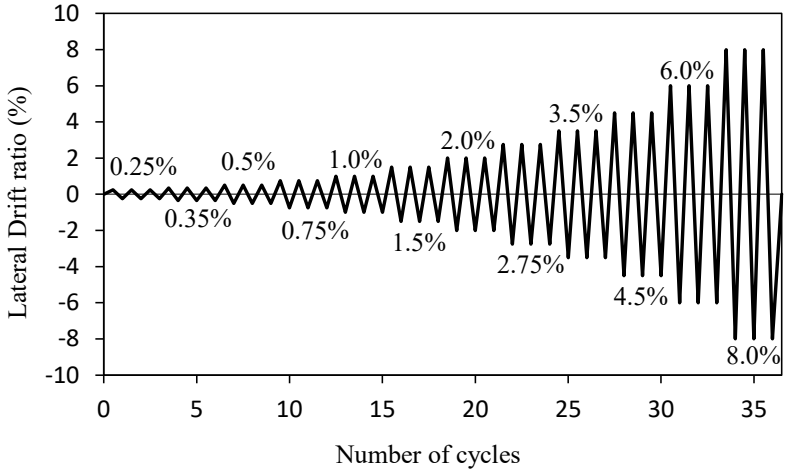

Figure 5-9 Loading plan of the beam-column connection tests

Table 5-4 Loading plan of the column tests

Step	Lateral drift ratio[1)] (%)	Net lateral displacement[2)] (mm)	Number of load cycles	Incremental ratio[3)]
1	0.25	5.25	3	-
2	0.35	7.35	3	1.40
3	0.5	10.5	3	1.42
4	0.75	15.75	3	1.50
5	1.0	21	3	1.33
6	1.5	31.5	3	1.50
7	2.0	42	3	1.33
8	2.75	57.75	3	1.37
9	3.5	73.5	3	1.27
10	4.5	94.5	3	1.28
11	6.0	126	3	1.33
12	8.0	168	3	1.33

1) (Net lateral displacement) ÷ (Net height of columns)

2) (Displacement of the actuator) – (Bottom hinge slip) – (rigid body rotation)

3) (Current displacement) ÷ (Previous displacement)

5.2.6 Measurement plan

To measure deformations around the joint, strain gauges were attached to 24 spots on the steel cages. In the beams and the columns, the strain gauges were attached to the reinforcements near the joint. The stain of the column longitudinal reinforcements inside the joint was measured at 20–30 mm beneath the connection face to investigate transmission of stress from the column to the joint. The strain gauges were also attached to the hoops inside the joint to investigate amount of stress in the transverse reinforcements inside the joint. In the monolithic specimen, the strain gauges were located at the same spot.

To measure deformations of the test specimens, 11 linear variable displacement transducers (LVDT) were installed on the specimens. The actuator displacement and the slip at the lower column were measured by the horizontal LVDTs on the top and the bottom, the rigid body rotation by the vertical LVDTs on both beam ends, the beam flexural deformation and the gap opening by the horizontal and vertical LVDTs on the corner of the joint, respectively. The joint shear deformation by the X-shaped LVDTs on the joint.

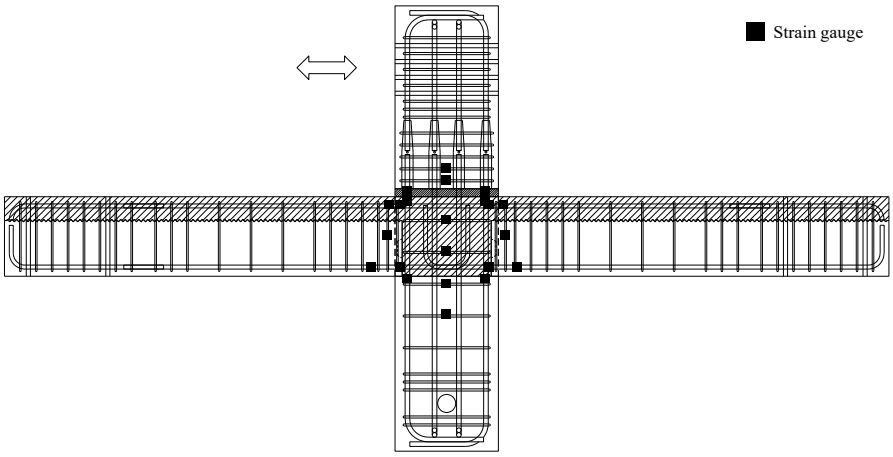

(a) Strain gauge plan

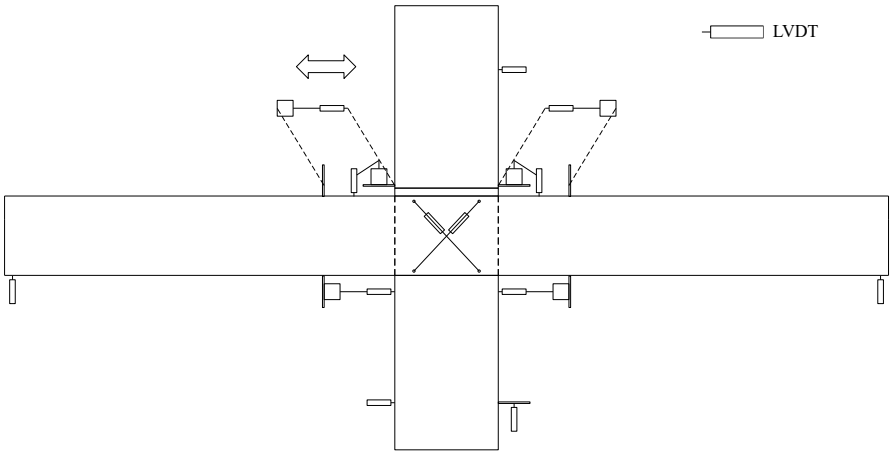

(b) LVDT plan

Figure 5-10 Measurement plan of beam-column connection specimens

5.3 Prediction of Possible Failure Mode and Estimation of Nominal Strength

Possible failure modes can be classified into flexural yielding of beam or column, joint shear failure, anchorage failure of hooked bars, and bond failure of longitudinal bars. All test specimens were designed to fail in beam flexural failure mode. The five failure modes including beam flexural failure mode were considered and described below.

5.3.1 Flexural yielding of beam or column

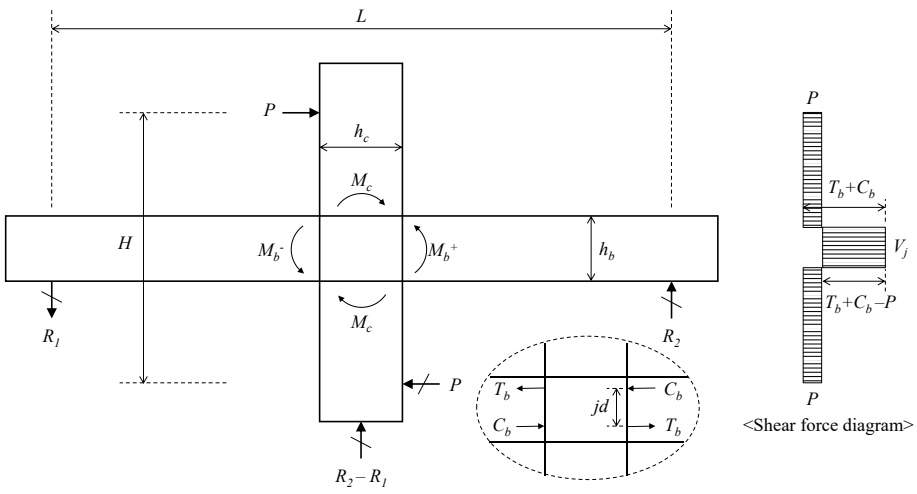

Figure 5-11 Internal and external forces acting on beam-column connections

A nominal strength of a test specimen due to column flexural yielding (P_{nc}) can be calculated by considering column moments at the joint face to reach the nominal moment strengths of the columns. Then, the nominal strength of the

test specimen is calculated by dividing the nominal moment strength (M_{nc}) by the shear span ($a = (H - h_b)/2$).

$$P_{nc} = \frac{2M_{nc}}{H - h_b} \quad \text{Eq 5-1}$$

A nominal strength of a test specimen due to beam flexural yielding (P_{nb}) can be calculated by considering beam moments at the both joint faces to reach the nominal moment strengths of the beams. The beam support reactions at both ends should be calculated at first by force equilibrium ($R_1 + R_2 = 2PH/L$). Assuming that the beam moments at the joint face reach the nominal moment strengths of the beams, the beam support reactions can be calculated ($R_1 = M_b^-/a$; R2 = M_b^+/a; where $a = (L - h_c)/2$). By combining the two equations and organizing it in terms of P, the nominal strength can be obtained:

$$P_{nb} = \left(\frac{M_b^+ + M_b^-}{L - h_c}\right)\frac{L}{H} \quad \text{Eq 5-2}$$

Here, M_b^+ and M_b^- are the positive and negative nominal moment strengths of the beams, respectively.

5.3.2 Joint shear failure

A nominal strength of a test specimen due to joint shear failure (P_{nj}) can by calculated by considering that the joint is subjected to the nominal joint shear strength. In this study, the joint shear strength of ACI 352R-02 was used (refer to **2.1 (l)**).

$$V_n = 0.083\gamma\sqrt{f_c'}b_j h_c \quad \text{Eq 5-3}$$

where γ is a value regarding connection types, and b_j is the effective joint width. For joints with a continuous column and two opposite beams, γ is 20 for ordinary moment frames, and 15 for intermediate or special moment frames (for moment frames, refer to **2.1 (h)**). In this study, γ-value of 15 was selected to conservatively evaluate the joint shear strength even though the test specimens did not fully satisfy the details of intermediate or special moment frames.

The joint shear force (V_j) induced by lateral force (P) can be calculated as follows:

$$\begin{aligned} V_j &= T_b + C_b - P \\ &= \frac{M_b^+ + M_b^-}{jd} - P \\ &= P\left(\frac{H}{L}\right)\left(\frac{L - h_c}{jd}\right) - P \end{aligned} \qquad \text{Eq 5-4}$$

Here, jd is moment arm length of the beams.

By organizing the equation in terms of P and substituting V_{jn} for V_j, the nominal strength can be calculated. Here, the moment arm length is assumed ($jd \approx 0.87d$).

$$P_{nj} = \frac{V_{jn}}{\left(\frac{H}{L}\right)\left(\frac{L - h_c}{0.87d}\right) - 1} \qquad \text{Eq 5-5}$$

5.3.3 Anchorage failure of hooked bars

The anchorage lengths of the hooked bars of the PC specimens were calculated by ACI 352R-02 which is the same as KDS 14 20 52 :2022 and ACI 318-14 (refer to **2.1 (j)**; here, the multiplier 0.7 was incorporated). The anchorage lengths (l_{dh}) were designed to be equal to required anchorage lengths calculated by the code. However, the actual material strengths were greater than the specified strengths, which decreased the required anchorage lengths. The actual anchorage lengths were 14-21% higher than the required anchorage lengths as shown in **Table 5-5**.

Table 5-5 Anchorage length of PC beam-column connection specimens

	Dimension		Requirement							
			Design				Actual			
Specimen	d_b (mm)	$l_{dh,actual}$ (mm)	f_y (MPa)	f_{ck} (MPa)	$l_{dh,req}$ [1)] (mm)	$l_{dh,design}$ /$l_{dh,req}$	f_y (MPa)	f_c' (MPa)	$l_{dh,req}$ [1)] (mm)	$l_{dh,actual}$ /$l_{dh,req}$
J-G1	25.4	470	600	30	467	1.00	658.0	52.6	387	1.21
J-G2	22.2	410	600	30	409	1.00	672.4	48.5	360	1.14

1) The anchorage lengths calculated by ACI 352R-02, KDS 14 20 52 :2022 and ACI 318-14 (refer to **2.1 (j)**)

5.3.4 Bond failure of beam longitudinal bars

According to ACI 352R-02, a wide column depth is recommended to limit slippage of straight bars passing through the joint (refer to **2.1 (k)**). During cyclic loading, straight bars inside the joint may slip, which may cause bond failure. KDS 14 20 80 :2022 also specifies required column-depth-to-bar-diameter ratio of beam-column connections (refer to **2.1 (k)**).

As shown in **Table 5-6**, the actual column-depth-bar-diameter ratio of the specimens (beam top longitudinal reinforcements of J-N1, J-G1 and J-G2 and

beam bottom longitudinal reinforcements of J-N1) satisfied KDS 14 02 80 :2022 but was lower than the required value of ACI 352R-02.

Table 5-6 Column-depth-to-bar-diameter ratio of beam-column connection specimens

				h_c/d_b		
Specimen	h_c	d_b	f_y	Specimen	KDS	ACI 352
J-N1 J-G1 J-G2	650	25.4	658.0	25.6	25.0	31.3

5.3.5 Estimation of nominal strength of test specimens

As shown in **Table 5-7**, all test specimens were designed to fail in beam flexural yielding. The test specimens were reinforced enough to avoid shear failure in the beams and the columns (for the nominal shear strength, refer to **2.1 (g)**). The nominal moment capacities of the columns were design to be larger than those of the beams. The nominal shear strength of the joint was designed to be safe even when nominal moment strengths of the beams were developed. Therefore, nominal lateral force capacities were calculated based on the beam moment strengths. All nominal strengths were calculated with respect to the material test results. The predicted failure mode of all test specimens was beam flexural yielding. The anchorage lengths of hooked bars were longer than the required lengths.

Table 5-7 Estimation of nominal strengths and failure modes of beam-column connection specimens

	Column yielding		Beam yielding			Joint shear failure		Nominal strength	Predicted failure mode		
Specimen	M_{nc} (kN-m)	P_{nc} (kN)	M_{nb}^{+} (kN-m)	M_{nb}^{-} (kN-m)	P_{nb} (kN)	V_{jn} (kN)	P_{nj} (kN)	P_n (kN)		$l_{dh,actual}$ /$l_{dh,req}$	h_c/d_b
J-N1	939	1173	288	551	462	3194	871	462	Beam flexural yielding	-	25.6
J-G1	937	1172	288	551	462	2935	800	462		1.21	25.6
J-G2	939	1174	311	552	475	2818	772	475		1.14	25.6

M_{nc} : nominal moment strength of column
P_{nc} : nominal lateral force capacity due to column flexural yielding
M_{nb}^{+} : nominal positive moment strength of beam
M_{nb}^{-} : nominal negative moment strength of beam
P_{nb} : nominal lateral force capacity due to beam flexural yielding
V_{jn} : nominal shear strength of joint
P_{nj} : nominal lateral force capacity due to joint shear failure
P_n : nominal lateral force capacity due to predicted failure mode
$l_{dh,actual}$: actual development length of hooked bars
$l_{dh,req}$: required development length of hooked bars calculated by ACI 352R-02 (the same as KDS 14 20 52 :2022 and ACI 318-14; refer to (refer to **2.1 (k)**))
h_c : depth of column
d_b : diameter of beam longitudinal bar

5.4 Test Results and Observations

5.4.1 Load-displacement relationship

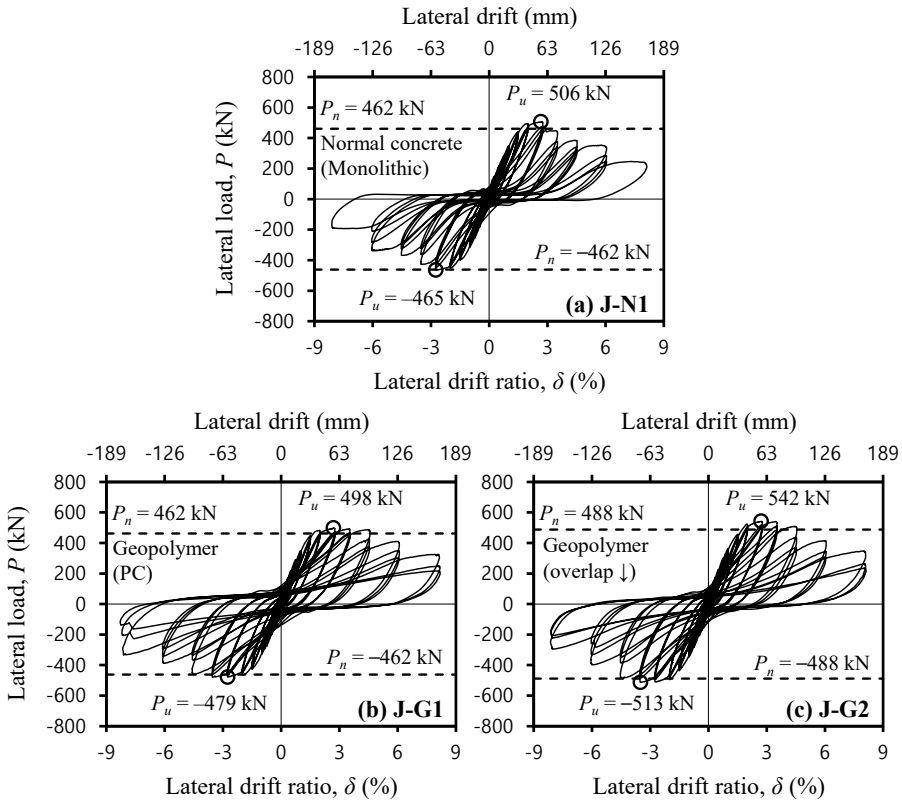

Figure 5-12 Load-displacement relationship of beam-column connection specimens

Figure 5-12 shows relationships between lateral load (P) and lateral displacement ratio (δ) of the beam-column connection specimens with either geopolymer concrete or normal concrete. The lateral drift ratio was calculated by dividing lateral drift with loading height (H = 2100 mm). The lateral drift was calculated by deducting an effect of the slip at the lower column hinge and the rigid body rotation of the specimen. The test strength (P_u) is presented by a

round mark, and the predicted strength (P_n) is presented by a horizontal dashed line. The predicted strength (P_n) is calculated in **5.3.5**. All three specimens showed greater test strengths than the predicted strengths.

The specimens with different overlap lengths of hooked bars (J-G1 and J-G2) showed no significant difference. This is because the failure was caused by beam flexural failure not joint shear failure and the specimens did not suffer severe steel deformation in the joint.

Specimen J-N1 was the monolithic specimen with normal concrete. The test strength was +506kN (δ = 2.75%) and –465kN (δ = 2.75%), and this was respectively 10% and 1% higher than the predicted strength, 462kN. At the first load cycle of 3.5% drift ratio, the load decreased as beam bottom concrete was spalled around the joint face. The load continued decreasing as beam bottom crushing became severe. The test ended at 8.0% drift ratio. Joint damage was hardly detected, but severe concrete spalling happened around beam bottom reinforcement near the joint face. The pinching effect occurred on the unloading phase.

Specimen J-G1 was the PC specimen with the geopolymer concrete and the hooked bar overlap length of 290mm. The test strength was +498kN (δ = 2.75%) and –462kN (δ = 2.75%), which was respectively 8% and 4% higher than the predicted strength, 462 kN. At 4.5% drift ratio, joint diagonal crack was detected and beam top and bottom concrete started to be spalled. The test ended at 8.0% drift ratio.

Specimen J-G2 was the PC specimen with the geopolymer concrete and the hooked bar overlap length of 170mm. The test strength was +542kN (δ = 2.75%)

and –513kN (δ = 3.5%), which was respectively 11% and 5% higher than the predicted strength, 488 kN. At 4.5% drift ratio, the load decreased as the beam top and bottom concrete started to be spalled. The test ended at 8.0% drift ratio. At the joint occurred severer diagonal cracks than those of J-G1 which had the longer overlap length of the hooked bars.

5.4.2 Failure mode

Figure 5-13 shows failure pictures after the tests ended. In all specimens, plastic hinges were formed at the beams and concrete spalling and crushing were detected. After the maximum load, J-N1 suffered bond damage of beam bottom longitudinal bars rather than joint damage. Both J-G1 and J-G2 suffered cracking damage on the joint and concrete crushing on beam top region at the joint face, and J-G2 suffered severe damage on the joint than that of J-G1.

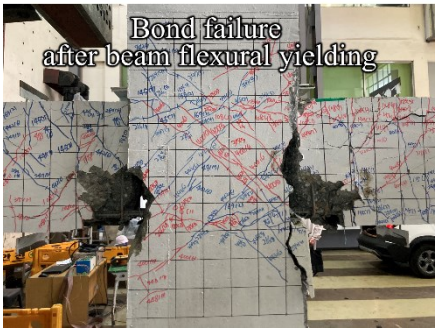

(a) J-N1

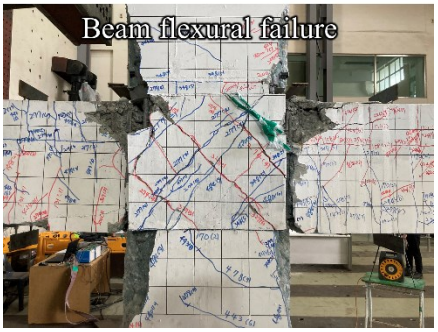

(b) J-G1

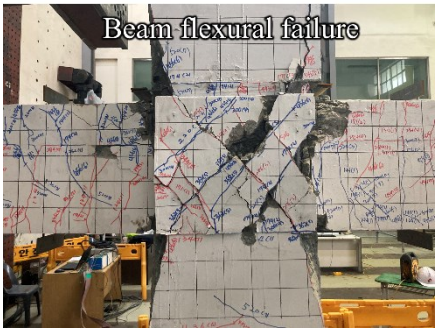

(c) J-G2

Figure 5-13 Final failure pictures of beam-column connection specimens

As shown in **Figure 5-14**, the monolithic specimen (J-N1) suffered concrete crushing and bond damage at the bottom of the beams. Joint damage was hardly detected. Unlike J-G1 and J-G2, bond damage was severe under cyclic loading at the beam bottom longitudinal reinforcements as concrete at the bottom of the beams was spalled after concrete crushing. At the joint, only few diagonal cracks occurred.

As shown in **Figure 5-15**, J-G1 suffered concrete crushing at the corner of the beams and joint cracking damage. Concrete was crushed as plastic hinges were formed at the top and bottom of the beams. Diagonal cracks occurred at the joint, but were not severe until drift ratio 8.0%. The corner concrete cover of the upper and lower columns was spalled around the joint face. The damage was concentrated on the top and bottom corners of the beams.

As shown in **Figure 5-16**, J-G2 suffered similar damage patterns with J-G1 but joint cracking damage was severer. The width of joint diagonal cracks was larger because the overlap length of the hooked bars inside the joint was shorter. The corner concrete cover of the upper and lower columns was spalled around the joint face.

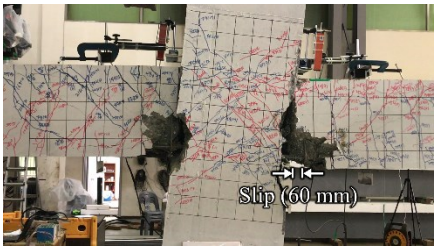

(a) Maximum positive drift (δ = 8.0%)

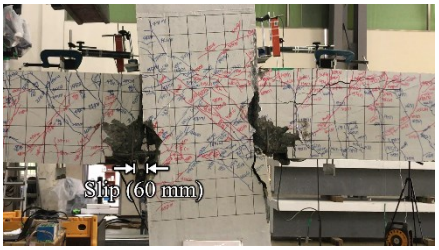

(b) Maximum negative drift (δ = 8.0%)

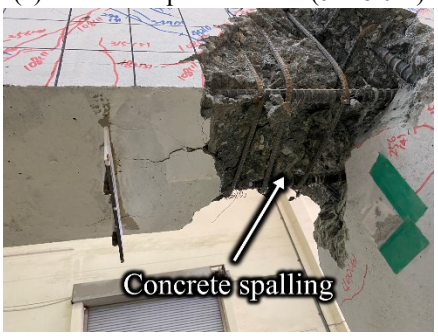

(c) Left beam bottom

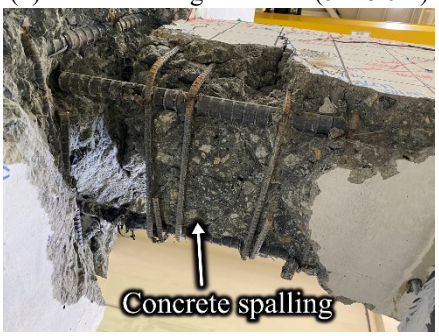

(d) Right beam bottom

(e) Front joint

(f) Back joint

Figure 5-14 J-N1 detailed failure pictures

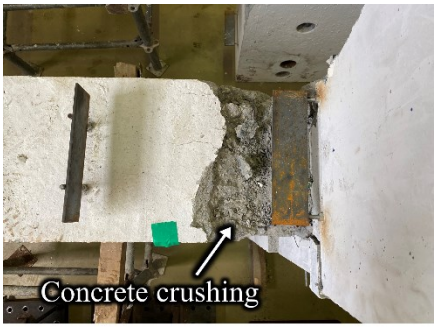

(a) Left beam top

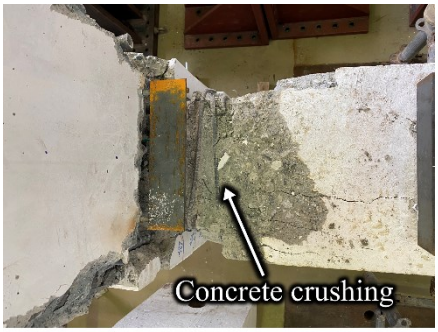

(b) Right beam top

(c) Left beam bottom

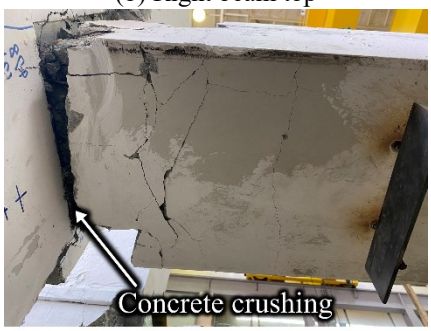

(d) Right beam bottom

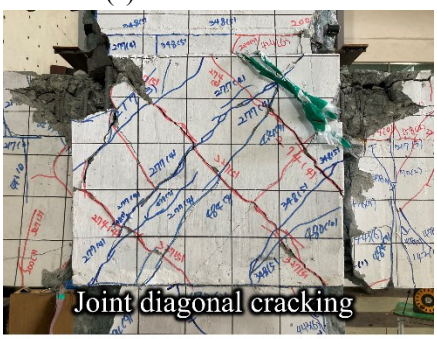

(e) Front joint

(f) Back joint

Figure 5-15 J-G1 detailed failure pictures

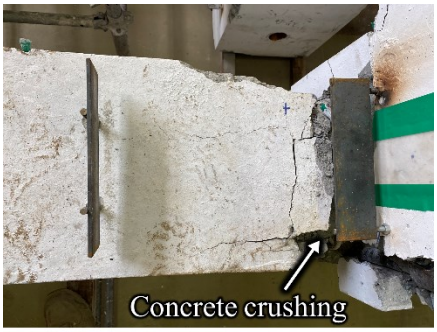

(a) Left beam top

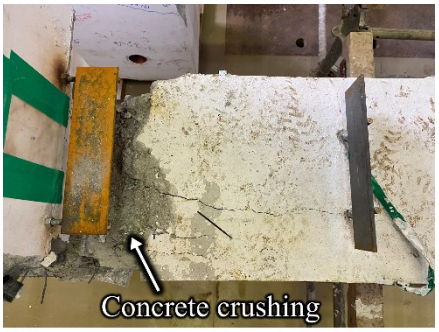

(b) Right beam top

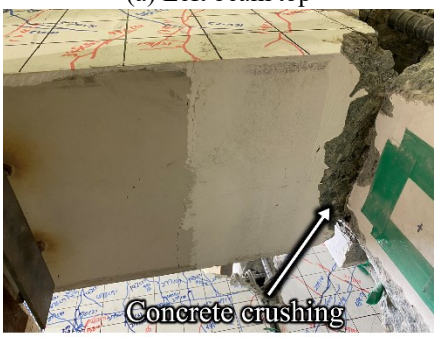

(c) Left beam bottom

(d) Right beam bottom

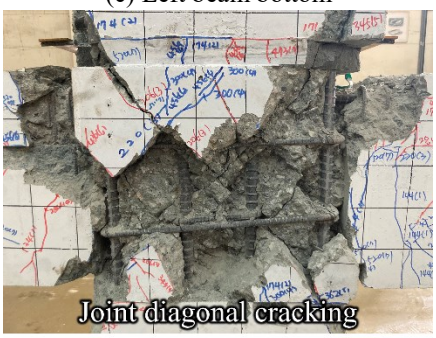

(e) Front joint (cover eliminated)

(f) Back joint

Figure 5-16 J-G2 detailed failure pictures

5.4.3 Strain of steel reinforcements

From **Figure 5-17** to **Figure 5-19** show strains of beam longitudinal reinforcements at the beam ends 30 mm away from the joint face. In every reinforcement, strains exceeded the yield strains (ε_y = 0.00336 (D25), 0.00329 (D22)). This means plastic hinges were formed in the beams as expected. In J-N1, strains of beam top longitudinal reinforcement dropped rapidly as bond damage occurred after the peak load (**Figure 5-17**). In J-G1, beam bottom longitudinal reinforcements showed more ductile behavior than the other specimens (**Figure 5-18**).

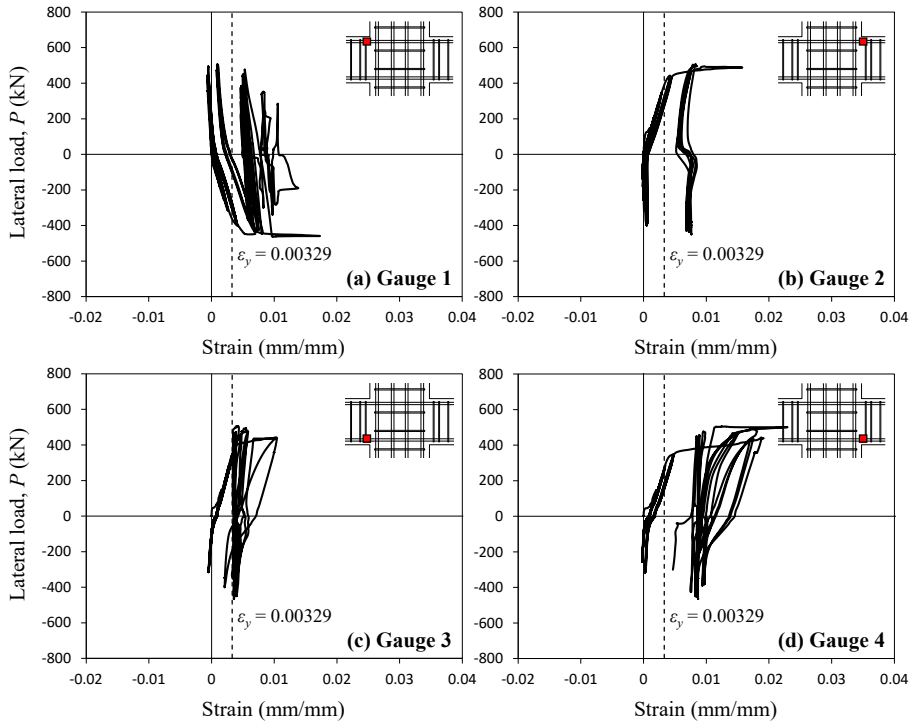

Figure 5-17 Strain of beam longitudinal reinforcement of J-N1

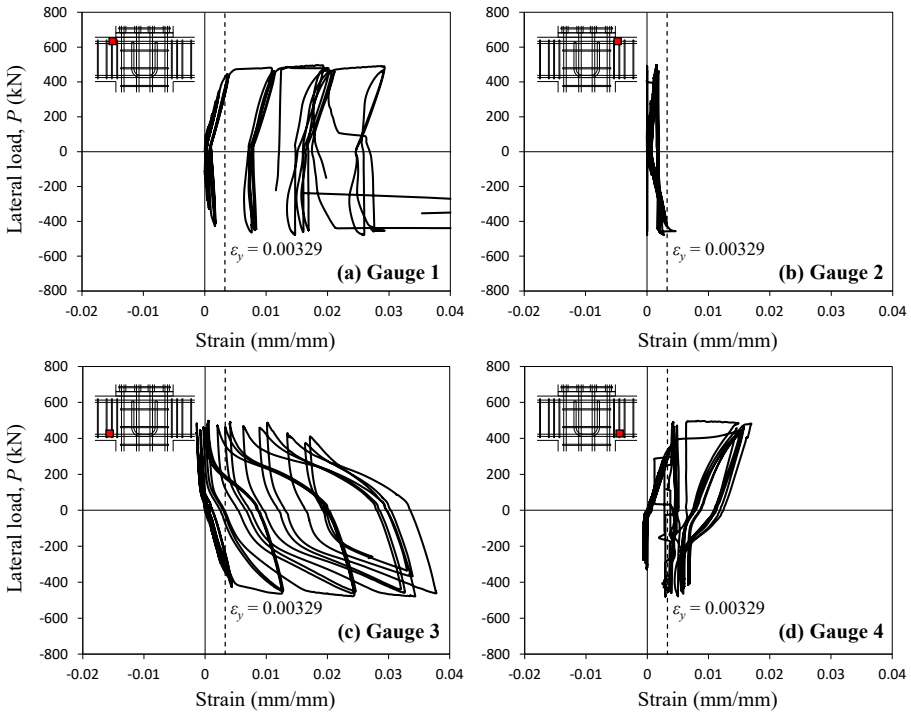

Figure 5-18 Strain of beam longitudinal reinforcement of J-G1

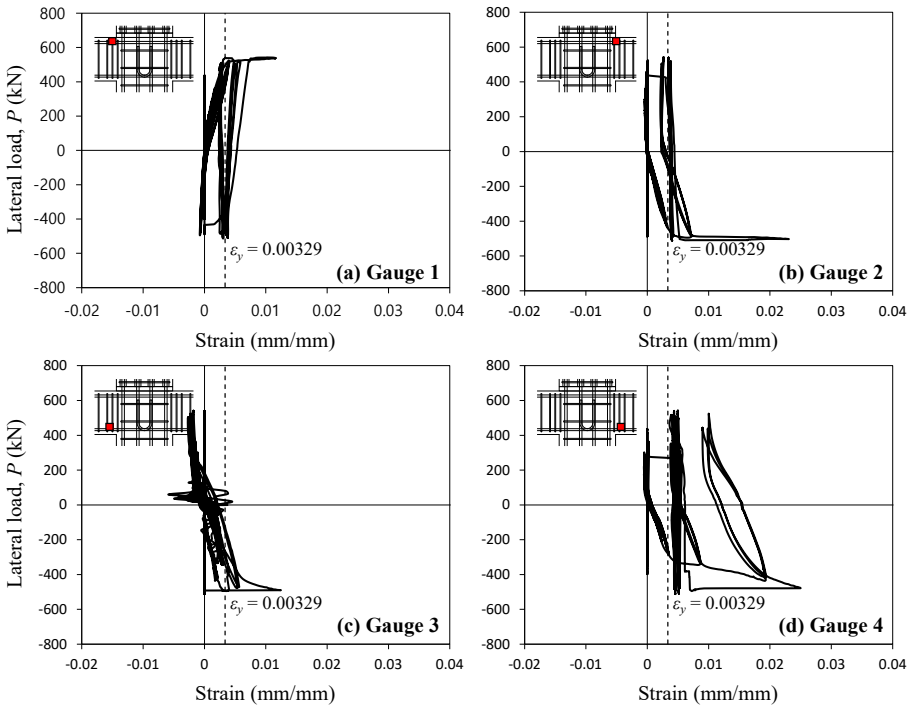

Figure 5-19 Strain of beam longitudinal reinforcement of J-G2

Figure 5-20 shows strains of joint transverse reinforcements located in the center of the joint. In J-N1 and J-G1, the strains did not exceed the yield strain. The strain of J-G2 reached the yield strain, but it was not significantly large. This means all beam-column specimens did not suffer severe steel deformation in the joint, but the steel deformation of J-G2 which used the shorter overlap length was larger than J-G1 which used the longer overlap length.

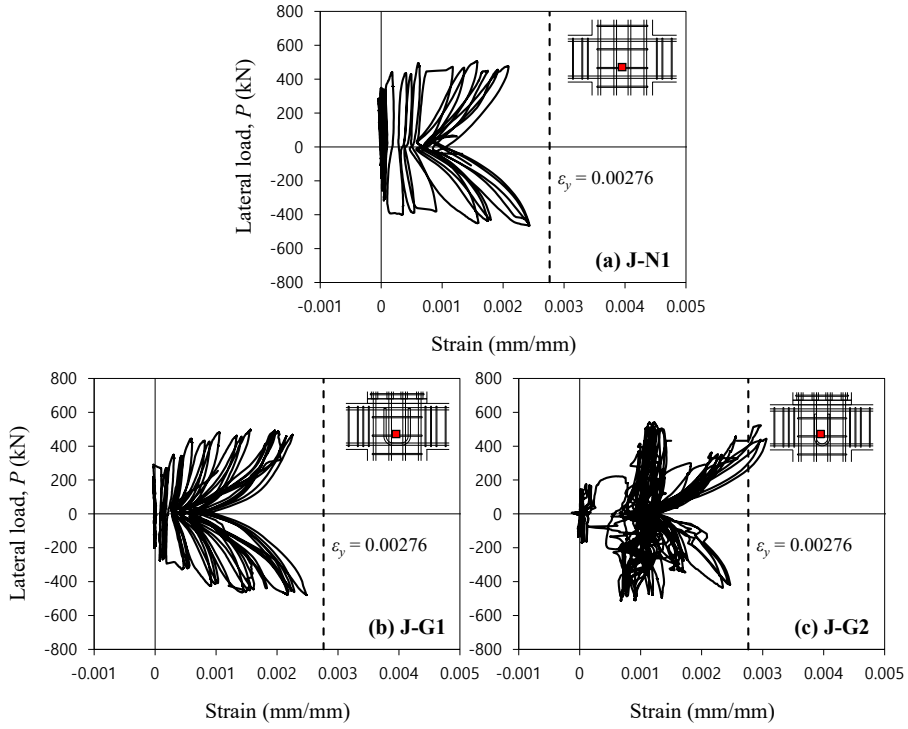

Figure 5-20 Strain of joint transverse reinforcement

5.4.4 Secant stiffness

As shown in **Figure 5-21**, secant stiffnesses of the beam-column specimens were the same. The secant stiffness was calculated from a straight line passing through the minimum and the maximum load points at the first load cycle of each drift ratio.

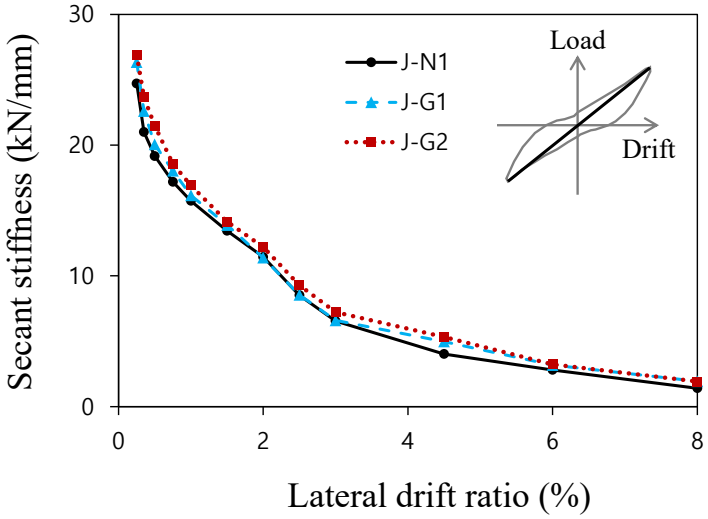

Figure 5-21 Secant stiffness of beam-column connections

5.4.5 Panel zone deformation

Lateral drift developed by panel zone deformation (Δ_{pz}) can be calculated by **Figure 5-22** and **Eq 5-9**. Here, γ_{pz} is shear distortion angle at the joint, H is the height of beam-column connection, L is the length between the beam supports, and h_c and h_b are the section depth of the column and the beam, respectively. Shear distortion angle (γ_{pz}) can be calculated by $\gamma_{pz} = (\delta_j - \delta_j')\sqrt{a^2+b^2}/2ab$ using two LVDTs (δ_j, δ_j') installed at the joint panel zone with X-shape as shown in **Figure 5-23** (Here, a and b are horizontal and vertical spacing of LVDTs).

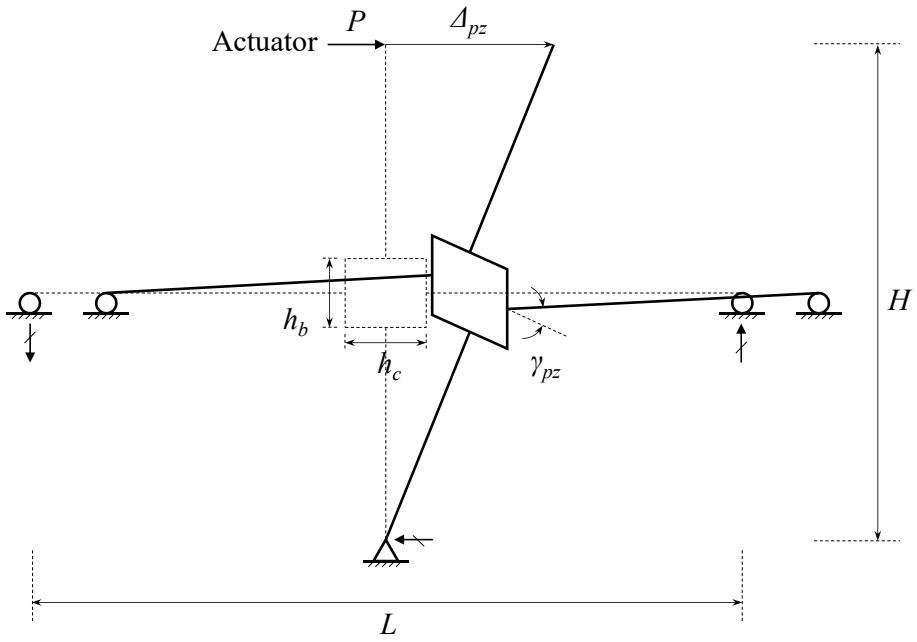

Figure 5-22 Calculation of drift developed by panel zone shear deformation

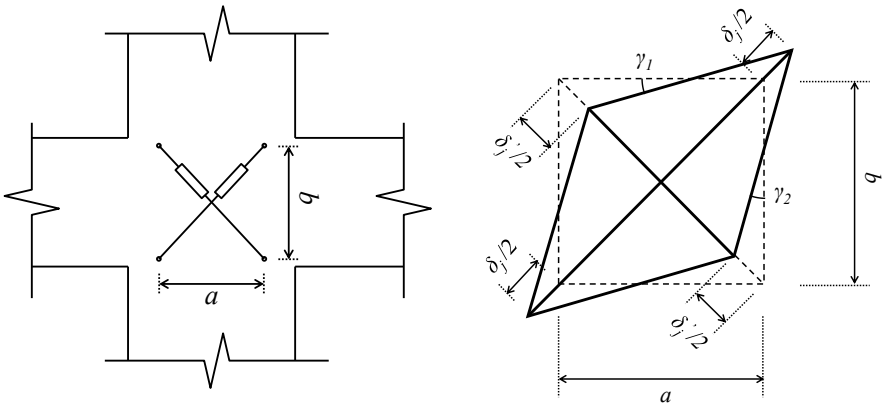

(a) LVDT at the joint (b) Panel zone shear deformation

Figure 5-23 Calculation of panel zone shear deformation

$$\Delta_{pz} = \gamma_{pz}\left(H - h_c\frac{H}{L} - h_b\right) \qquad \text{Eq 5-6}$$

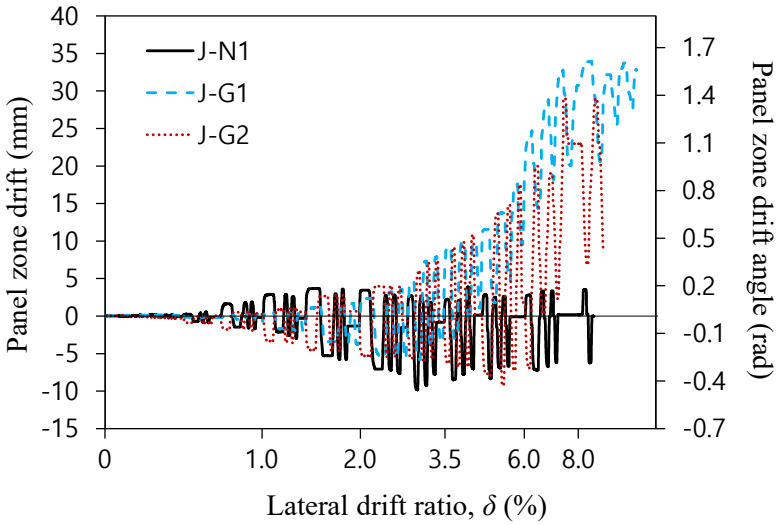

Figure 5-24 Drift developed by panel zone shear deformation

As shown in **Figure 5-24**, Panel zone shear deformation was the largest in J-G1, the next was J-G2, and J-N1 showed the smallest deformation. In case of J-N1, beam bottom longitudinal reinforcements passing through the joint suffered severe bond damage, which caused relatively small panel zone shear deformation. Both J-G1 and J-G2 met anchorage length of hooked bars specified in ACI 352R-02 (the same as KDS 14 20 52 :2022 and ACI 318-14; refer to **2.1 (k)**), but J-G1 showed greater panel zone shear deformation than J-G2.

5.4.6 Energy dissipation

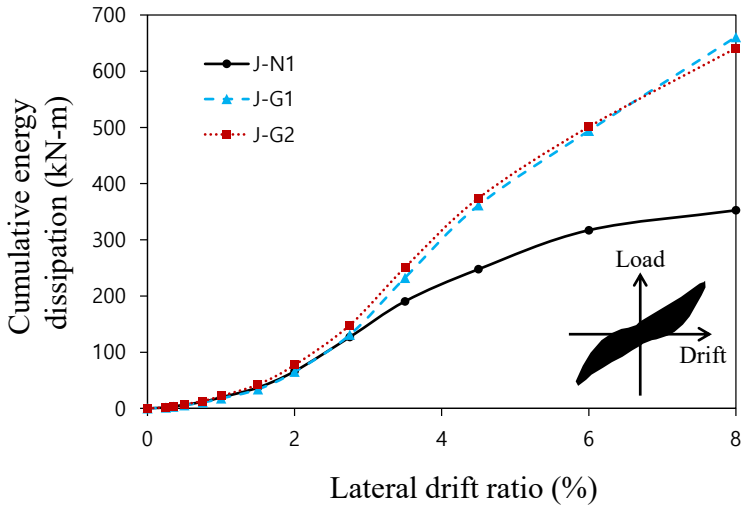

Figure 5-25 Cumulative energy dissipation of beam-column connection specimens

Figure 5-25 shows cumulative energy dissipation of the beam-column connection specimens according to lateral drift ratio. Energy dissipation is defined by an area of a closed loop in each drift ratio in a hysteresis curve. Until

2.75% drift ratio where the load reached the peak, all specimens showed similar cumulative energy dissipation. After the peak load, the difference was captured in cumulative energy dissipation in inelastic range. J-G1 and J-G2 showed similar energy dissipation, which was relatively greater than J-N1. Their cumulative energy dissipation was 232 kN-m and 251 kN-m respectively at 3.5% drift ratio, and 661 kN-m and 641 kN-m respectively at 8.0% drift ratio. On the other hand, J-N1 showed relatively small energy dissipation due to bond failure of the beam bottom longitudinal reinforcements. Its cumulative energy dissipation was 191 kN-m at 3.5% drift ratio (82% of J-G1 and 76% of J-G2), and 353 kN-m at 8.0% drift ratio (53% of J-G1 and 55% of J-G2).

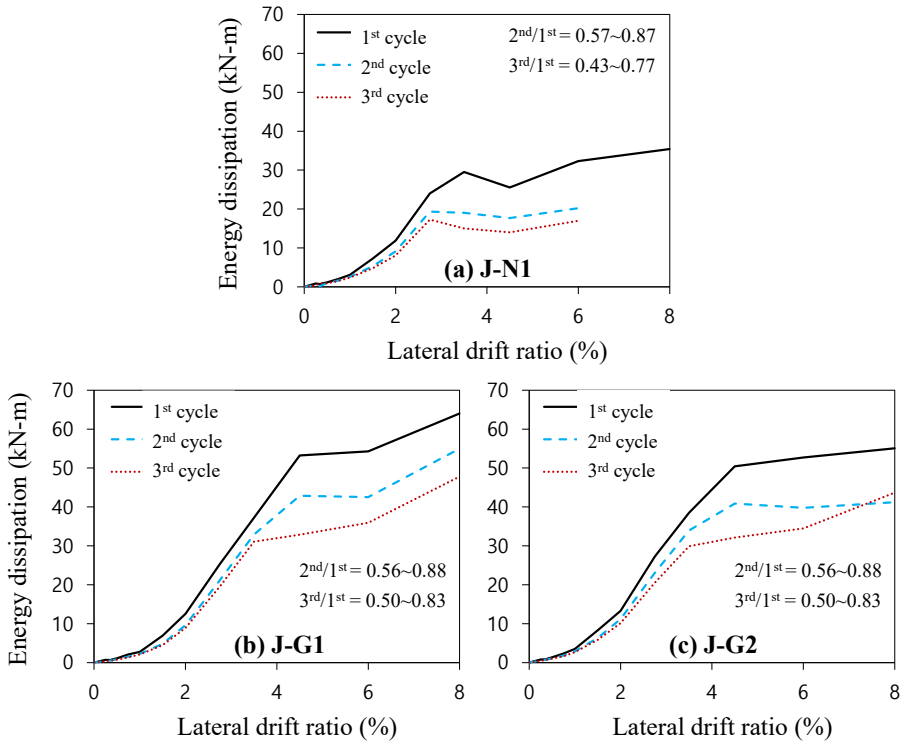

Figure 5-26 Energy dissipation per load cycle of beam-column connection specimens

Figure 5-26 shows energy dissipation per load cycle of the beam-column connection specimens according to lateral drift ratio. Energy dissipation of J-N1 whose beam top and bottom longitudinal reinforcements passed through the joint was relatively lesser than that of J-G1 and J-G2 whose beam bottom longitudinal reinforcements were anchored by 90° hooked bars inside the joint. This is because after plastic hinges were formed at the beam ends at the peak load and concrete crushing and concrete cover spalling occurred at the bottom of the beams, bond capacity of the beam bottom longitudinal reinforcements decreased and slip occurred.

No significant difference in energy dissipation was observed between J-G1 and J-G2 whose beam bottom longitudinal reinforcements were anchored by 90° hooked bars inside the joint. At 8.0% drift ratio, J-G2 showed relatively lesser energy dissipation than J-G1 because of severe joint cracking.

In all specimens, energy dissipation decreased rapidly at the second load cycle after the peak load. Energy dissipation of the second cycle was 56–88% of that of the first cycle. Energy dissipation of the third cycle decreased than that of the second cycle but showed similar pattern.

5.4.7 Deformation capacity

The envelop curve shown in **Figure 5-27 (a)** was drawn by connecting maximum load points at each drift ratio. Until the peak load, the monolithic and the PC specimens showed almost the same load-displacement relationship, reaching equivalent peak strength. However, after the peak load, the patterns of

the monolithic specimen and the PC specimens were different. While the both PC specimens gradually decreased in strength regardless of the length of the joint hook anchorage, the monolithic specimen showed a relatively steep decrease in strength compared to the PC specimens.

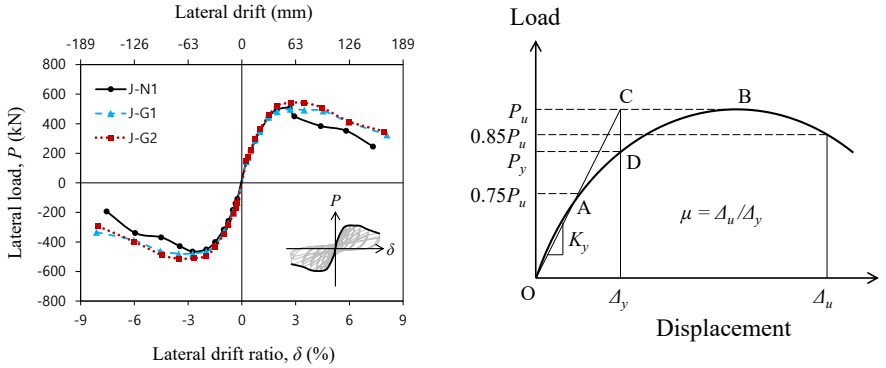

(a) Envelop curve (b) Definition of deformation capacity

Figure 5-27 Envelop curve and definition of deformation capacity of beam-column specimens

Deformation capacity was calculated using a method illustrated in **Figure 5-27 (b)** based on the envelop curve. The deformation capacity was characterized by yield strengths, yield stiffnesses, maximum strengths, yield displacements, yield drift ratios, ultimate displacements, ultimate drift ratios, and ductility. Yield displacements were defined by the drift ratio at the peak load of a straight line passing the origin and the point of 75% of the peak load. Ultimate displacements were defined by the drift ratio at the point of 85% of peak load after the peak load. Yield stiffnesses were defined by the value dividing the peak load with the yield displacement.

As shown in **Table 5-8**, the yield strengths and the maximum strengths of the test specimens were similar. The yield displacements were also similar, so were

the yield stiffnesses. However, the ultimate displacements of J-G1 and J-G2 were greater than that of J-N1 (54% and 43% higher respectively). Therefore, the ductility of J-G1 and J-G2 was greater than that of J-N1 (61% and 38% higher respectively).

Table 5-8 Deformation capacity of beam-column connection specimens

	Yield strength P_y (kN)		Yield stiffness K_y (kN/mm)		Peak strength P_u (kN)		Yield drift ratio δ_y (%)		Ultimate drift ratio δ_u (%)		Ductility μ	
Specimen	Pos.	Neg.	Pos.	Neg.	Pos.	Neg.	Pos.	Neg.	Pos.	Neg.	Pos.	Neg.
J-N1	449	-411	15.9	14.2	506	-465	1.55	-1.59	3.39	-4.05	2.18	2.54
J-G1	446	-429	16.2	16.2	498	-479	1.50	-1.54	5.72	-5.66	3.80	3.68
J-G2	476	-450	15.5	15.5	542	-513	1.65	-1.61	5.25	-5.36	3.18	3.32

5.4.8 Seismic performance evaluation by ACI 374.1-05

ACI 374-05 specifies acceptance criteria for evaluating seismic performance of reinforced concrete moment frames by experiments. If all the acceptance criteria are satisfied, the test specimen can be considered to have equivalent seismic performance to special moment frames according to ACI 318-19 (**refer to 2.1 (m)**).

As shown in **Table 5-9**, only J-G1 and J-G2, the PC specimens with the geopolymer concrete, satisfied all acceptance criteria from (b) to (e). Criterion (a) was excluded in the study because the allowable story drift in criterion (a) differs according to required ductility when structure designing. On the other hand, J-N1, the monolithic specimen with the normal concrete, dissatisfied the criteria expect criterion (b) and (d), which are criteria to check whether failure occurred at a beam according to the strong-column-weak-beam concept and to ensure adequate damping for the frame as a whole, respectively.

Criteria (c) and (e) which only J-N1 failed to satisfy are related to the third load cycle of 3.5% drift ratio. In **Figure 5-28** which shows the third load cycle of 3.5% drift ratio, the peak strengths of J-N1, the monolithic specimen, was 26% and 30% lower than those of J-G1 and J-G2, the PC specimens, in both positive and negative direction (criterion (c)). And also, J-N1 showed severe pinching behavior, which was characterized by the flat curves near the origin (criterion (e)). This is because the beam bottom longitudinal reinforcements passing through the joint suffered severe bond slip. As such, unlike J-N1 showed the same secant stiffness as those of J-G1 and J-G2, the stiffness near the origin was severely lower than those of J-G1 and J-G2.

Table 5-9 Seismic performance evaluation by ACI 374.1-05

Criterion		J-N1		J-G1		J-G2	
		Pos.	Neg.	Pos.	Neg.	Pos.	Neg.
(b) Maximum lateral load (kN)	E_{max}	506	-465	498	-479	542	-513
	λE_n	1034	-1034	1032	-1032	1035	-1035
	Judgement	OK	OK	OK	OK	OK	OK
(c) Lateral force at 3.5% (kN)	$0.75E_{max}$	379	-349	374	-359	406	-385
	E at 3.5%	339	-324	459	-440	487	-463
	Judgement	NG	NG	OK	OK	OK	OK
	/(J-N1)	-	-	1.37	1.32	1.34	1.29
(d) Energy dissipation (kN-m)	Elastic plastic	79.4		102		106	
	Actual	15.0		31.1		29.9	
	Ratio	0.189		0.306		0.282	
	Judgement	OK		OK		OK	
	/(J-N1)	-		1.62		1.49	
(e) Stiffness (kN/mm)	5% of initial K	1.44	1.04	1.37	1.26	1.39	1.30
	K at 3.5%	0.82	0.44	4.78	4.23	4.28	3.38
	Judgement	NG	NG	OK	OK	OK	OK
	/(J-N1)	-	-	6.08	7.90	5.37	6.14

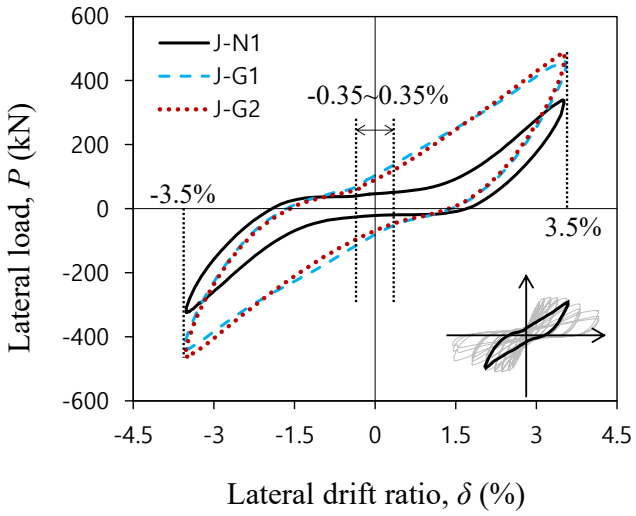

Figure 5-28 The 3rd load cycle of 3.5% drift ratio

5.4.9 Seismic performance evaluation by AIJ 2002 Guidelines

AIJ 2002 Guidelines specifies structural performance goals so that PC structure can ensure the performance of RC structure. If PC members on ultimate limit state under earthquake load satisfy all the acceptance criteria, PC members can ensure the equivalent performance to RC members (**refer to 2.1 (n)**). The result is summarized in **Table 5-10**,

The PC geopolymer concrete beam-column connection specimens (J-G1, J-G2) satisfied the acceptance criteria compared with the monolithic normal concrete specimen (J-N1) in overall. The yield strengths and the peak strengths of the PC geopolymer concrete specimens were 99-110% and 111-125% of the monolithic normal concrete specimen, respectively. The strengths at 2% drift ratio of the PC geopolymer concrete specimens were 97% of the peak strengths,

which were higher than 80% as the guideline suggests. The yield drift ratios of the PC geopolymer concrete specimens were 96-106% of the monolithic normal concrete specimen, where the difference between the specimens were not more than 20% as the guideline suggests. The energy dissipation at the 2nd cycle of 2% drift ratio of the PC geopolymer concrete specimens was 106-123% of the monolithic normal concrete specimen, which were higher than 80% as the guideline suggests.

Table 5-10 Seismic performance evaluation by AIJ 2002 Guidelines

Criterion		J-N1		J-G1		J-G2	
		Pos.	Neg.	Pos.	Neg.	Pos.	Neg.
(a) Yield strength	P_y (kN)	449	-411	446	-429	476	-450
	/J-N1	-	-	0.99	1.04	1.06	1.10
(b) Peak strength	P_u (kN)	506	-465	498	-479	542	-513
	/J-N1	-	-	1.11	1.17	1.21	1.25
(c) Strength at 2% drift ratio	P_u at 2% (kN)	495		482		524	
	(P_u at 2%)/P_u	0.978		0.968		0.966	
(d) Yield drift ratio	δ_u (%)	1.55	-1.59	1.50	-1.54	1.65	-1.61
	/J-N1	-	-	0.97	0.96	1.06	1.01
(e) Energy dissipation	E at 2% (kN-m)	9.10		9.60		11.2	
	/J-N1	-		1.06		1.23	

5.5 Summary

In this chapter, the cyclic loading tests were conducted to investigate seismic performance of the PC beam-column connections using the geopolymer concrete. Total 3 beam-column connection specimens (1 normal concrete and 2 geopolymer concrete) were tested for the cyclic loading tests. The test parameters included concrete types (normal or geopolymer), construction methods (monolithic or PC), and overlap lengths of hooked bars anchored inside the joint (290 mm or 170 mm). For the PC beam-column connections, the beams and the columns used the geopolymer concrete while topping and joint used the normal concrete. The same details of reinforcements used in PC construction were adopted such as 90° hook anchorage of the beam bottom longitudinal bars, while the monolithic beam-column connection used straight beam bottom longitudinal bars passing through the joint panel. The seismic performance of the beam-column connections was investigated in terms of strength, load-displacement relationship, failure mode, secant stiffness, energy dissipation, and ductility. The seismic performance of each specimen was evaluated by ACI 374.1-05 and AIJ 2002 Guidelines.

For the seismic performance of the PC beam-column connections using the geopolymer concrete, the major findings are summarized as follows:

1) The PC geopolymer concrete beam-column connections (J-G1, J-G2) developed the predicted strengths calculated by the design codes (P_u/P_n = 1.01-1.11)

2) The PC geopolymer concrete beam-column connections (J-G1, J-G2)

showed superior seismic performance to the monolithic normal concrete beam-column connection (J-N1). The PC geopolymer concrete beam-column connections showed 82-87% higher energy dissipation and 38-61% higher ductility than the monolithic normal concrete beam-column connection.

3) The PC geopolymer concrete beam-column connections (J-G1, J-G2) showed equivalent seismic performance to special moment frames by satisfying all the criteria of ACI 374.1-05.

4) The failure modes after beam flexural yielding varied depending on the construction methods (monolithic or PC). The monolithic beam-column connection (J-N1) suffered bond damage of beam bottom longitudinal bars rather than joint damage. On the other hand, the PC beam-column connections (J-G1, J-G2) suffered cracking damage on the joint and concrete crushing on beam top region at the joint face.

5) The monolithic beam-column connection with beam bottom bars passing through the joint (J-N1) suffered severe bond slip damage, which degraded energy dissipation, ductility, and load-carrying capacity after the peak strengths compared to the PC beam-column connections with joint hook anchorage. The severe pinching effect was detected in the load-displacement relationship of the monolithic beam-column connection.

6) The beam-column connections with different overlap lengths of hooked bars (J-G1, J-G2) showed no significant difference in seismic performance. This may be because beam flexural failure dominated rather than joint shear failure, the difference of overlap length was not significant, and the

reinforcement ratio of beam bottom longitudinal reinforcement was low. Further studies are needed to evaluate the effect of different overlap lengths of joint hook anchorage.

7) Nevertheless, slight disadvantages were discovered on using shorter overlap length of joint hook anchorage. The beam-column connection with shorter overlap length (J-G2) suffered slightly more cracking damage on the joint, slightly greater steel deformation on the transverse reinforcement in the joint, while experiencing slightly less panel zone shear deformation. The ductility of the beam-column connection with shorter overlap length was 15% less than that of the specimen with longer overlap length (J-G1)

Chapter 6. Conclusion

Cyclic loading tests were conducted to evaluate the seismic performance of PC columns and beam-column connections using the geopolymer concrete. The geopolymer concrete in the study had the specific mix proportion with the binder composed of 100% GGBS and alkaline activator (Ca-type composites). The geopolymer concrete specimens were compared with the normal concrete specimens with the binder composed of 70% cement and 30% GGBS. The geopolymer concrete specimens with different design parameters were also compared one another. The study also covered the effects of the connection details of PC (splice sleeve connections, joint hook anchorage). The performance was mainly compared in terms of strength, load-displacement relationship, failure mode, secant stiffness, energy dissipation, and deformation capacity.

The general conclusion of the study is presented as follows:

The geopolymer concrete had equivalent material performance to the normal concrete or exceeded the equations of the design codes in overall. The PC columns and beam-column connections using the geopolymer concrete developed the predicted strengths calculated by the design codes. The PC columns and beam-column connections using the geopolymer concrete showed superior seismic performance to the monolithic normal concrete specimens. The load-displacement relationship and energy dissipation of the PC columns using the geopolymer concrete were equivalent to those of the PC columns using the normal concrete. However, the ductility of the PC columns using the

geopolymer concrete was 35% lower than that of the PC column using the normal concrete. The different performance between PC geopolymer concrete specimens and monolithic normal concrete specimens does not assure material superiority of the geopolymer concrete, which seems to be mainly caused by PC details. Thus, a further study is needed for seismic performance of monolithic columns and beam-column connections using geopolymer concrete.

Specifically, for the material performance of the geopolymer concrete, the major findings are summarized as follows:

1) The compressive strengths of the standard-cured geopolymer concrete on day 7, 14, and 28 were 50.5, 58.0, and 64.2 MPa, respectively (Ø100×200 mm) and 52.4, 59.2, and 65.4 MPa, respectively (Ø150×300 mm). In the ambient-cured group, the compressive strength of the geopolymer and the normal concrete was only 5% different.

2) The stress-strain curves of standard-cured geopolymer concrete were similar in different size of cylinders. The stress-strain curves of the ambient-cured geopolymer concrete cylinders showed little difference from the stress-strain curves of the normal concrete cylinders.

3) The ratio of tested modulus of elasticity of the standard-cured geopolymer concrete to KDS ($E_{c,test}/E_{c,KDS}$) was 81% (Ø100×200 mm) and 88% (Ø 150×300 mm) in average. As to ACI 318, the ratio ($E_{c,test}/E_{c,ACI}$) was 74% (Ø100×200 mm) and 81% (Ø150×300 mm) in average. In the ambient-cured group, regardless of the concrete type, the tested modulus of elasticity was 9-15% (geopolymer) and 5-12% (normal) lower than the equations of the design codes.

4) The average strains at peak stress of the standard-cured geopolymer concrete ranged from 0.00279 to 0.00340. In the ambient cured group, the average strains at peak stress of the geopolymer concrete was 1-9% different from that of the normal concrete.

5) The modulus of rupture (i.e. flexural strength) of the standard-cured geopolymer concrete on day 7, 14, and 28 was 5.82, 5.96, and 6.06 MPa, where the ratio of tested modulus of rupture to KDS ($f_{r,test}/f_{r,KDS}$) was 125%, and the ratio to ACI 318 ($f_{r,test}/f_{r,ACI}$) was 127% in average. In ambient-cured group, regardless of the concrete type, the tested modulus of rupture was higher than the equations of the design codes.

6) The splitting tensile strengths of the standard-cured geopolymer concrete on day 7, 14, and 28 were 4.88, 5.40, and 5.44 MPa, respectively (Ø100×200 mm) and 4.66, 5.10, and 5.5 MPa, respectively (Ø150×200). Regardless of the size of the cylinder, the tested splitting tensile strengths were 14-24% higher than the equations of ACI 314 and ACI 363. Regardless of concrete type and cylinder size, the tested splitting tensile strengths were higher than the equations of the design codes.

For the seismic performance of the PC columns using the geopolymer concrete, the major findings are summarized as follows:

1) The geopolymer concrete columns (C-G1, C-G2, C-G3, C-G1-IMP, and C-G4-IMP) developed the predicted strengths calculated by the design codes (P_u/P_n = 1.03-1.15, except negative loading of C-G1 which had grouting defects).

2) The PC geopolymer concrete columns (C-G1 (positive loading) and C-G3) showed similar or superior seismic performance to the monolithic normal concrete column (C-N1). The PC geopolymer concrete columns resisted until 8.0% drift ratio, whereas the monolithic normal concrete column failed at 3.5% drift ratio.

3) The PC geopolymer concrete columns (C-G1 (positive loading) and C-G3) showed equivalent seismic performance to the PC normal concrete column (C-N2). The strength, load-displacement relationship, failure mode, and energy dissipation of the PC geopolymer concrete columns were similar to those of the PC normal concrete column. the PC geopolymer concrete columns (C-G1 (positive loading), C-G3) satisfied AIJ 2002 Guidelines for ensuring equivalent performance to the PC normal concrete columns (C-N2).

4) However, ductility of the PC geopolymer concrete columns (C-G1) was 35% lower than that of the PC normal concrete column (C-N2) due to the effect of grouting quality. The cracking patterns and the stress-strain curves were almost the same.

5) The PC columns with grouting defects (C-G1 (negative loading), C-G1-IMP, C-G4-IMP) showed inferior performance to the PC column without grouting defects (C-N2). The test strength was 9% lower than the predicted strength calculated by the design codes. The PC columns with grouting defects showed 10-35% lower energy dissipation and 26-48% lower ductility than the PC column without grouting defects.

6) The PC column with larger-size sleeves (C-G3) prevented grouting defects

caused by poor injecting quality of grouting. However, using larger-size sleeves does not mean better seismic performance.

7) The PC column with higher reinforcement ratio (C-G2) showed better performance. It could prevent bond failure of the longitudinal reinforcements inside the splice sleeves because of the low steel strains, so that could maintain the strength after the peak load.

For the seismic performance of the PC beam-column connections using the geopolymer concrete, the major findings are summarized as follows:

1) The PC geopolymer concrete beam-column connections (J-G1, J-G2) developed the predicted strengths calculated by the design codes (P_u/P_n = 1.01-1.11)

2) The PC geopolymer concrete beam-column connections (J-G1, J-G2) showed superior seismic performance to the monolithic normal concrete beam-column connection (J-N1). The PC geopolymer concrete beam-column connections showed 82-87% higher energy dissipation and 38-61% higher ductility than the monolithic normal concrete beam-column connection.

3) The PC geopolymer concrete beam-column connections (J-G1, J-G2) showed equivalent seismic performance to special moment frames by satisfying all the criteria of ACI 374.1-05.

4) The failure modes after beam flexural yielding varied depending on the construction methods (monolithic or PC). The monolithic beam-column connection (J-N1) suffered bond damage of beam bottom longitudinal bars

rather than joint damage. On the other hand, the PC beam-column connections (J-G1, J-G2) suffered cracking damage on the joint and concrete crushing on beam top region at the joint face.

5) The monolithic beam-column connection with beam bottom bars passing through the joint (J-N1) suffered severe bond slip damage, which degraded energy dissipation, ductility, and load-carrying capacity after the peak strengths compared to the PC beam-column connections with joint hook anchorage. The severe pinching effect was detected in the load-displacement relationship of the monolithic beam-column connection.

6) The beam-column connections with different overlap lengths of hooked bars (J-G1, J-G2) showed no significant difference in seismic performance. This may be because beam flexural failure dominated rather than joint shear failure, the difference of overlap length was not significant, and the reinforcement ratio of beam bottom longitudinal reinforcement was low. Further studies are needed to evaluate the effect of different overlap lengths of joint hook anchorage.

7) Nevertheless, slight disadvantages were discovered on using shorter overlap length of joint hook anchorage. The beam-column connection with shorter overlap length (J-G2) suffered slightly more cracking damage on the joint, slightly greater steel deformation on the transverse reinforcement in the joint, while experiencing slightly less panel zone shear deformation. The ductility of the beam-column connection with shorter overlap length was 15% less than that of the specimen with longer overlap length (J-G1)

References

[1] ACI Committee 209, "Prediction of Cree, Shrinkage, and Temperature Effects in Concrete Structures (ACI 209R-92) (Reapproved 2008)." Farmington Hills, MI: American Concrete Institute, 1992.

[2] ACI Committee 318, "Building Code Requirements for Structural Concrete (ACI 318-14) and Commentary." Farmington Hills, MI: American Concrete Institute, 2014.

[3] ACI Committee 318, "Building Code Requirements for Structural Concrete (ACI 318-19) and Commentary." Farmington Hills, MI: American Concrete Institute, 2019.

[4] ACI Committee 363, "State-of-the-Art Report on High-Strength Concrete (ACI 363R-92) (Reapproved 1997)." Farmington Hills, MI: American Concrete Institute, 1992.

[5] ACI Committee 374, "Acceptance Criteria for Moment Frames Based on Structural Testing and Commentary (ACI 374.1-05) (Reapproved 2014)." Farmington Hills, MI: American Concrete Institute, 2005.

[6] AIJ, "Guidelines for Structural Design of Precast Concrete Connection Emulating Cast-in-place Reinforced Concrete." Tokyo, Japan: Architecture Institute of Japan, 2002.

[7] J. Aldred and J. Day, "Is geopolymer concrete a suitable alternative to traditional concrete," in *Proceedings of the 37th Conference on Our World in Concrete & Structures, Singapore*, 2012, pp. 29-31.

[8] M. Ameli, J. E. Parks, D. N. Brown, and C. P. Pantelides, "Seismic evaluation of grouted splice sleeve connections for reinforced precast concrete column-to-cap beam joints in accelerated bridge construction," *PCI journal,* vol. 60, no. 2, pp. 80-103, 2015.

[9] Y. M. Amran, R. Alyousef, H. Alabduljabbar, and M. El-Zeadani, "Clean

production and properties of geopolymer concrete; A review," *Journal of Cleaner Production,* vol. 251, p. 119679, 2020.

[10] ASTM C469, "Standard Test Method for Static Modulus of Elasticity and Poisson's Ratio of Concrete in Compression." West Conshohocken, PA: ASTM International, 2002.

[11] Concrete Products, "Alternative Materials to the Rescue!" https://concreteproducts.com/index.php/2022/11/12/alternative-materials-to-the-rescue/ (accessed Jan. 26, 2023).

[12] B. De Nicolo, L. Pani, and E. Pozzo, "Strain of concrete at peak compressive stress for a wide range of compressive strengths," *Materials and Structures,* vol. 27, no. 4, pp. 206-210, 1994.

[13] E. I. Diaz-Loya, E. N. Allouche, and S. Vaidya, "Mechanical properties of fly-ash-based geopolymer concrete," *ACI materials journal,* vol. 108, no. 3, p. 300, 2011.

[14] Fédération Internationale du Béton (fib), "fib Model Code for Concrete Structures 2010." Lausanne, Switzerland, 2012.

[15] A. Hutagi, R. Khadiranaikar, and A. A. Zende, "Behavior of geopolymer concrete under cyclic loading," *Construction and Building Materials,* vol. 246, p. 118430, 2020.

[16] S.-J. Hwang and H.-J. Lee, "Analytical model for predicting shear strengths of exterior reinforced concrete beam-column joints for sesimic resistance," *ACI Structural Journal,* vol. 96, pp. 846-857, 1999.

[17] IEA. "Cement." IEA. https://www.iea.org/reports/cement (accessed Nov. 14, 2022).

[18] Joint ACI-ASCE Committee 352, "Recommendations for Design of Beam-Column Connections in Monolithic Reinforced Concrete Structures (ACI 352R-02)." Farmington Hills, MI: American Concrete Institute, 2002.

[19] KCS 14 20 10, "Ordinary Concrete." Gyonggi-Do, Republic of Korea:

Korea Construction Standards Center, 2022.

[20] KDS 14 20 01, " Structural Concrete Design Code(Strength Design Method): General." Gyonggi-Do, Republic of Korea: Korea Construction Standards Center, 2022.

[21] KDS 14 20 22, "Structural Concrete Design Code: Shear and Torsion." Gyonggi-Do, Republic of Korea: Korea Construction Standards Center, 2022.

[22] KDS 14 20 30, " Structural Concrete Design Code: Serviceability." Gyonggi-Do, Republic of Korea: Korea Construction Standards Center, 2022.

[23] KDS 14 20 52, " Structural Concrete Design Code: Development and Splice." Gyonggi-Do, Republic of Korea: Korea Construction Standards Center, 2022.

[24] KDS 14 20 80, "Structural Concrete Design Code: Seismic Design." Gyonggi-Do, Republic of Korea: Korea Construction Standards Center, 2022.

[25] KEITI. LCI DB (2021.08.02) [Online] Available: https://www.greenproduct.go.kr/epd/lci/evlCffcnt.do

[26] KS B 0801, "Test Pieces For Tensile Test For Metallic Materials." Chungcheongbuk-do, Repulic of Korea: Korean Agency for Technology and Standards, 2022.

[27] KS B 0802, "Method of Tensile Test For Metallic Materials." Chungcheongbuk-do, Repulic of Korea: Korean Agency for Technology and Standards, 2018.

[28] KS F 2403, "Standard Test Method For Making And Curing Concrete Specimens." Chungcheongbuk-do, Repulic of Korea: Korean Agency for Technology and Standards, 2019.

[29] KS F 2405, "Standard Test Method For Compressive Strength Of

Concrete." Chungcheongbuk-do, Repulic of Korea: Korean Agency for Technology and Standards, 2017.

[30] KS F 2408, "Standard test method for flexural strength of concrete." Chungcheongbuk-do, Repulic of Korea: Korean Agency for Technology and Standards, 2021.

[31] KS F 2423, "Standard test method for tensile splitting strength of concrete." Chungcheongbuk-do, Repulic of Korea: Korean Agency for Technology and Standards, 2021.

[32] KS F 2438, " Standard test method for static modulus of elasticity and Poisson's ratio in compression of cylindrical concrete specimens." Chungcheongbuk-do, Repulic of Korea: Korean Agency for Technology and Standards, 2022.

[33] KS F 4044, "Hydraulic-cement grout(nonshrink)." Chungcheongbuk-do, Repulic of Korea: Korean Agency for Technology and Standards, 2019.

[34] F. Legeron and P. Paultre, "Prediction of modulus of rupture of concrete," *Materials Journal,* vol. 97, no. 2, pp. 193-200, 2000.

[35] F. Lin and X. Wu, "Mechanical performance and stress–strain relationships for grouted splices under tensile and cyclic loadings," *International Journal of Concrete Structures and Materials,* vol. 10, no. 4, pp. 435-450, 2016.

[36] H. Liu, Q. Yan, and X. Du, "Seismic performance comparison between precast beam joints and cast-in-place beam joints," *Advances in Structural Engineering,* vol. 20, no. 9, pp. 1299-1314, 2017.

[37] N. Lloyd and V. Rangan, "Geopolymer concrete with fly ash," in *Proceedings of the Second International Conference on sustainable construction Materials and Technologies*, 2010: UWM Center for By-Products Utilization, pp. 1493-1504.

[38] Z. Lu, Z. Wang, J. Li, and B. Huang, "Studies on seismic performance of precast concrete columns with grouted splice sleeve," *Applied sciences,* vol. 7, no. 6, p. 571, 2017.

[39] C.-K. Ma, A. Z. Awang, and W. Omar, "Structural and material performance of geopolymer concrete: A review," *Construction and Building Materials,* vol. 186, pp. 90-102, 2018, doi: 10.1016/j.conbuildmat.2018.07.111.

[40] Y. Mao et al., "Seismic performance of interior beam-column joints using reinforced slag-based geopolymer concrete," *Earthquake Engineering & Structural Dynamics*, 2022.

[41] McKinsey, "The net-zero transition: What it would cost, what it could bring," McKinsey & Company, 2022.

[42] K. H. Mo, U. J. Alengaram, and M. Z. Jumaat, "Structural performance of reinforced geopolymer concrete members: A review," *Construction and Building Materials,* vol. 120, pp. 251-264, 2016.

[43] T. T. Ngo, T. T. Tran, T. M. Pham, and H. Hao, "Performance of geopolymer concrete in monolithic and non-corrosive dry joints using CFRP bolts under cyclic loading," *Composite Structures,* vol. 258, p. 113394, 2021.

[44] S. Park and K. M. Mosalam, "Analytical Model for Predicting Shear Strength of Unreinforced Exterior Beam-Column Joints," *ACI Structural Journal,* vol. 109, no. 2, 2012.

[45] M. Pauletta, D. Di Luca, and G. Russo, "Exterior beam column joints–Shear strength model and design formula," *Engineering Structures,* vol. 94, pp. 70-81, 2015.

[46] S. D. Raj, N. Ganesan, R. Abraham, and A. Raju, "Behavior of geopolymer and conventional concrete beam column joints under reverse cyclic loading," *Advances in concrete construction,* vol. 4, no. 3, p. 161, 2016.

[47] P. Saranya, P. Nagarajan, and A. Shashikala, "Seismic performance of geopolymer concrete beam-column joints under reverse cyclic loading," *Innovative Infrastructure Solutions,* vol. 6, no. 2, pp. 1-10, 2021.

[48] T. Srividya, K. R. PR, M. Sivasakthi, A. Sujitha, and R. Jeyalakshmi, "A state-of-the-art on development of geopolymer concrete and its field applications," *Case Studies in Construction Materials,* vol. 16, p. e00812, 2022.

[49] M. Tasdemir, C. Tasdemir, S. Akyüz, A. Jefferson, F. Lydon, and B. Barr, "Evaluation of strains at peak stresses in concrete: A three-phase composite model approach," *Cement and concrete composites,* vol. 20, no. 4, pp. 301-318, 1998.

[50] UN Environment Programme, "2021 Global Status Report for Buildings and Construction: Towards a Zero-emission," Efficient and Resilient Buildings and Construction Sector, Nairobi, 2021.

[51] L. Xie *et al.*, "Full-scale experimental investigation on the seismic performance of PC columns before and after repair of grouting defects," *Journal of Building Engineering,* vol. 58, p. 104996, 2022.

초 록

지오폴리머 콘크리트를 사용한 프리캐스트 기둥 및 보-기둥 접합부의 내진성능

문 한 세

서울대학교 건축학과 대학원

오늘날 심각해지는 환경문제를 해결하기 위해 건설 산업은 전 세계 이산화탄소 배출량의 큰 비중을 차지하는 시멘트를 조절함으로써 이산화탄소 배출량을 감소시킬 수 있다. 지오폴리머 콘크리트는 포틀랜드 시멘트를 사용하지 않는 대체 콘크리트로서 알칼리성 자극제와 플라이애쉬, 고로슬래그 미분말과 같은 산업부산물을 사용하여 만들어진다. 그러나 광범위한 구성 재료와 배합비로 인해 지오폴리머 콘크리트의 일반적인 성능을 정량화하기가 어려운 실정이다. 이에 더해 지오폴리머 콘크리트에 관한 대부분의 기존 연구는 재료 수준에서 수행되어 왔으며, 부재 혹은 구조 수준에서의 연구는 미비하다. 이마저도 단조가력 실험에 의한 연구이며 지오폴리머 콘크리트 부재에 관해 보고된 반복가력 실험은 희박하다. 설계기준에 따르면 성능 시험을 통한 조사와 입증 없이는 산업 표준에 명시되어 있지 않은 대체 시멘트를 사용할 수 없게 되어 있다.

이번 연구에서 지오폴리머 콘크리트는 고로슬래그 미분말 100%로 구성된 결합재와 알칼리성 자극제 (칼슘계 복합재료)로 구성된 특정한 배합비로 만들어졌다. 비교 대상인 일반 콘크리트는 시멘트 70%와 고로슬래그 미분말 30%를 혼합한 결합재로 이루어졌다. 지오폴리머 콘크리트의 재료 성능을 조사하기 위해 압축강도, 응력-변형률 곡선, 탄성계수, 최대강도에서의 변형률, 파괴계수 (즉 휨강도), 그리고 쪼갬인장강도에 관한 재료실험을 수행하였다.

지오폴리머 콘크리트를 사용한 프리캐스트 (이하 PC) 기둥과 보-기둥 접합부의 내진 성능을 평가하기 위하여 반복가력실험을 수행하였다. 기둥 실험의 경우, 총 7개 실험체 (일반 콘크리트 2개, 지오폴리머 콘크리트 5개)에 대해 13% 축력비로 실험하였다. 실험 변수는 콘크리트 종류 (일반 콘크리트, 지오폴리머 콘크리트), 제작 방식 (일체타설, PC), 스플라이스 슬리브 사이즈 (D25, D29), 주철근비 (0.0162, 0.0254)로 설정하였다. 보-기둥 접합부 실험의 경우, 총 3개 실험체 (일반 콘크리트 1개, 지오폴리머 콘크리트 2개)에 대해 실험하였다. 실험 변수는 콘크리트 종류 (일반 콘크리트, 지오폴리머 콘크리트), 제작 방식 (일체타설, PC), 접합부 정착 갈고리 간 겹침길이 (290 mm, 210 mm)로 설정하였다. 주된 성능 비교는 강도, 하중-변위 관계, 할선 강성, 에너지 소산, 그리고 변형능력 관점에서 비교하였다. 추가로, ACI 374.1-05와 AIJ 2002 Guidelines에 따라 각 실험체의 내진 성능을 평가하였다.

지오폴리머 콘크리트의 전체적인 재료성능은 일반 콘크리트와

동등하거나 설계기준식을 능가하였다. 지오폴리머 콘크리트를 사용한 PC 기둥과 보-기둥 접합부는 설계기준에 따라 계산된 예상 강도를 발현하였다. PC 지오폴리머 콘크리트 실험체는 일체타설 일반 콘크리트 실험체보다 우수한 내진 성능을 보였다. PC 지오폴리머 콘크리트 실험체는 PC 일반 콘크리트 실험체와 동등한 하중-변위 관계, 에너지 소산을 보였다. 그러나 PC 지오폴리머 콘크리트 기둥은 그라우팅 상태에 따른 영향으로 인해 PC 일반 콘크리트 기둥보다 35% 낮은 연성도를 보였다.

PC 지오폴리머 콘크리트 실험체와 일체타설 일반 콘크리트 실험체 간의 성능 차이로부터 지오폴리머 콘크리트의 재료적 우수성을 단정 지을 순 없으며, 이러한 성능 차이는 주로 PC 상세에 의한 것으로 보인다. 그러므로 일체타설로 제작한 지오폴리머 콘크리트 기둥 및 보-기둥 접합부의 내진성능에 관한 추가 연구가 필요하다.

주요어: 반복가력실험, 지오폴리머 콘크리트, 기둥, 보-기둥 접합부, 프리캐스트 콘크리트, 스플라이스 슬리브, 접합부 갈고리 정착

학 번: 2021-24712